NANOSTRUCTURED POLYMER FILMS FOR ELECTRONICS

A Dissertation

Presented to

the Faculty of the Department of Chemical and Biomolecular Engineering

University of Houston

In Partial Fulfillment

of the Requirements for the Degree

Doctor of Philosophy

in Chemical Engineering

May 2014

by

Nikhila Mahadevapuram

NANOSTRUCTURED POLYMER FILMS FOR ELECTRONICS

Nikhila Mahadevapuram

Approved:

Chair of the Committee
Gila E. Stein, Assistant Professor,
Chemical and Biomolecular Engineering

Committee Members:

Michael P. Harold, Professor and Chair,
Chemical and Biomolecular Engineering

Demetre J. Economou, Professor,
Chemical and Biomolecular Engineering

Paul Ruchhoeft, Associate Professor,
Electrical and Computer Engineering

Dmitri Litvinov, Professor,
Electrical and Computer Engineering

Suresh K. Khator, Associate Dean,
Cullen College of Engineering

Michael P. Harold,
Professor and Chair,
Chemical and Biomolecular Engineering

Acknowledgments

First, I would like to thank my advisor, Assistant Professor Dr. Gila Stein for all the guidance, invaluable support and encouragement during my PhD research. With her guidance, I was able to work on different areas of research and I thank her for giving me various opportunities. I thank my committee members for their feedback and suggestions on my research.

I am thankful to the contributions from Dr. Suchanun Moungthai, Saeed Ahmadi Vaselabadi, Thai Vu, and Indranil Mitra in studying both the projects. I thank the collaborators from University of Houston, and Argonne National Laboratory for their support and the Nanofabrication Facility at University of Houston for providing access to the tools and equipment needed for my research.

I am thankful to my fellow research members Dr. Ginusha Perera, Abhijit Patel, Hui Zhen Mah, David Truong, Wendy Lang and graduate students from Chemical and Biomolecular engineering department for their informative discussions and support. I thank my friends Sravanti Addepalli, Uma Pureti, Pooja Yadav, Shweta Mehar, Sachin Dherange, Dr. Vrishank Raghav, Dr. Prasanna Dasari, Tripura Mulukutla, Dr. Meenakshi Sharma, Sujith Reddy, Maneesh Merwade, Srinivas Kumar Sunkara and others who provided me with their valuable suggestions at different stages of my PhD career.

Lastly, I would like to thank my family Dr. Ravindra Nath Mahadevapuram, Rama Devi Mahadevapuram, Dr. Rakesh Chandra Mahadevapuram and Divya Muthavarapu for the invaluable support, encouragement and endless patience.

NANOSTRUCTURED POLYMER FILMS FOR ELECTRONICS

An Abstract

of a

Dissertation

Presented to

the Faculty of the Department of Chemical and Biomolecular Engineering

University of Houston

In Partial Fulfillment

of the Requirements for the Degree

Doctor of Philosophy

in Chemical Engineering

May 2014

by

Nikhila Mahadevapuram

Abstract

Nanostructured polymer films are used as active materials in polymer-based photovoltaics, and as sacrificial materials for building nanoscale semiconductor devices. The research work described in this thesis addresses both topics.

First, we used a simple approach to cross-link the π-conjugated polymer donor using electron-beam lithography or proximity ion beam lithography. Spectroscopy measurements show light absorption properties in cross-linked polymer, therefore aromatic groups responsible for charge generation and transport are retained after the lithographic process. Gradient and nanostructured devices were fabricated to study their optoelectronic properties. Nanostructured devices showed improved device efficiency due to increase in interfacial area for charge dissociation. Cross-linked polymers are resistant to heat and solvent processing which allows the study of active layer morphology by deconstructing the nanostructured device. Structure-property relationships are established using these simple model systems. In order to have a complete understanding of cross-linked polymer, effects of radiation on molecular ordering, polymer crystal orientations and charge-carrier mobility were investigated. Cross-linked polymer system has reduced degree of crystallinity and hole mobility by almost 50%.

Second, we investigate the effects of surface and substrate interactions on self-assembly of block copolymer lamellae in thin films. The aim is to identify conditions where lamellar domains are oriented perpendicular to the substrates. Thin films of diblock and triblock copolymers were prepared on neutral substrates, which were ordered by thermal annealing. Thin films were evaluated by optical microscopy, scanning force microscopy and grazing incidence small angle X-ray scattering (GISAXS).

Domain orientations in diblock copolymer films were sensitive to annealing temperature, quality of neutral substrate and film thickness. Thin films of triblock copolymers have perpendicular domain orientation for all conditions studied due to increase in the end-segmental conformational entropy. Triblocks are much easier to orient than diblock coploymer films but both these films are associated with high density of "tilt" defects. Studies were done on diblock copolymer films prepared on different neutral substrates of varying grafting densities of polymer brushes to understand the in-plane and out-of-plane ordering. In-plane order improves with increases in the brush grafting density and film thickness. However, while out-of-plane order improves with increases in brush grafting density, it is always reduced in thicker films where the free energy penalty for bending is small. These studies demonstrate that the optimal film thickness for block copolymer lithography is equal to the lamellar periodicity.

Table of Contents

Acknowledgments . . . . . **iv**

Abstract . . . . . **vi**

Table of Contents . . . . . **viii**

List of Figures . . . . . **x**

List of Tables . . . . . **xv**

Chapter 1 Introduction **1**

Chapter 2 Direct patterning of conductive polymer domains for photovoltaic devices **7**

2.1 Introduction 7

2.2 Experimental Methods 11

2.3 Results and Discussion 16

2.4 Conclusions 30

Chapter 3 Effects of radiation on polymer crystal orientation and charge transport. **32**

3.1 Introduction 32

3.2 Experimental Methods 34
3.3 Results and Discussion 40
3.4 Conclusions 51

Chapter 4 Controlling Domain Orientations in Thin Films of AB and ABA Block Copolymers 52

4.1 Introduction 52
4.2 Experimental Methods 55
4.3 Results and Discussion 58
4.4 Conclusions 70

Chapter 5 Effects of Substrate Interactions on In-Plane and Out-of-Plane Order in Thin Films of Lamellar Copolymers . . 71

5.1 Introduction 71
5.2 Experimental Methods 72
5.3 Results and Discussion 80
5.4 Conclusions 92

Chapter 6 Outlook 93

6.1 Outlook 93

References 95

List of Figures

Figure 2.1 Direct patterning of gradient (top) and nanostructured (bottom) polymer/fullerene solar cells. 10

Figure 2.2 (a) Optical micrograph of cross-linked P3HT pads with irradiation doses in units of $\mu C/cm^2$. (b) Example of P3HT nanopillar arrays patterned with an area dose of 450 $\mu C/cm^2$. (c) Normalized residual thickness (t/t_0). 18

Figure 2.3 (a) Linear absorption coefficient (μ) measured by UV-Vis and (b) IR absorbance spectra of P3HT films at different stages in the lithographic process. 20

Figure 2.4 J–V characteristics of sequentially-cast (0 $\mu C/cm^2$) and gradient P3HT/PCBM solar cells. 22

Figure 2.5 Power-conversion efficiency (PCE) of sequentially-cast (SC) and gradient (EBL) P3HT/PCBM devices as a function of annealing time. 25

Figure 2.6 Filling P3HT nanopillars with PCBM: (a) Initial P3HT nanopillar array; (b) Partially filled pillars; (c) Almost complete filling. Internal device structure: (d) Initial P3HT nanopillar array; (e) Nanopillars after double-coat with PCBM and thermal anneal; (f) Etched to the bottom of the pillars. 27

Figure 2.7 Device deconstruction. Surface of the nanostructured P3HT/PCBM composite after removal of Al cathode (left), and after immersion in dichloromethane (right). The accompanying cartoons illustrate the active layer structure. 29

Figure 3.1 Direct patterning of polymer and device fabrication for mobility measurements. 34

Figure 3.2 (a) Optical micrograph of cross-linked P3HT pads on a silicon substrate. Irradiation doses are marked below each pad in units of $\mu C/cm^2$. (b) Normalized residual thickness (t/t_0) as a function of exposure dose for each developer. 39

Figure 3.3 (a) Linear absorption coefficient (μ) measured by UV-Vis spectroscopy and (b) Maximum value of linear absorption coefficient (μ) and also at vibronic shoulder (600 nm) are plotted. 41

Figure 3.4 (a) $\log(J)$–$\log(V)$ characteristics of as-cast P3HT device. The curves were measured under dark conditions. (b) n in the SCLC region was plotted for all devices studied. Error bars correspond to measurements from 3-4 devices for each exposure dose. 43

Figure 3.5 Hole mobility (μ_b) of all devices as a function of exposure dose. μ_b of unexposed devices are denoted at an exposure dose 0 $\mu C/cm^2$. Error bars correspond to measurements from 3-4 devices for each exposure dose. 44

Figure 3.6 (a) Corrected grazing-incidence X-ray scattering data for as-cast and exposed P3HT films. (b) Azimuthal integrated intensity (I) verses scattering vector (q) for as-cast and exposed P3HT films. 46

Figure 3.7 (a) FWHM evaluated from peak intensities at (100), (200), (300) and (010) peak positions in as-cast and exposed P3HT thin films. (b) Relative crystallite size (ϕ) for (100) and (010) in exposed P3HT films relative to as-cast. 48

Figure 3.8 (a) Pole figures for (100) peak where logarithm of peak intensity was plotted as a function of orientation angle (χ). Fits for the data are shown as a solid line. (b) Integrated peak intensity of exposed films relative to as-cast P3HT film was plotted for all doses. 50

Figure 4.1 Overview of sample preparation and types of lamellar structures that are detected in experiments. 59

Figure 4.2 Bright-field optical micrographs and atomic force microscopy phase images of ABA film surfaces. All films were prepared on high-quality neutral brushes (contact angle of 83°) and annealed for 2 days at 200°C. 60

Figure 4.3 Bright-field optical micrographs and atomic force microscopy phase images of AB film surfaces. All films were prepared on high-quality neutral brushes (contact angle of 83°) and annealed for 2 days at 200°C. 60

Figure 4.4 Fraction of perpendicular lamellae calculated from AFM images as a function of normalized film thickness. Data for "equilibrium" annealing (more than one day under low vacuum). . 62

Figure 4.5 Fraction of perpendicular lamellae calculated from AFM images as a function of normalized film thickness. Data for "nonequilibrium" annealing (10 minutes in air). 62

Figure 4.6 GISAXS data for (a) triblock and (b) diblock copolymer thin films ($t/L_0 = 2.9$) annealed at 240°C for 10 minutes. 65

Figure 4.7 Summary of maximum lamellar tilt angles ($\pm\gamma$) for all samples measured with GISAXS. 68

Figure 5.1 Schematic of sample preparation and types of lamellar structures that are detected in experiments. 77

Figure 5.2 Color maps superposed on microscopy images. Domains in PS-PMMA films were ordered by annealing at 240°C for 10 minutes. 81

Figure 5.3 (a,b) Normalized orientational correlation length (ζ/L_0) calculated from microscopy images as a function of film thicknesses and brush thicknesses. As-cast films were annealed at 240°C for 10 minutes. (b) ζ/L_0 measured throughout the PS-PMMA film. (c) Cartoon showing the tilted domains. 83

Figure 5.4 GISAXS data for diblock copolymer thin films (a) $t/L_0 = 1$ and (b) $t/L_0 = 2.5$ on three different substrates annealed at 240°C for 10 minutes. Incident angle (α_i) at which data was collected is 0.22°. 86

Figure 5.5 (a) Data and fit for first-order diffraction rod for $t/L_0 = 1$ and on three different substrates. (b) Cartoon denoting the distribution of tilt angles (σ_γ). γ is the tilt angle. (c) σ_γ was plotted as a function of film thicknesses and brush thicknesses. 88

Figure 5.6 (a) Maximum tilt angle range estimated by mapping the powder rings as a function of film thickness and brush thickness. (b) Cartoon depicts the change in tilt angle as the film thickness increases. (c) Free energy penalty for bending. 90

List of Tables

Table 2.1 Electronic performance of P3HT/PCBM solar cells after 4 minutes annealing at 170°C, unless otherwise noted. 24

Table 5.1 Material Characteristics 73

Table 5.2 Brush thicknesses and grafting densities determined with spectroscopic ellipsometry (SE) and X-ray reflectivity (XRR). . . 74

Table 5.3 Surface energy measurements for polymer brushes. 75

Table 5.4 Scaling exponent (n) for orientational correlation length as a function of film thickness, i.e., $\zeta/L_0 \sim (t/L_0)^n$ 84

Chapter 1 Introduction

Printing polymer films for organic electronics. Solar energy is one of the major alternative renewable resources of energy that is abundantly available. Inorganic semiconductors with efficiencies upto 24% have been commercially used to convert solar energy into electricity, but high manufacturing costs tend to limit this technology [1, 2]. Currently, organic photovoltaics have been extensively studied to convert the solar energy into electricity. Roll-to-roll and wet processing techniques can reduce the manufacturing costs in thin film technology. The device modules are light-weight, flexible and durable, which makes them easy to use [1–3]. However, organic photovoltaics are limited by their low power-conversion efficiency. In order to commercialize, power-conversion efficiency of 10% for a life time of 10 yrs is required [2, 4]. Most widely studied device architecture in organic photovoltaics is the bulk heterojunction (BHJ) design. BHJ morphology is an interpenetrating network of polymer donor and fullerene acceptor [5]. Polymer-fullerene system phase-separate and provide large interfacial area for charge separation and a good charge transport [6]. Efficiency reported for thin film devices are nearly 6%-8% [7, 8]. In order to improve the device efficiency systematic understanding of structure-property relations is required [5, 9].

For organic photovoltaic system, π-conjugated polymer donor absorbs light to generate excitons. Excitons are coulombically bound electron-hole pairs with the binding energy of 0.4 eV. Typical diffusion lengths of these excitons are ~ 10 nm before they recombine or decay. The generated excitons diffuse towards the donor-acceptor

interface, which provides necessary driving potential to dissociate the excitons into free charges. Free charges are then transported to the respective electrodes [5, 9].

BHJ morphology is a non-equilibrium system, which is formed by spin-casting and annealing. Processing conditions like solvent type, evaporation rates and thermal annealing influence the BHJ morphology and thus making it difficult to control. Simultaneous processes like polymer crystallization and fullerene diffusion takes places [10, 11]. Device function in BHJ were measured and several techniques were used to measure the active layer structure [8, 12–14]. The difficulty in controlling and characterizing BHJ morphology, leaves us with the challenge of understanding structure-property relations.

In order to understand organic photovoltaics, active layer morphology must be controlled. Several groups have reported techniques to control active layer morphology. Techniques like semiconducting block copolymers provide dense arrays of well defined nanostructures but controlling domain orientations in these thin films is difficult [15]. Polymer nanowires can provide high charge-carrier mobility but controlling domain size and placement is difficult [16]. Imprint lithography was used to study structure-property relations. Domain sizes were varied by using different sized stamps and improved efficiency was reported for smaller domains. This technique has limitations with respect to polymer stability through both the solvent and thermal processing steps, non uniformity of domains and fullerene filling in the nanostructures [17–19].

A model system was established to study structure-property relations, we used a simple approach to cross-link the π-conjugated polymers using electron-beam or atom-beam. Electron-beam lithography (EBL) or proximity ion beam lithography (PIBL) can be used to generate free radicals in π-conjugated polymers. Free radicals

on α-carbon are resonance stabilized. These radicals can form cross-links within the polymer matrix. The extent of cross-links can be controlled by varying the exposure dose. Uncross-linked polymer is rinsed by developing in the solvent. The heterojunction is formed by coating fullerene acceptor. The materials used in this work are, Poly (3-hexylthiophene) as polymer donor with M_w: 50 kg/mol and regio-regularity: 93% and fullerene derivative,[6,6]-phenyl-C_{61}-butyric acid methyl ester (PCBM) as acceptor. P3HT and PCBM system has been widely studied and is well documented in the literature. Indium tin oxide (ITO) was used as anode, aluminum (Al) as cathode and PEDOT:PSS = poly(3,4-ethylenedioxythiophene):poly-(styrenesulfonate) as hole injecting layer. The goals of the project are:

- Control active layer morphology, (a) Use Electron-beam lithography (EBL), or Proximity ion beam lithography (PIBL)(b) Study lithographic properties of polymer donor.

- Study structure-optoelectronic properties in cross-linked polymer systems, (a) Light absorption, charge generation, and charge transport (b) Active layer morphology and device function in both devices, (i) Bilayer device (ii) Nanostructured device.

- Study molecular ordering in cross-linked polymer (a) Polymer crystal orientation (b) Charge-carrier mobility.

Nanopatterning using thin films of block copolymers. Thin films of block copolymer (BCP) have been studied to pattern features with size and periodicity in the range of 10-100 nm [20]. They can be used as templates for pattern transfer in lithographic processes [21]. Block copolymer are polymer systems where two chemically distinct blocks are covalently linked. These block copolymers can micro phase

separate and self-assemble into different ordered nanostructures [22]. Thermodynamics drives pattern formation in these systems, therefore less energy intensive than top-down lithographic processes and hence inexpensive [20, 23, 24].

In thin films of block copolymers, the effects of interface play an important role. These films show preferential wetting at the interfaces if the surface energetics are not balanced. Several groups have studied various techniques to avoid preferential wetting at the substrate by coating with polymeric cross-linked surface [25], random copolymer brushes [26] or surface active random copolymer [27]. Film thickness of the block copolymers can also significantly influence the domain orientations. Films with thickness that are incommensurate with asymmetric boundary conditions and/or after annealing at high temperatures can form perpendicular domains on neutral substrates [28, 29].

In order to use thin films of block copolymers as templates, domain orientations have to be controlled [23]. Theoretical studies from several groups suggested that copolymer architecture can influence the domain orientations in thin films of block copolymers [30]. Triblock copolymers can orient easily when compared to diblock copolymers due to broad distribution of chain end which result in increased end-segmental configurational entropy [31]. Out-of-plane defects have to be minimized to be able to use these systems as pattern transfer mask without significant errors in feature size and placement [32].

In our present work we use block copolymer systems of polystyrene (PS) and poly(methyl methacrylate)(PMMA) as model systems. In order to avoid preferential wetting at the substrate, silicon substrates were coated with random copolymer brushes and polymer films are annealed at high temperatures to allow domain ordering.

Goals for the project are:

- Study the effects of copolymer architecture on surface energetics and domain orientations using thin films of diblock and triblock copolymers.
- Study the effects of block copolymer-substrate interactions on in-plane and out-of-plane ordering in thin films of diblock copolymers.

The thesis is divided into 6 chapters with chapter 1 stating the overview of the projects studied in my PhD research. Chapter 2 and 3 discusses the studies done on printing polymer films for organic electronics. Chapter 4 and 5 discusses the studies done on nanopatterning using block copolymer self-assembly.

Chapter 2 discusses the simple approach to control the morphology using electron-beam lithography in polymer based solar cells. Exposed polymer was then investigated for its lithographic and optoelectronic properties. Devices were constructed using this approach. These model systems provide a fundamental understanding of structure-property relations.

Chapter 3 discusses the effects of radiation on polymer structure and charge transport. This helps in understanding completely the model system built using electron-beam or atom-beam. Molecular ordering, polymer crystal orientation and charge transport were studied in polymer systems after electron-beam or atom-beam exposure.

Chapter 4 studies the effect of copolymer architecture on domain orientation in thin films of block copolymers. Thin films of diblock and triblock copolymers were used to study the domain orientation under different processing conditions.

Chapter 5 studies the effect of underlying substrate on in-plane and out-of-plane ordering in thin films of diblock copolymers. In-plane ordering improves as the block

copolymer thickness increases and detailed study on out-of-plane ordering was done.

Chapter 6 is the Outlook. This chapter introduces topics of interest for potential future work in these areas of research.

Chapter 2 Direct patterning of conductive polymer domains for photovoltaic devices

2.1 Introduction

Polymer solar cells are attractive for clean energy production because they can be fabricated in light-weight, flexible, durable, and inexpensive modules. The most efficient devices are based on the bulk heterojunction (BHJ) design [5, 33]. BHJs are prepared by arresting the phase separation of a polymer-fullerene (donor-acceptor) blend. The resulting structure is a nanoscale, interpenetrating network that offers a large interfacial area for charge generation and a good pathway for charge transport to the electrodes. Currently, it is unclear what aspects of the BHJ structure are controlling device function, because it is difficult to control and characterize the formation of these highly non-equilibrium morphologies. BHJs are usually prepared by spin-casting from volatile solvents, and the as-cast structure is very sensitive to the solvent quality, evaporation rate, solution concentration, and ambient temperature. BHJ growth kinetics are controlled by a coupled crystallization-diffusion mechanism, so key parameters such as domain size, phase purity, polymer crystallinity, and interfacial area cannot be varied independently. Additionally, the BHJ morphology is disordered and anisotropic at both molecular and nanometer length scales, and this feature complicates measurement of the structure with scattering or microscopy [8]. As a result of these challenges, there is wide debate about the optimal design attributes for polymer-based solar cells. It is generally agreed that charge generation is optimized when the

phase separation length scale is comparable to the exciton diffusion length, which is approximately 10 nm for most polymer semiconductors. However, even when the average BHJ domain size meets this criteria, the film contains defects such as regions of complete polymer/fullerene miscibility, domains that are larger than the exciton diffusion length, and incomplete paths to the electrodes [8]. These defects are responsible for carrier losses through trapping, recombination, or photoluminescence, making it difficult to accurately interpret spectroscopic and optoelectronic measurements. Furthermore, while most works indicate that highly-crystalline polymers will enhance light absorption and carrier transport, there are examples of good optoelectronic function in low-crystallinity systems [34, 35]. This discrepancy is explained by the coupling between crystallinity, domain size, and interfacial area in a BHJ device, making it difficult to determine which parameter is controlling the observed photocurrent. It is critical to develop model systems where different structural parameters can be independently interrogated.

A variety of experimental methods have been developed that offer control over the nanoscale morphology [36]. Examples include self-assembly of block copolymer semiconductors [15,37,38], polymer nanowire growth [16,39,40], and imprint lithography [17, 18, 41–44]. Block copolymers provide a simple route to generate dense arrays of nanostructures, but it is difficult to control domain orientations throughout the film thickness. Furthermore, critical properties such as domain size, interfacial width, and crystallinity are all coupled to the copolymer composition and molecular weight [45]. The growth of crystalline polymer nanowires will produce high-mobility nanoscale domains [16, 39, 40, 46], but does not afford precise control over wire diameters, orientations, or placement. Recently, several groups have used imprint lithography to build polymer-based heterojunctions with well-defined morphologies [17–19,36,41,43,44,47].

Such top-down lithographic techniques provide control over domain sizes and interfacial area, which is helpful to understand the effects of active layer structure on optoelectronic function. For example, these studies have demonstrated that matching the domain size to exciton diffusion lengths can enhance photocurrent generation [18,43]. However, imprint lithography has a few limitations. First, master stamp fabrication is difficult and expensive, particularly when the desired pattern is a large-area array of sub-20 nm nanostructures. Imprint lithography is an excellent strategy for repetitive printing of a single design, but this approach can be costly and time-consuming when many different designs are under investigation. Second, the thermal and mechanical properties of organic semiconductors are not optimized for imprinting. This means that imprinted nanostructures have limited stability through solvent processing or heat treatments, and it is difficult to generate nanostructures with high aspect-ratios (width:height > 2) [18]. Finally, imprinting will induce alignment of the polymer chains within the template [41], so polymer crystallinity and grain orientations will be coupled to the design of the stamp.

In this work, we report a flexible approach to control the morphology of polymer/fullerene heterojunctions. Thin films of π-conjugated polymers are directly patterned with electron-beam lithography (EBL). This process initiates a localized, *in-situ* cross-linking reaction that generates conductive nanostructures or microstructures. The image is developed by immersion in an organic solvent, and then the cross-linked polymer structures are coated with a soluble fullerene to complete the heterojunction. This protocol allows for independent variation of domain size and shape, interfacial area, and phase purity. The lithographic process is compatible with commercially-available materials such as different types of poly(3-alkylthiophene) and poly(phenylene vinylene). Polymer cross-link density can be tuned *on-demand* by

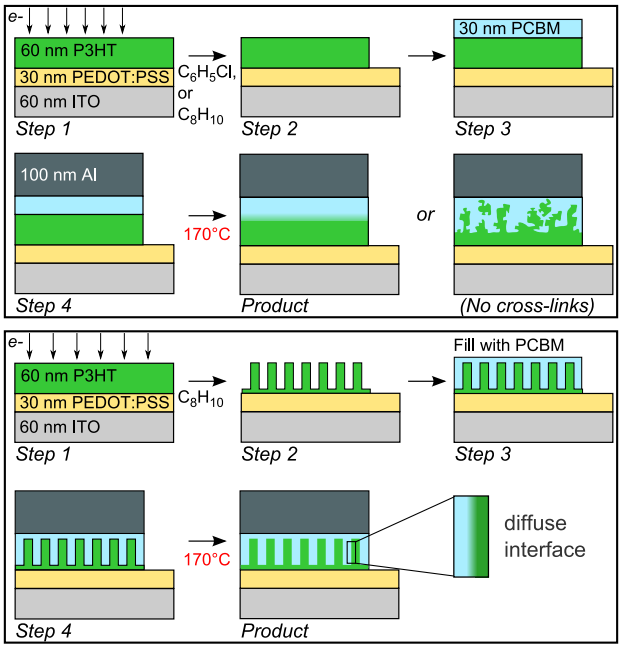

Figure 2.1: Direct patterning of gradient (top) and nanostructured (bottom) polymer/fullerene solar cells.

varying the exposure dose, providing a simple route to engineer high-performance nanostructures that are stable through solvent and thermal processing. Furthermore, after evaluating the spectroscopic and optoelectronic properties of these devices, the heterojunction morphology can be measured with microscopy by "deconstructing" the active layer. While EBL is too slow for manufacturing, this technology is very valuable for structure–property investigations: EBL patterns are defined with Computer-Aided Design ("maskless"), so different types of designs can be rapidly evaluated. State-of-the-art EBL systems require a substantial capital investment, but the data presented in this report were acquired with a scanning electron microscope equipped with a Nanometer Pattern Generation System.

The materials used in this work are poly(3-hexylthiophene) (P3HT) and [6,6]-phenyl-C_{61}-butyric acid methyl ester (PCBM), which are benchmark donor and acceptor chemistries, respectively. This report is divided into three parts. First,

we investigated the lithographic properties of P3HT films. We find that P3HT is a high-resolution, negative-tone resist. Second, we measured irradiated P3HT films with ultraviolet-visible (UV-Vis) and infrared (IR) absorbance spectroscopies. These data confirm that patterned P3HT films retain the π-bonds responsible for light absorption, charge generation, and charge transport. Third, we evaluated the electronic performance of patterned P3HT films in "gradient" and nanostructured P3HT/PCBM heterojunctions (see 2.1). The device consists of layers of indium tin oxide (ITO), poly(3,4-ethylenedioxythiophene):poly(styrenesulfonate) (PEDOT:PSS), poly(3-hexylthiophene)(P3HT), [6,6]-phenyl-C_{61}-butyric acid methyl ester (PCBM). PCBM is spin-cast from dichloromethane. The power-conversion efficiency of lithographically-defined heterojunctions improves with increasing polymer/fullerene interfacial area. These results establish a model system for structure–function studies of polymer-based solar cells, where domain size and interfacial area can be varied independently of polymer crystallinity.

2.2 Experimental Methods

Active Materials. Poly(3,4-ethylenedioxythiophene):poly(styrenesulfonate) (PEDOT:PSS) was purchased from Baytron (product PH500, 1 wt% aqueous dispersion). The PEDOT:PSS dispersion was diluted with two parts deionized water and then filtered with a 0.45 μm glass microfiber mesh. Poly(3-hexylthiophene) (P3HT) was purchased from Rieke Metals (90-94% regio-regular, number-average molecular weight of 30 kg/mol, polydispersity index of 1.8). P3HT was dissolved in anhydrous chlorobenzene at a concentration of 0.014 g/mL and filtered three times with a 0.2 μm Teflon mesh. [6,6]-phenyl-C_{61}-butyric acid methyl ester (PCBM) was purchased

from Nano-C. PCBM was suspended in anhydrous dichloromethane at concentrations of 0.005 or 0.015 g/mL and filtered three times with a 0.2 μm Teflon mesh. Note that high PCBM concentrations are needed to fill nanostructured devices, while low PCBM concentrations are used for gradient or sequential casting designs.

Electron-Beam Lithography. Microscale P3HT/PEDOT:PSS pads (45 μm $\times$ 45 μm) are patterned with a 30 keV, 12 nA electron beam using a FEI XL-30FEG field emission scanning electron microscope (SEM) equipped with a 5 MHz Nanometer Pattern Generation System [48]. Exposures are implemented with a square grid based on a 30 nm pixel size. Doses are varied in the range of 100 to 2000 μC/cm^2. These microstructures are used for two tasks: (i) Lithographic contrast is evaluated by measuring the residual thickness of isolated pads; and (ii) gradient heterojunctions are built by stitching together arrays of pads to span a total area of 2 mm $\times$ 2 mm. This report also includes data for P3HT nanopillars. For the example in Figure 2.2, the nanopillars are printed in a square grid (250 nm pitch) with a focused 50 pA beam. Patterning with this low beam current demonstrates that P3HT is a high-resolution resist. To fabricate devices, the nanopillars are printed in a single-pass with a 400 nm pitch. These exposures use a 12 nA beam (fast) to build nanostructured heterojunctions that span 3 mm $\times$ 2 mm. A detailed discussion of EBL exposure schemes is included elsewhere [49]. Note that SEM-based lithography does not have dynamic focus corrections, so P3HT films are nanopatterned with a slightly defocused beam to minimize variations in feature size.

P3HT Pattern Development. P3HT patterns are developed in a nitrogen-purged glove box following one of two procedures. (1) Immersion in chlorobenzene for 25 seconds at room temperature, using a standard Pyrex beaker; or (2) immersion in

p-xylenes for 25 seconds at 35 °C, using a Teflon beaker with nitrogen bubbler. Note that samples are usually developed 12–24 hours after patterning. It is possible that the post-exposure delay will impact the lithographic resolution and/or optoelectronic properties of P3HT.

Microscopy. The structure of patterned P3HT films is measured with Atomic Force Microscopy (AFM) using a MultiMode 3 (Veeco) in Tapping Mode. AFM probes are silicon with a spring constant of 40 N/m, and these tips are most effective when functionalized with hexamethyldisiloxane (to minimize adhesive interactions with the polymer). The structures of microscale and millimeter-scale features are evaluated with a Nikon Eclipse LV100 optical microscope (bright-field optics).

Spectroscopy. Irradiated P3HT and PEDOT:PSS films are characterized with ultraviolet-visible (UV-Vis) and infrared (IR) absorbance spectroscopies. Samples are prepared by spin-casting thin films on 100 nm thick silicon nitride membranes. P3HT and PEDOT:PSS film thicknesses are approximately 60 nm and 30 nm, respectively. All data are collected in transmission mode at normal incidence (approximately). UV-Vis absorbance is recorded with a Shimadzu UV-2401PC spectrophotometer (200-800 nm), and infrared absorbance is measured with a Nicolet 6700 spectrometer. The signal from a clean silicon nitride membrane was also measured and subtracted from the spectra shown in Figure 2.3. Note that five to ten samples were measured at each stage in the lithographic process.

Gradient Heterojunctions. Substrates are glass microscope slides coated with 60-100 nm of indium tin oxide (ITO, 15-25 Ω/Sq, Sigma Aldrich). Substrates are cleaned by sonication for 20 minutes in each of the following solutions: 2% Hellmanex

II detergent, deionized water, and isopropanol. Substrates are then immediately dried in a clean nitrogen stream. PEDOT:PSS films with thickness (25 ± 5) nm are spun-cast in air on top of the ITO anode, then baked for 10 minutes at 140 °C. Substrates are transferred to a nitrogen-purged glove box and the ITO/PEDOT:PSS stack is coated with a (60 ± 5) nm P3HT film. In some cases the P3HT film is pre-baked at 150°C for 2 min (to remove residual solvent). The active layer is built following the scheme in Figure 2.1. First, samples are transferred to the electron-beam lithography instrument for cross-linking. Second, samples are transferred back to the nitrogen-purged glove box for image development. Third, PCBM films with thickness (32 ± 5) nm are spun-cast on top of the patterned P3HT films from 0.005 g/mL suspensions in dichloromethane. Fourth, samples are transferred to a thermal evaporator for deposition of a 100 nm thick Aluminum (Al) cathode. Last, samples are returned to the glove box to thermally-anneal the active layer at 170 °C for up to 6 minutes. Note that samples are transferred between instruments using a portable chamber that is pressurized with nitrogen.

Nanostructured Heterojunctions. Nanostructured heterojunctions are built with the scheme illustrated in Figure 2.1, which is similar to the procedures for gradient heterojunctions. The key steps that differ for nanostructured devices are as follows: Prior to EBL, the P3HT films are baked at 150°C for 2 minutes. P3HT nanostructures are developed with *p*-xylene at 35°C for 25 seconds; the developer is purged with nitrogen to displace dissolved oxygen. The PCBM spin-casting step is performed twice using a 0.015 g/mL suspension of PCBM in dichloromethane. We found that a "double-coat" process was more effective at filling the void space around the pillars (see Figure 2.6). The PCBM layer on top of nanostructures was 20–40 nm thick. After measuring the electronic function, the Al cathode is dissolved

with aqueous potassium hydroxide (45 wt%) and then PCBM is washed out with dichloromethane. Device "deconstruction" is very valuable for confirming the P3HT nanostructures are intact after all processing steps.

Bulk Heterojunctions. BHJs are prepared with the same anode and cathode as gradient or nanostructured devices. The only step that differs is casting of the active layer. P3HT and PCBM are dissolved in a 1:1 ratio (weight basis) in anhydrous chlorobenzene (concentration of 0.01 g/mL). The solution is filtered three times with a 0.2 μm Teflon mesh, and then a 100 nm thick film is spun-cast on top of the PEDOT:PSS/ITO anode.

Sequential Casting Heterojunctions. These devices are prepared with the same anode and cathode as all other devices. The only step that differs is casting of the active layer. P3HT films are spun-cast on the PEDOT:PSS film with thickness (60$\pm$5) nm, and the PCBM is spun-cast on top with thickness (32$\pm$5) nm. The concentration of PCBM in dichloromethane is 0.005 g/mL.

Etching. We used oxygen plasma to etch through the active layer so we could evaluate the internal structure. The oxygen plasma was generated with a Oxford Plasma Lab 80 Plus Reactive Ion Etch system (100 W, 20 sccm, 20 mTorr, DC bias of 230 V). The etch rates for P3HT and PCBM are approximately 0.75 nm/sec and 0.5 nm/sec, respectively, so the P3HT pillars appear shorter than the surrounding PCBM.

Electronic Characterization. All electronic measurements are conducted in a nitrogen-purged glove box at 28°C. Devices are illuminated with a 150 W solar simulator (Oriel) equipped with an air mass 1.5 global filter. The lamp power is calibrated to 100 mW/cm^2 using a silicon reference solar cell equipped with KG5 filter (certified by the National Renewable Energy Laboratory, VLSI Standards) [50]. Current-voltage characteristics are recorded with a Keithley 2601A source meter. Power-conversion efficiency (PCE) is calculated from the open-circuit voltage (V_{oc}), short-circuit current density (J_{sc}), fill factor (FF), and input power (P) in the usual way [50]:

$$PCE = V_{oc} J_{sc} FF / P. \tag{2.1}$$

To convert from current to current-density, the device active area is calculated from the cathode area (measured from analysis of optical micrographs). Typical active areas are 0.03-0.05 cm^2.

2.3 Results and Discussion

Lithography. Our first aim was to evaluate the sensitivity of P3HT to electron-beam radiation. Thin films of P3HT were patterned with EBL and the relief images were developed with chlorobenzene (room temperature) or *p*-xylene (35°C). Note that *p*-xylene is purged with nitrogen to displace dissolved oxygen. Figure 2.2(a-b) includes examples of microscale and nanoscale P3HT patterns. Average pillar diameter and height are 50 nm and 60 nm, respectively. Image was acquired with an atomic force microscope operating in tapping-mode, and Figure 2.2(c) reports the normalized residual thickness as a function of exposure dose for chlorobenzene (square) and

p-xylene (triangle) developers. We find that P3HT is a high-resolution, negative-tone electron-beam resist. The critical exposure dose at 30 keV is approximately 400 μC/cm^2, which is slightly lower than poly(methyl methacrylate) or hydrogen silsesquioxane electron-beam resists [51], [52]. It is difficult to evaluate the resolution limit for P3HT because our EBL system does not have instrumentation for dynamic focus corrections. However, we find that nanodots and nanolines with 50 nm widths are reliably resolved using a low beam current, and we anticipate that even smaller features can be printed with a more sophisticated EBL system and/or an optimized development protocol [51], [53]. We also evaluated the sensitivity of poly(3,4-ethylenedioxythiophene):poly(styrenesulfonate) (PEDOT:PSS) to electron-beam radiation. This material is used as a hole-injection layer at the anode (see Figure 2.1) and is therefore irradiated during the fabrication process. We find that PEDOT:PSS is also a negative-tone material, but with a low critical exposure dose of 200 μC/cm^2 for development in water. It is important to note that critical exposure doses are very sensitive to polymer molecular weight. For example, increasing the molecular weight of P3HT will reduce the required dose.

Spectroscopy. Our second aim was to determine if irradiated P3HT films retain the π-bonds responsible for optoelectronic function. There are several studies that have considered P3HT as a resist for optical lithography, where irradiation in air will initiate complex photooxidation reactions that result in cross-linking and loss of conjugation [54–57]. Our studies differ because EBL is implemented under ultra high vacuum (10^{-7} Torr). The irradiated sample volume is very small, and this prevents detailed characterization of the bond structure with nuclear magnetic resonance or

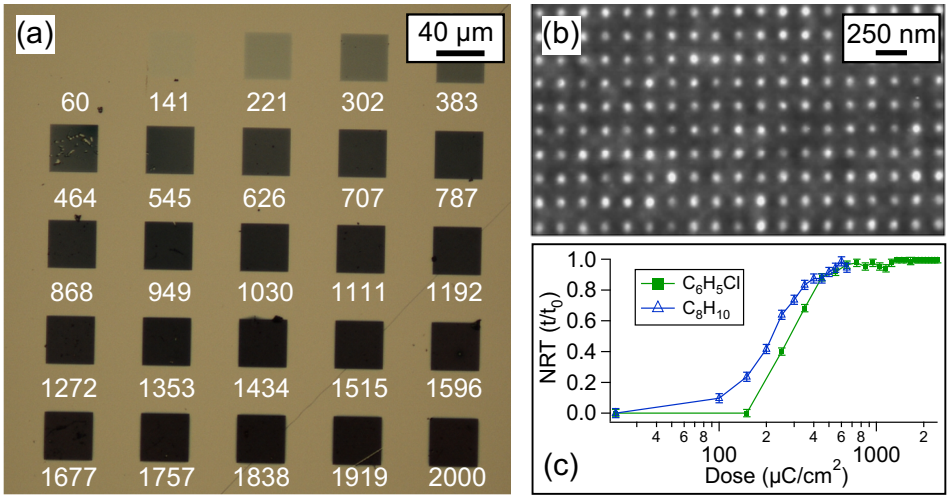

Figure 2.2: (a) Optical micrograph of cross-linked P3HT pads with irradiation doses in units of μC/cm^2. (b) Example of P3HT nanopillar arrays patterned with an area dose of 450 μC/cm^2. (c) Normalized residual thickness (t/t_0).

x-ray photoelectron spectroscopies. Instead, we used UV-Vis and IR absorbance spectroscopies to evaluate the properties of un-exposed films, irradiated films, and irradiated films after immersion in developer. Representative UV-Vis and IR absorbance data are included in Figure 2.3 for five samples: An as-cast P3HT film, a "pre-baked" P3HT film that was thermally-annealed for 2 minutes at 150°C, a pre-baked P3HT film that was irradiated at 450 μC/cm^2, and pre-baked P3HT films that were irradiated at 450 μC/cm^2 and then immersed in chlorobenzene or *p*-xylene. These data are normalized to account for variations in film thickness. First, the linear absorption coefficients (μ) for as-prepared and irradiated P3HT films are nearly identical. This finding is consistent with work from Gearba et al., where thin P3HT films were thermally cross-linked with a peroxide radical initiator, and there was no change in UV-Vis absorbance at low-to-moderate cross-link densities [58]. However, we do find evidence of photobleaching when irradiated films are immersed in the developer. The

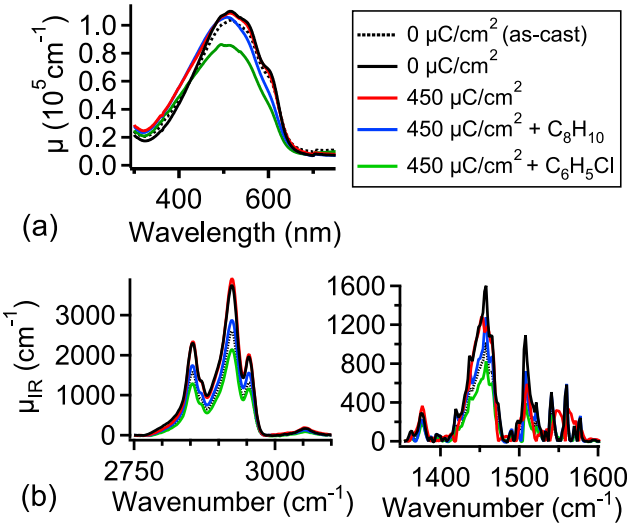

Figure 2.3: (a) Linear absorption coefficient (μ) measured by UV-Vis and (b) IR absorbance spectra of P3HT films at different stages in the lithographic process.

wavelength at peak absorbance is (515 ± 2) nm, (513 ± 2) nm, and (509 ± 2) nm for as-prepared, irradiated, and developed films, respectively.[1] In addition to this blue-shift, developed films absorb less light and exhibit weaker vibronic shoulders [59, 60]. The loss of fine structure suggests that development partly disrupts the intermolecular ordering, and this conclusion is supported by preliminary grazing-incidence wide-angle X-ray scattering (GIWAXS) data. Second, the IR spectra for as-prepared and irradiated films are nearly identical. Peaks associated with hydrocarbon and aromatic functional groups are resolved in the ranges 2850-3050 cm^{-1} and 1370-1560 cm^{-1}, respectively, although the latter fingerprint region is quite noisy. All peak intensities are weaker after development, which is expected based on the reduced film thickness, but this finding is also consistent with polymer degradation [57, 61].

It is difficult to identify the P3HT cross-linking reaction using UV-Vis and IR absorbance data. We have hypothesized a mechanism that is consistent with other

[1] Average values and standard deviations are calculated from measurements of five to ten samples at each step in the process.

studies [61, 62]. For the purposes of this discussion, it is important to note that electron beams will ionize the polymer to generate radicals. The data reported in Figure 2.2 demonstrate that some of these radicals combine to form intermolecular cross-links. P3HT is a semi-crystalline polymer with a glass transition temperature near 12°C [63], although this number is widely debated [64, 65], so cross-links are most likely formed in the amorphous regions where the polymer has greater segmental mobility. There is a high probability that some radicals remain trapped in the polymer, and a subsequent reaction during development could explain the changes in UV-Vis and IR absorbance that are summarized in Figure 2.3. Indirect evidence of trapped radicals is seen, where a post-exposure bake at elevated temperature increases the size of the nanostructures–meaning, baking enhances the polymer mobility so more radicals can meet and react. One possibility is that trapped radicals can react with dissolved oxygen in the solvent. The IR measurements do not detect any oxidation products such as carbonyl and hydroxyl moieties, but the UV-Vis spectra suggest that purified *p*-xylene can minimize photobleaching compared with out-of-the-bottle chlorobenzene. Another possibility is that residual iron catalyst from the polymer synthesis is sensitized by electron-beam radiation, generating free radicals that could attack the thienyl ring and reduce the extent of conjugation [61]. This explanation is consistent with UV-Vis and IR absorbance spectra. Further investigations are underway to identify the photobleaching mechanism and address this challenge.

With regards to PEDOT:PSS, irradiation slightly increases the UV-Vis absorbance at 437 nm, while no clear changes are detected in IR absorbance spectra. Other works suggest that low-energy electrons (ca. 3 eV) can induce oxygen and sulfur loss from PSS and disrupt carbon-oxygen bonds in PEDOT [66], while the thiophene rings are unaffected by irradiation. We find that irradiated PEDOT:PSS

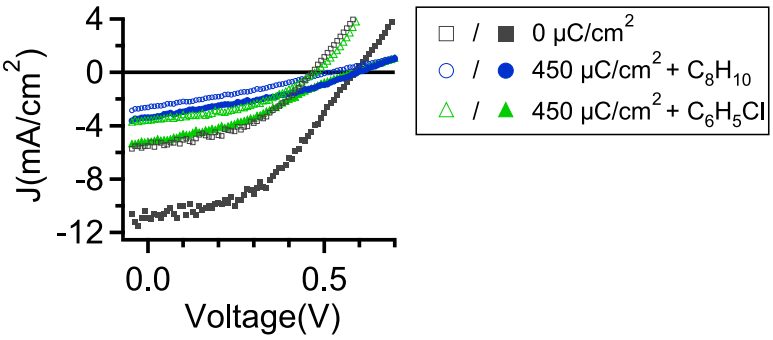

Figure 2.4: J–V characteristics of sequentially-cast (0 μC/cm^2) and gradient P3HT/PCBM solar cells.

films are insoluble in water, which is consistent with a reduction of PSS solubility due to sulfonate damage and/or intermolecular cross-linking through ionization of the polymers.

Optoelectronic Function. Our final aim was to characterize the electronic performance of lithographically-patterned P3HT films in P3HT/PCBM solar cells. We built "gradient" and nanostructured P3HT/PCBM heterojunctions following the schemes in Figure 2.1. The variables in these experiments were exposure dose and type of developer: Patterns were defined with an area dose of 300, 450, or 600 μC/cm^2, and then developed with either chlorobenzene or *p*-xylene. We also prepared two types of samples that were not exposed to electron-beam radiation: BHJs based on P3HT/PCBM blends, and devices that were prepared by sequential casting of P3HT and PCBM layers from orthogonal solvents [67–69]. Table 2.1 summarizes the average photovoltaic response for all devices after annealing for 1–4 minutes at 170°C. BHJ = bulk heterojunction, SC = sequential casting, Gr = Gradient, NP = Square grid of nanopillars with 400 nm pitch, MNL = Modulated nanolines with a 400 nm pitch. *Only one device was prepared in this manner, so we do not report the uncertainty. †Data are reported for 1 minute of annealing at 170°C. $^\triangleright$Devices developed

Table 2.1: Electronic performance of P3HT/PCBM solar cells after 4 minutes annealing at 170°C, unless otherwise noted.

Design	Dose (μC/cm^2)	V_{oc} (V)	J_{sc} (mA/cm^2)	FF	PCE (%)
BHJ	0	0.60 ± 0.01	8.86 ± 3.01	0.46 ± 0.06	2.45 ± 0.85
SC	0	0.56 ± 0.04	7.59 ± 2.48	0.43 ± 0.03	1.85 ± 0.73
Gr$^{\triangleright}$	300	0.56 ± 0.01	2.67 ± 1.32	0.36 ± 0.03	0.55 ± 0.33
Gr$^{\triangleright}$	450	0.57 ± 0.04	3.07 ± 1.25	0.35 ± 0.01	0.61 ± 0.27
Gr$^{\triangleright}$	600	0.58 ± 0.02	1.51 ± 0.66	0.34 ± 0.01	0.30 ± 0.15
Gr$^{\blacktriangleright}$	300	0.58 ± 0.03	1.47 ± 0.32	0.34 ± 0.01	0.29 ± 0.08
Gr$^{\blacktriangleright}$	450	0.59 ± 0.02	1.24 ± 0.30	0.36 ± 0.03	0.33 ± 0.10
Gr$^{\blacktriangleright}$	600	0.60 ± 0.02	1.38 ± 0.02	0.35 ± 0.02	0.29 ± 0.01
NP$^{\dagger,\blacktriangleright}$	450	0.60 ± 0.01	1.79 ± 0.16	0.40 ± 0.03	0.43 ± 0.02
MNL$^{\star,\dagger,\blacktriangleright}$	450	0.61	1.78	0.47	0.51

in C_6H_5Cl. $^{\blacktriangleright}$Devices developed in C_8H_{10}. Figure 2.4 shows the J–V characteristics of sequentially-cast (0 μC/cm^2) and gradient P3HT/PCBM solar cells. The curves were measured under AM1.5G white light illumination at 100 mW/cm^2. Open/closed symbols correspond with no annealing and 4 min thermal annealing at 170°C, respectively. Before discussing the lithographically-defined heterojunctions, we note that the electronic characteristics of BHJ and sequentially-cast samples are very similar. This finding indicates that sequential casting generates a bicontinuous morphology during thermal annealing [68–70], which is expected based on the well-documented miscibility of P3HT and PCBM and fast inter-diffusion rates [14,71,72]. We also note two significant differences between our work and others in the literature. First, the device active areas are small (ca. 0.03-0.05 cm^2), so edge effects could inflate the measured short-circuit current density [73,74]. Second, the cathode is Al rather than the optimal LiF/Al design, and this leads to inferior power-conversion efficiency [75,76]. With these factors in mind, the device characteristics in this report should be compared against each other rather than other works.

The power-conversion efficiencies (PCE) of sequentially-cast devices is denoted by 0 μC/cm^2 (diamonds), and PCE of lithographically-defined gradient devices is reported as a function of dose and type of developer (circles, triangles, and squares) in Figure 2.5. The PCE of lithographically-defined gradient devices range from 0.3-0.6%, while the PCE of BHJ and sequentially-cast samples is approximately 2%. This difference stems from smaller fill factors (FF) and short-circuit current densities (J_{sc}) when the active layer is built with EBL. The open-circuit voltage (V_{oc}) is not affected by the lithographic process. There are two likely causes for diminished electronic performance of electron-beam patterned heterojunctions. First, the lithographic process may change the P3HT chemistry. The data included in Figure 2.3 demonstrate that patterned P3HT films are adversely affected by development and absorb less light. Irradiation could have other consequences that are not yet understood, such as introduction of trap states that reduce the carrier mobility. Second, cross-linking the P3HT film will prevent the formation of a nanoscale P3HT/PCBM network during thermal annealing. The smaller interfacial area in gradient devices will reduce the density of photo-generated charges. We note that other studies of planar P3HT/PCBM heterojunctions report similar values for PCE (ca. 0.5%) in the absence of P3HT-PCBM interdiffusion [18, 70], although it is difficult to compare these data against ours due to the differences in device layout and processing methods.

The spectroscopy data in Figure 2.3 suggest that purified *p*-xylene is more effective at suppressing photobleaching than chlorobenzene. However, as summarized in Table 2.1, development with chlorobenzene can yield higher values of PCE than *p*-xylene. This finding might suggest that chlorobenzene is the better developer, but there are two observations that lead us to select *p*-xylene instead. First, there is less sample-to-sample variability when developing with *p*-xylene compared with

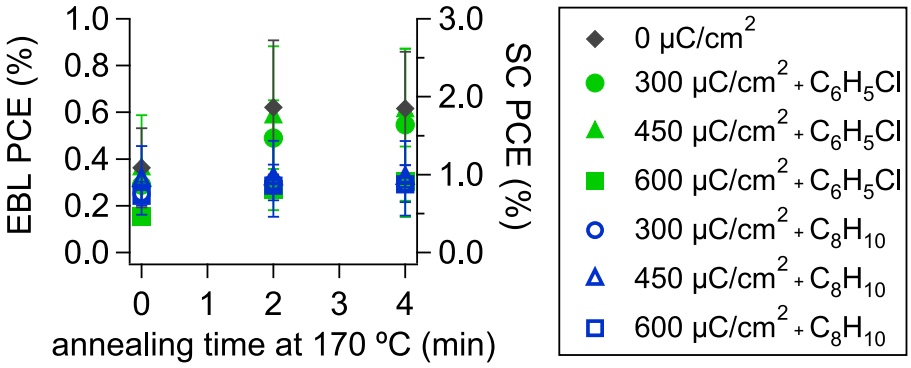

Figure 2.5: Power-conversion efficiency (PCE) of sequentially-cast (SC) and gradient (EBL) P3HT/PCBM devices as a function of annealing time.

chlorobenzene. These statistics are included in 2.1. Second, development with *p*-xylene yields heterojunctions with better thermal stability than chlorobenzene. Table 2.4 reports the current density–voltage ($J-V$) characteristics of sequentially-cast and gradient devices, both before and after thermal annealing for 4 minutes at 170°C. Figure 2.5 reports the power-conversion efficiency as a function of annealing time for all gradient devices. The same trends are observed for sequentially-cast devices and gradient heterojunctions that were developed with chlorobenzene: After annealing, the PCE is doubled due to improvements in V_{oc}, FF, and J_{sc}. In contrast, gradient heterojunctions that were developed with *p*-xylene are nearly unchanged by subsequent thermal annealing (approximately 10% improvement in PCE).

The average electronic characteristics of lithographically-defined gradient heterojunctions are independent of exposure dose, although sample-to-sample variability is minimized by increasing the exposure dose. Such improvements in reproducibility are explained by the lithographic contrast curve in Figure 2.2. The slope of the contrast curve is a maximum when the exposure dose is between 200 and 400 μC/cm^2, which means that a slight variation in beam current or development time will change the residual thickness of the P3HT film. The contrast curve is flat when the dose exceeds

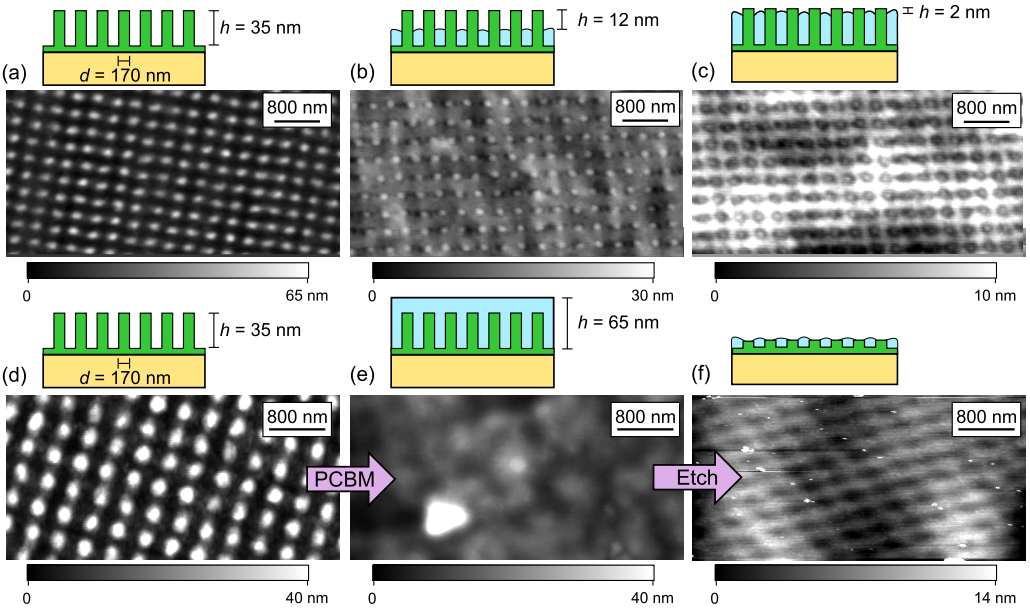

Figure 2.6: Filling P3HT nanopillars with PCBM: (a) Initial P3HT nanopillar array; (b) Partially filled pillars; (c) Almost complete filling. Internal device structure: (d) Initial P3HT nanopillar array; (e) Nanopillars after double-coat with PCBM and thermal anneal; (f) Etched to the bottom of the pillars.

500 μC/cm^2, so the process is less sensitive to human error above this threshold. Other studies have demonstrated that PCE in gradient P3HT/PCBM heterojunctions is very sensitive to the thickness of P3HT films, and variations at the scale of 10 nm can change J_{sc} by a factor of 2 [77]. This sensitivity to film thickness might explain why J_{sc} seems to vary with the type of developer, because the residual film thickness will differ for chlorobenzene and *p*-xylene.

We used electron-beam patterning to build nanostructured heterojunctions based on arrays of P3HT nanopillars. The diameter and height of these P3HT pillars are approximately 220 nm and 35 nm, respectively, and the pitch is 400 nm. The patterns were exposed with an area dose of 450 μC/cm^2 and then developed with *p*-xylene. This process leaves approximately 40 nm of cross-linked P3HT underneath the pillars, a consequence of electron scattering events, so the anode is coated with

a continuous P3HT film (see Figure 2.1). The P3HT nanostructures are then spin-coated with PCBM. We found that PCBM tends to dewett from the top edges of the pillars, and measurements of this phenomena are included in Figure 2.6(a-c). This problematic behavior is mitigated by "double-coating" PCBM, which fills the voids and generates a top-coat that is 20–40 nm thick for most devices (described in the Experimental Procedures). We evaluated the internal structure of these "double-coated" heterojunctions with successive etching and imaging steps, and we determined that PCBM infiltrates the void space and contacts the P3HT pillars throughout the active layer thickness. These data are reported in Figure 2.6(d-f).

The average PCE for nanopillar devices is approximately 30% larger than the gradient heterojunctions due to enhancements in J_{sc} and FF. While the lithographic process may change the chemistry of P3HT, these effects are similar for gradient and nanostructured devices. Therefore, we attribute the improved performance of nanopillar devices to the ca. 15% increase in polymer/fullerene interfacial area. Tuning the nanopillar dimensions could further improve the PCE: Currently, the nanopillar diameter is much larger than the exciton diffusion length [78], and the nanopillar height is smaller than the P3HT absorption length.

Uniquely, after measuring the J–V characteristics of nanostructured devices, we deconstructed the active layer to image the morphology. Deconstruction is a simple, two-step process: The Aluminum cathode is removed with a drop of aqueous potassium hydroxide solution, and then the PCBM phase is washed away with dichloromethane. Figure 2.7 reports atomic force microscopy measurements for each step of the deconstruction process, and the accompanying cartoons illustrate the device structure. The deconstruction process facilitates correlation of active layer morphology and optoelectronic performance. For example, we found one device where

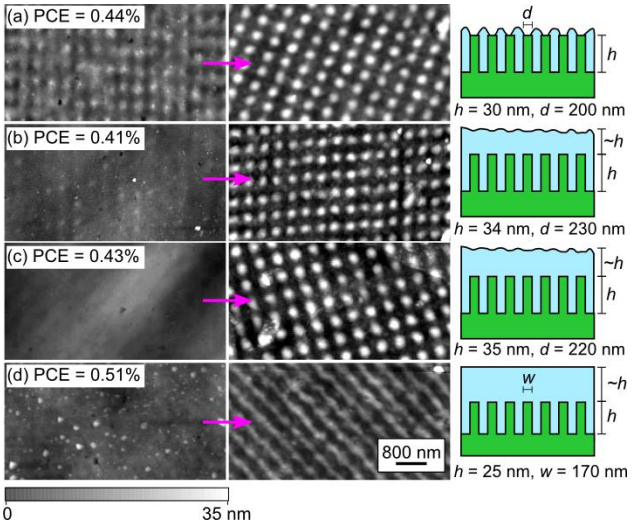

Figure 2.7: Device deconstruction. Surface of the nanostructured P3HT/PCBM composite after removal of Al cathode (left), and after immersion in dichloromethane (right). The accompanying cartoons illustrate the active layer structure.

an error in the printing process generated "modulated" nanolines instead of dots, and the PCE for this design was 50% larger than gradient devices (see Table 2.1). Significantly, the P3HT nanostructures are still intact after thermal annealing, solvent-based processing, and electronic characterization steps. We note that polymer-based electronics have limited resistance to thermal or solution-based processing, and this challenge is usually addressed by synthesizing polymer semiconductors with crosslinkable side groups [77, 79–82]. In our approach, polymer cross-linking is inherent to the lithographic process. Cross-link density is controlled by exposure dose, so properties such as thermal stability, mechanical stability, and solvent resistance are easy to optimize for a specific application.

2.4 Conclusions

We developed a simple, two-stage approach to control the morphology of polymer/fullerene solar cells based on direct-write lithography of polymer semiconductors. First, thin films of poly(3-hexylthiophene) (P3HT) are cross-linked into conductive nanostructures or microstructures with electron-beam lithography. Second, the polymer structures are coated with a soluble fullerene to complete the heterojunction. This methodology offers several features that are very valuable for fundamental structure-property investigations. First, the lithographic process is compatible with commercially-available materials. Second, the cross-linked polymer structures are stable through thermal annealing and solution-based processing. Third, different designs can be studied systematically because nanostructure size, shape, density, and placement are all controlled with computer software. Fourth, interfacial area and domain size can be varied independently of polymer crystallinity. Finally, after measuring the optoelectronic characteristics of these model devices, the active layer can be deconstructed to measure the morphology. We verified that patterned P3HT films can absorb light, generate charges, and conduct charges. We included simple structure-property studies that show improvements in power-conversion efficiency with increasing P3HT/fullerene interfacial area. Further studies are needed to fully evaluate the effects of irradiation and development on molecular structure, crystallinity, and charge-carrier mobility.

Electron-beam lithography is too slow for large-scale production of polymer-based optoelectronic devices. However, like electrochemical nanopatterning and other scanning-probe techniques [83–86], direct-write lithography could be very valuable for

basic scientific investigations. For example, when nanoscale polymer devices are generated *in-situ* with lithography, their positions are precisely controlled for integration into circuity. This attribute is very useful for testing the function of nanoscale optical and electrical sensors [82, 87, 88]. The cross-linking reaction is advantageous for devices that require sequential casting of different layers, such as multi-color light-emitting diodes [79] or tandem solar cells [80]. Other lithographic tools based on ionizing radiation may be appropriate for manufacturing. For example, atom-beam effect the same cross-linking reaction as electrons - but at much lower doses. Proximity ion beam lithography systems can provide high-throughput (square meters per hour) [89–92], offering a route to low-cost nanopatterning of polymer semiconductors for a variety of applications.

Chapter 3 Effects of radiation on polymer crystal orientation and charge transport.

3.1 Introduction

Thin films of π-conjugated polymers are widely investigated for their applications in organic electronics like polymer-based solar cells, light emitting diodes and transistors [93–96]. Device modules fabricated using polymer thin films are lightweight, durable and flexible. Manufacturing costs for casting thin films is reduced because of roll-to-roll and wet processing techniques [1–3]. Thus, π-conjugated polymers are attractive for organic electronics. Optical and electrical properties in these π-conjugated polymers is depended on their morphology. These polymer systems have disordered structure and fundamental understanding is required to enhance the polymer properties [96–101].

Direct patterning with lithography can print conductive microstructures and nanostructures using electron-beam or atom-beam [54, 62, 102]. π-conjugated polymers on exposure to radiation generate free radicals which can form intermolecular cross-links in the system. Solvents can be used to selectively remove un-exposed polymer and retain cross-linked domains. This technique can have precise control of size, shape, density and placement of domains in the system. This simple approach to control morphology is valuable for systematic structure-property studies and for further potential device optimization.

In this work, the effects of radiation on polymer structure and properties are studied. Proximity ion beam lithography (PIBL) was used to directly pattern thin films of π-conjugated polymers. Atom-beam can initiate a localized, *in-situ* cross-linking reaction in the polymer matrix. Cross-linked polymer of nanostructures or microstructures can be generated depending of the exposed area. Unexposed polymer can be removed by developing the image in organic solvent. For our studies, we used exposed polymer and cross-link density was varied by varying the exposure dose. Cross-linked polymers were studied for polymer structure and charge-carrier mobility. Spectroscopic, X-ray scattering and mobility measurements were done on these systems. PIBL can be used for flood exposure with a high-throughput [89–92], such technology is valuable in different areas where controlled structure is required.

The material used in this work is poly(3-hexylthiophene) (P3HT), which is widely investigated as the donor material in polymer-based solar cells [5, 8], and the active material in organic thin film transistors. The studies are divided into four areas. First, P3HT sensitivity to atom-beam was investigated. P3HT is a negative-tone resist, which was consistent with our previous studies with electron-beam lithography. Second, cross-linked P3HT films were measured with ultraviolet-visible (UV-Vis) spectroscopy. The data clearly indicates that cross-linked P3HT films retain light absorption properties. Third, mobility measurements were done to evaluate charge-carrier mobility in cross-linked polymer (see Figure 3.1). The device consists of layers of indium tin oxide (ITO), poly(3,4-ethylenedioxythiophene):poly(styrenesulfonate) (PEDOT:PSS) and poly(3-hexylthiophene)(P3HT). The charge-carrier mobility measured from space charge limited current (SCLC) region drops by 50% in cross-linked polymer system. Fourth, polymer crystallinity was studied by grazing-incidence wide angle X-ray scattering measurements. Degree of crystallinity also reduces by 50% in

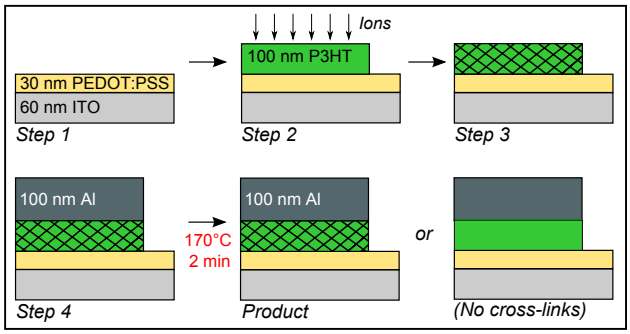

Figure 3.1: Direct patterning of polymer and device fabrication for mobility measurements.

cross-linked polymers. These studies enable complete understanding of the effects of radiation on polymer system to be used as a model system for structure–property studies in organic devices.

3.2 Experimental Methods

Materials. Poly(3,4-ethylenedioxythiophene):poly(styrenesulfonate)(PEDOT:PSS) was purchased from Baytron (product PH500, 1 wt% aqueous dispersion). The PEDOT:PSS dispersion was diluted with two parts deionized water and then filtered with a 0.45 μm glass microfiber mesh. Substrates for devices are glass microscope slides coated with 60-100 nm of indium tin oxide (ITO, 15-25 Ω/Sq, Sigma Aldrich). Poly(3-hexylthiophene) (P3HT) was purchased from Rieke Metals (90-94% regio-regular, number-average molecular weight of 30 kg/mol, polydispersity index of 1.8). P3HT was dissolved in anhydrous chlorobenzene at a concentration of 0.019 g/mL and filtered three times with a 0.2 μm Teflon mesh. Concentrated solution of poly (methyl methacyralate) (PMMA) in anisole was purchased from MICRO CHEM. The solution was diluted with seven parts of anisole to form thin films of PMMA. PMMA is used to calibrate PIBL doses.

Proximity Ion Beam Lithography. Large P3HT pads (1 cm diameter) are patterned with a 10 keV, 0.3 mA atom-beam using a proximity ion beam lithography (PIBL). Doses were varied in the range of 0.3 to 2.5 μC/cm^2. These patterns are used for two tasks: (i) Lithographic contrast is evaluated by measuring the residual thickness of isolated pads; and (ii) Crystallinity, absorption, and charge-carrier mobility are measured from the exposed pads. Poly (methyl methacrylate) (PMMA) films of thickness 350±5 nm were spun-cast on silicon substrates. PMMA contrast curves were generated to calibrate the exposure doses in each run of the PIBL instrument. Dose series of 0.3 to 2.5 μC/cm^2 with increments of approximately 0.2, total of 8 exposure doses were used. PMMA contrast curve from each run where super-posed and the doses were corrected for any deviation.

Microscopy. Patterned P3HT films are measured with Atomic Force Microscopy (AFM) using a MultiMode 3 (Veeco) in Tapping Mode for film thickness. AFM probes are silicon with a spring constant of 40 N/m. The structures of patterned features are evaluated with a Nikon Eclipse LV100 optical microscope (bright-field optics).

Spectroscopy. Samples are prepared by spin-casting on cleaned glass slides. P3HT film thickness is approximately 95±5 nm. P3HT films were pre-baked at 150°C for 2 min after spin-casting. Films were then exposed to atom-beam with the dose series of 0.3 to 2.5 μC/cm^2 and measured for light absorbance using ultraviolet-visible (UV-Vis)spectroscopy. The exposed P3HT films where compared with as-cast films for light absorption properties. All data are collected in transmission mode at normal incidence (approximately). The signal from a clean glass slide was also measured and subtracted from the spectra. UV-Vis absorbance is recorded with a JASCO V-570 UV/VIS/NIR spectrophotometer (200-800 nm). Film thicknesses of P3HT on glass

slides was measured using AFM. Linear absorption coefficients (μ) is estimated from the UV-Vis absorbance (A) data using Beer-Lambert Law,

$$\mu = A/t, \tag{3.1}$$

where film thickness (t) of P3HT films (measured using AFM). μ values at maximum peak absorption (approximately 512 nm) and at vibronic shoulder (600 nm).

Patterned devices. Substrates are cleaned by sonication for 20 minutes in each of the following solutions: 2% Hellmanex II detergent, deionized water, and iso-propanol. Substrates are then immediately dried in a clean nitrogen stream and are transferred to a nitrogen-purged glove box. PEDOT:PSS films with thickness (30 ± 5) nm are spun-cast on top of the ITO anode, then baked for 10 minutes at 140°C. ITO/PEDOT:PSS stack is coated with a (100 ± 5) nm P3HT film. P3HT film is pre-baked at 150°C for 2 min (to remove residual solvent). The active layer is built following the scheme in Figure 3.1. First, samples are transferred to the proximity ion beam lithography instrument for cross-linking. Second, samples are transferred to a thermal evaporator for deposition of a 100 nm thick Aluminum (Al) cathode. Last, samples are returned to the glove box to thermally-anneal the active layer at 170 °C for up to 2 minutes. Note that samples are transferred between instruments using a portable chamber that is pressurized with nitrogen.

Electronic Characterization. All electronic measurements are conducted in a nitrogen-purged glove box at 28°C under dark conditions. Current-voltage (I–V) characteristics are recorded with a Keithley 2601A source meter. To convert from current (I) to current-density (J), the device active area is calculated from the cathode

area (measured from analysis of optical micrographs). Typical active areas are 0.09-0.14 cm^2. Hole mobility measurements are done by fitting the dark J–V curves in the space charge limited current (SCLC) region using the modified Mott-Gurney equation,i.e. [103],

$$J = ((9/8)\epsilon\epsilon_{\circ}\mu_h(V^2/L^3)\exp(0.89\beta(V/L)^{0.5})), \tag{3.2}$$

where μ_h is the hole mobility, β is the field-activation factor , ϵ is the relative permittivity ($\epsilon \approx 3$ for P3HT) and $\epsilon_{\circ}$ is the permittivity of free space. Mobility measurements were reported for devices with SCLC slope $\leq$2.

Grazing-Incidence Wide Angle X-Ray Scattering (GIWAXS). GIWAXS experiments were conducted at beam line 8-ID-E at the Advanced Photon Source of Argonne National Laboratory. Samples were placed in a vacuum chamber and illuminated with 7.35 keV radiation at incident angles in the range of $0.1 - 0.24°$; the off-specular scattering was recorded with a Pilatus 1MF pixel array detector (pixel size = 172 μm) positioned 204 mm from the sample. Acquisition times were approximately 10 sec per frame. Each data set is stored as a 981×1043 32-bit tiff image (Pilatus, with 20-bit dynamic range). In order to fill the gaps that appear in the image due to the detector, two images with a vertical offset were collected. These images were used to get gapfilled images. Gapfilled images are corrected for flat-field, solid angle (efficiency and polarization) and displayed as intensity maps in q-space with the GIXSGUI package for MATLAB. Data is then processed for quantitative analysis as described in the Results and Discussion.

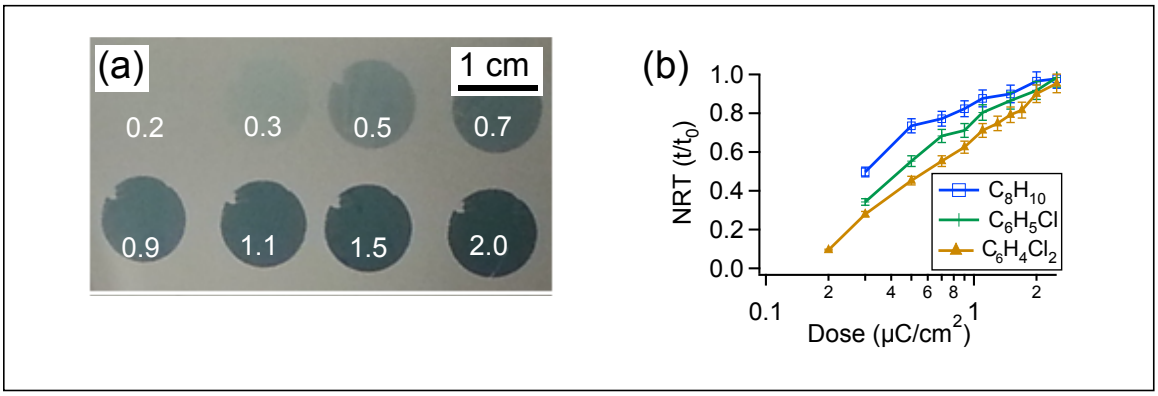

Figure 3.2: (a) Optical micrograph of cross-linked P3HT pads on a silicon substrate. Irradiation doses are marked below each pad in units of μC/cm^2. (b) Normalized residual thickness (t/t_0) as a function of exposure dose for each developer.

3.3 Results and Discussion

The objective of these studies were to understand the effects of radiation on polymer structure and charge-carrier mobility. P3HT films of thickness 95±5 nm were spun-cast on clean silicon substrates for lithographic studies. Sensitivity to atom-beam radiation was studied by constructing contrast curves of P3HT. Thin films of P3HT were patterned with PIBL and the relief images were developed with dichlorobenzene (room temperature) or chlorobenzene or *p*-xylene (35°C). Note that *p*-xylene is purged with nitrogen to displace dissolved oxygen. Figure 3.2(a) includes examples of large P3HT patterns, and Figure 3.2(b) reports the normalized residual thickness as a function of exposure dose for *p*-xylene (square), chlorobenzene (verticle line) and dichlorobenzene (triangle) developers. We find that, P3HT is a negative-tone resist and an exposure dose of 1 μC/cm^2 can retain 80% of the film after development. On exposure to electron-beam or atom-beam, free radicals are generated which can form intermolecular cross-links in the polymer system. Cross-link density in the polymer system can be varied by changing the exposure dose. In this work, patterned

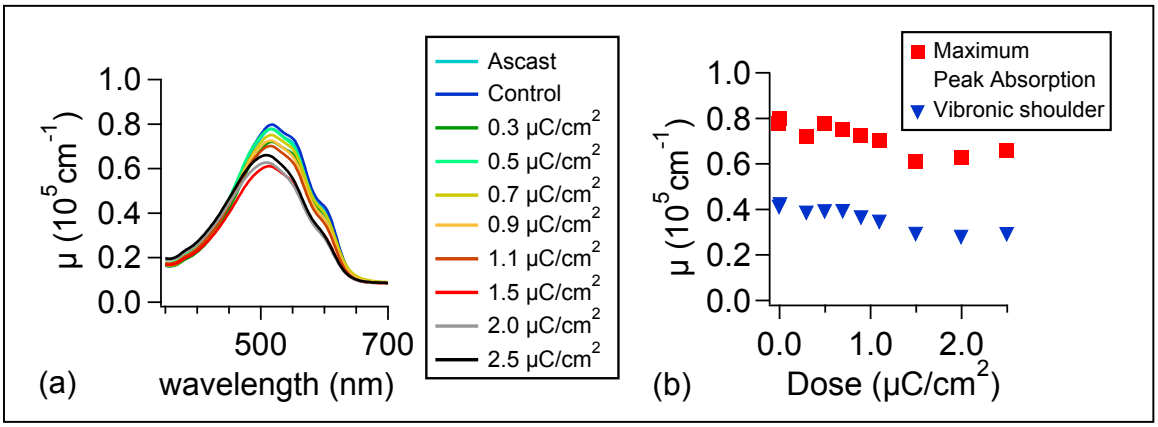

Figure 3.3: (a) Linear absorption coefficient (μ) measured by UV-Vis spectroscopy and (b) Maximum value of linear absorption coefficient (μ) and also at vibronic shoulder (600 nm) are plotted.

P3HT with no development is investigated for its polymer structure and charge-carrier mobility. These studies will be helpful in understanding the effects of radiation on polymer system.

Spectroscopy. Cross-linked P3HT films were investigated for π-bonds that are responsible for optoelectronic function. UV-Vis spectroscopy is used to evaluate light absorption properties. Thin films of P3HT were prepared on cleaned glass slides and were pre-baked for 2 minutes at 150°C to remove the residual solvent. These samples were pattered using PIBL for a dose range of 0.3 to 2.5 μC/cm^2 and compared with as-cast P3HT film. PIBL is implemented under ultra high vacuum (10^{-7} Torr) and this technique allows flood exposure of samples with high-throughput. The sample labeled as "control", follows the same procedure as irradiated sample with exposure time of 0 seconds. Figure 3.3(a) shows the UV-Vis data for all samples studied. The light absorption properties are retained in P3HT films after atom-beam exposure at low-to-moderate doses. This can be clearly seen from Figure 3.3(b), where maximum values for linear absorption coefficient (μ) was plotted as a function of exposure dose. Light

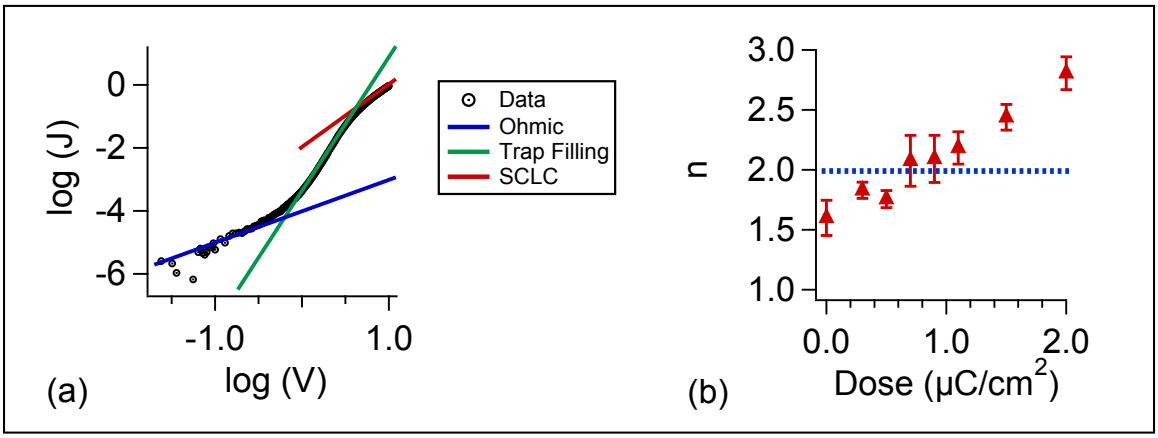

Figure 3.4: (a) $\log(J)$–$\log(V)$ characteristics of as-cast P3HT device. The curves were measured under dark conditions. (b) n in the SCLC region was plotted for all devices studied. Error bars correspond to measurements from 3-4 devices for each exposure dose.

absorption properties are retained in thin films of cross-linked polymers. However, at high exposure dose (> 1 μC/cm^2) the absorption properties drop gradually. (μ) at the vibronic shoulder (600 nm) in P3HT films was plotted as a function of exposure dose as shown in Figure 3.3(b). The fine structure of P3HT is retained at low-to-moderate exposure doses, but might be disrupted at high exposure doses. These results are consistent with work from other groups working with cross-links generated using peroxide radical initiator [58]. The loss of fine structure suggests that high exposure doses partly disrupts the intermolecular ordering.

Mobility measurements. Mobility measurements were done on patterned P3HT devices. We built devices following the scheme in Figure 3.1. Patterns devices with exposure dose from 0.3 to 2.5 μC/cm^2, and total devices of 8 doses were fabricated. We also prepared two types of devices that were not exposed to atom-beam radiation which are labeled as as-cast and control devices. The "as-cast" device will act as reference device in our experiments. "Control" device follows the same procedure as

exposed devices, but time of exposure is 0 seconds. Control devices were similar to as-cast devices. Dark current (I)- voltage (V) measurements were done on all these devices. With active area measurements using optical microscopy, current (I) was converted to current-density (J). A simple scaling relationship of J on V, which corresponds to $\mathrm{J} \propto \mathrm{V}^n$ can describe the dark measurements. n corresponds to the slope of a $\log(J)$ verses $\log(V)$ plot [104,105]. Figure 3.4(a) shows the $\log(J)$ - $\log(V)$ plot of as-cast P3HT films and three regions can be identified based on the slope (n). When the slope (n) = 1, the number of injected carriers is less than the intrinsic charge carriers. The system then follows ohmic behavior under low bias. J-V characteristics with $n > 2$ corresponds to trap filling region. Semiconducting polymers like P3HT are known for trap-limited hole mobility. For exponential distribution of trap energy states, n corresponds to the characteristic width of these energy states [104, 105]. When all trap states are filled, $n \leq 2$ corresponds to trap-free space charge limited current (SCLC) region. Figure 3.4(b) shows the summary of n in the SCLC region for all devices after annealing for 2 minutes at 170°C. The slope n in the SCLC region for low-to-moderate doses is $\leq$2, which partly corresponds to filled trapped states. With an increase in exposure dose the slope increases significantly, which suggests that trap states are introduced.

Charge transport properties in patterned devices was studied by evaluating hole mobility (μ_h). μ_h was estimated by fitting the SCLC region ($n \leq 2$) of the characteristic J-V data with modified Mott-Gurney equation (mentioned in the experimental procedures). Figure 3.5 plots μ_h as a function of exposure dose. μ_h of unexposed devices is of the order 2×10^{-4} (cm^2/V.s), which is consistent with results from other groups [106,107]. μ_h in patterned devices drops by almost 50% when compared to unexposed devices. At high exposure dose, trap states are introduced which can

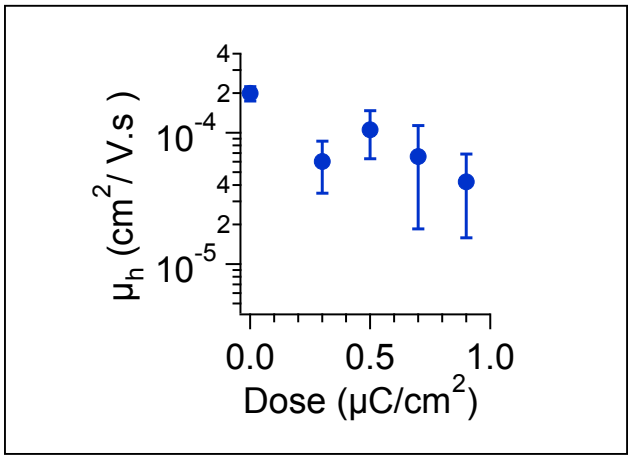

Figure 3.5: Hole mobility (μ_b) of all devices as a function of exposure dose. μ_b of unexposed devices are denoted at an exposure dose 0 μC/cm^2. Error bars correspond to measurements from 3-4 devices for each exposure dose.

reduce the charge-carrier mobility. In order to understand the significant difference in μ_h between unexposed and exposed devices, polymer structure has to be investigated. We used grazing-incidence wide angle X-ray scattering (GIWAXS) technique to understand the molecular ordering in cross-linked polymer system.

Polymer structure. P3HT chemical structure has both aliphatic and aromatics chains, the dissimilarity between the two chains drives the formation of small regions of crystals. π-π stacking of aromatic groups form crystals denoted as "face-on" crystal orientation. This orientation is most preferred for solar cells in order to transport free charges to respective electrodes. P3HT film can also have "edge-on" orientation where the aliphatic chains are stacked together [108, 109]. In order to investigate radiation effects on molecular ordering and crystallinity, grazing-incidence wide angle X-ray scattering (GIWAXS) technique was used. Thin films of pre-baked P3HT films were spun-cast on silicon substrates and exposed to atom-beam for a series of doses. The sample preparation was done in nitrogen purged glove box and are transported in portable nitrogen chamber. As-cast P3HT films were used as reference.

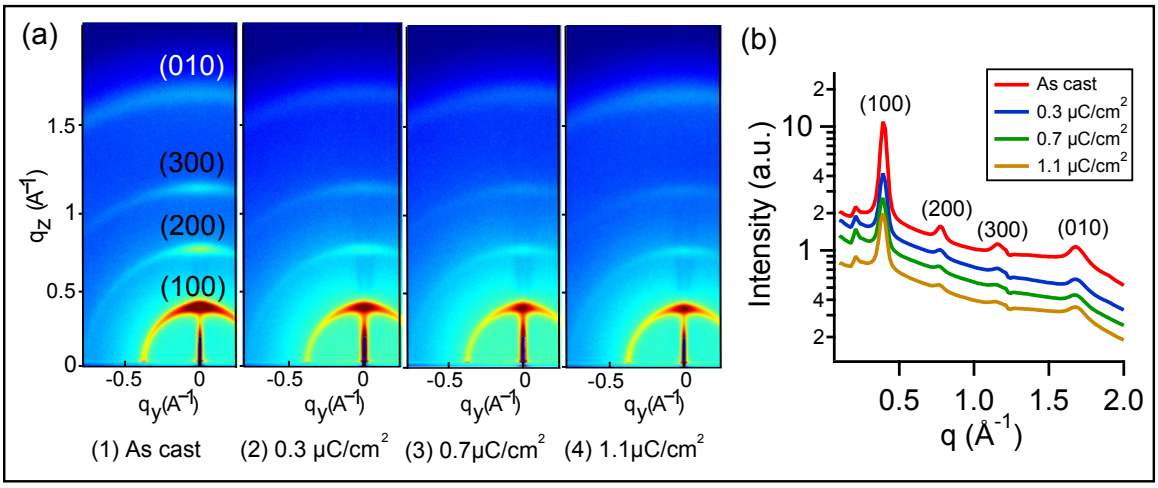

Figure 3.6: (a) Corrected grazing-incidence X-ray scattering data for as-cast and exposed P3HT films. (b) Azimuthal integrated intensity (I) verses scattering vector (q) for as-cast and exposed P3HT films.

GIWAXS data was collected for all samples and gapfilled images were corrected (mentioned in the experimental procedures). Figure 3.6(a) shows the corrected GIWAXS images for pre-baked P3HT films of as-cast, exposed samples at 0.3 μC/cm^2, 0.7 μC/cm^2 and 0.9 μC/cm^2. "Face-on" crystal orientation corresponds to a peak (010) and "edge-on" crystal orientation to peaks (100), (200), and (300) [108, 109] which are denoted on GIWAXS images. Figure 3.6(b) shows the azimuthal integrated intensity (I) as a function of scattering vector (q), which was extracted from GIWAXS images and is showed for as-cast, exposed samples at 0.3 μC/cm^2, 0.7 μC/cm^2 and 0.9 μC/cm^2. Broad peaks correspond to disordered orientation of crystals in both as-cast and exposed P3HT films.

In order to evaluate crystallite size in P3HT films, peak intensities at (100), (200), (300) and (010) peak positions were fit using lorentzian function. Figure 3.7(a) shows full width half maximum (FWHM) evaluated from the fits for all peaks. FWHM for as-cast films is lower when compared to exposed films. Crystallite size is inversely related to the FWHM. Figure 3.7(b) shows crystallite size in exposed films relative

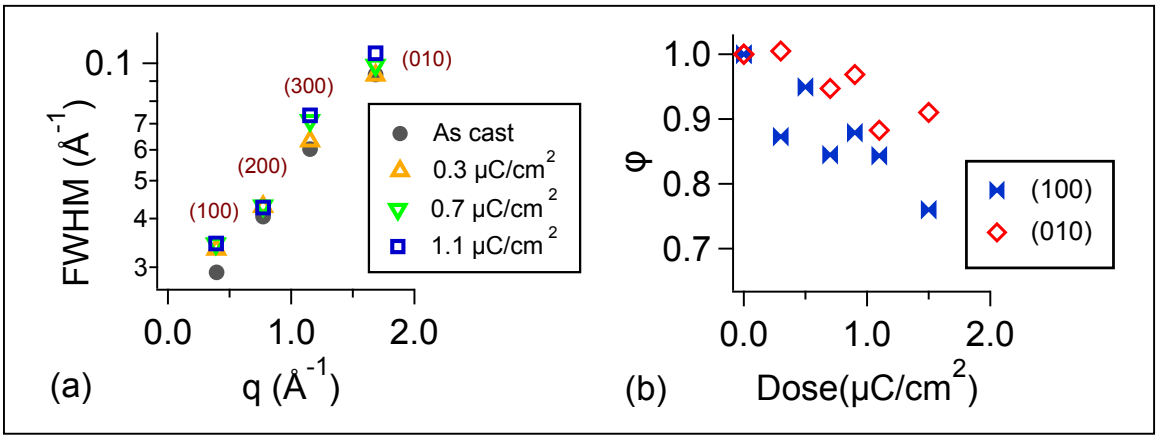

Figure 3.7: (a) FWHM evaluated from peak intensities at (100), (200), (300) and (010) peak positions in as-cast and exposed P3HT thin films. (b) Relative crystallite size (ϕ) for (100) and (010) in exposed P3HT films relative to as-cast.

to as-cast P3HT film. As the exposure dose increases, the relative crystallite (ϕ) size along (100) and (010) direction reduces.

Orientation distribution of crystallites can be obtained by constructing pole figures. These pole figures were constructed for (100) peak using the procedure described by other groups [110, 111]. Wedge cuts of angular breadth 2° were taken for various detector angles from GIWAXS image. Peak intensities at (100) peak position was fit with a lorentzian function (accounting for background). Intensities for pole figure were corrected for angular resolution limit and plotted against various orientation angle (χ). Figure 3.8 (a) shows the data and fit for (100) peak intensities of pole figure in as-cast and exposed P3HT films. The data and fit were given an offset to observe the peaks in both as-cast and exposed films. Integrated peak intensity (I_{intg}) for (100) peak was evaluated from the fits to the pole figure intensities. I_{intg} for all irradiated P3HT films was compared to integrated peak intensity of as-cast film (I_{intg_0}). Figure 3.8(b) shows the integrated peak intensities relative to as-cast P3HT films. Degree of crystallization (DOC) is directly related to integrated peak intensity.

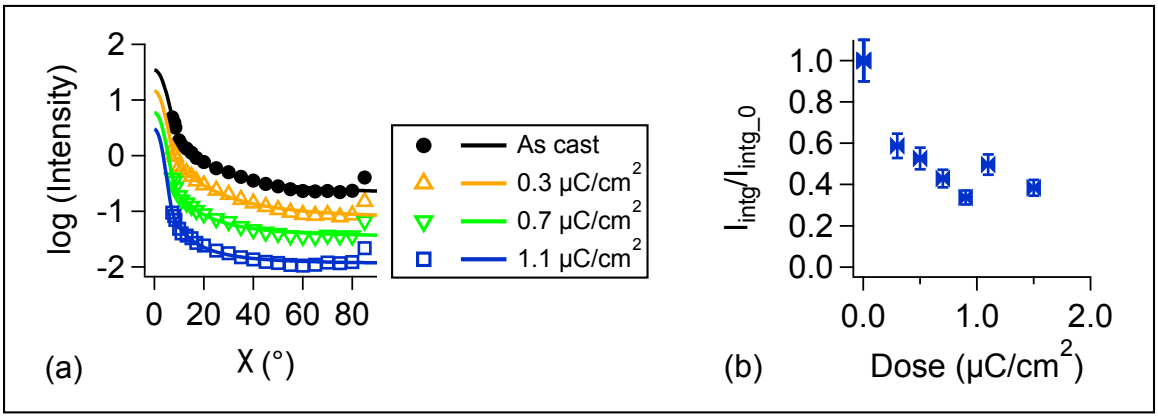

Figure 3.8: (a) Pole figures for (100) peak where logarithm of peak intensity was plotted as a function of orientation angle (χ). Fits for the data are shown as a solid line. (b) Integrated peak intensity of exposed films relative to as-cast P3HT film was plotted for all doses.

DOC decreases for about 50% when polymer is exposed to radiation.

When the polymer is exposed to radiation, at low-to-moderate doses the crystallite size and degree of crystallization drop significantly when compare to as-cast films. Intermolecular cross-links generated in π-conjugated polymers can disrupt the crystallite formation and thus reduced crystal orientations. This may be couple to reduced charge-carrier mobility in exposed P3HT films.

3.4 Conclusions

We have studied the effects of radiation on polymer structure and charge-carrier mobility. On exposure to radiation, intermolecular cross-links can be generated in π-conjugated polymer. Charge-carrier mobility was measured and it drops by 50% for exposed P3HT films at low-to-moderate doses. On higher exposure doses, trap states are introduced in the system which can significantly reduce carrier mobility. Crystallite size and degree of crystallization was reduced by 50% in cross-linked P3HT

films. Further studies are required to understand the cross-linking mechanism in these polymer system. X-ray photoelectron measurements are underway to identify the types of bonds present in irradiated films.

Chapter 4 Controlling Domain Orientations in Thin Films of AB and ABA Block Copolymers

4.1 Introduction

Thin films of block copolymers are attractive as low-cost templates for nanopatterning [21–23]. Applications in semiconductor manufacturing will require control over the size and shape, position, and orientation of copolymer domains [21, 23]. Domain sizes and shapes are determined by copolymer molecular weight and composition [24], respectively, while positions can be controlled with epitaxial or topographical templates [112–115]. Domain orientations are largely determined by surface energetics and confinement effects, and these factors are most thoroughly studied for diblock (AB) copolymers [20,23]. The objective of our current work is to identify the factors that control domain orientations in thin films of triblock (ABA) copolymers.

For most applications in nanopattering, a thin copolymer film is prepared by spin-casting on a substrate, so domains are confined between a hard surface and a "soft" air interface. Typically, each interface favors wetting by one of the blocks, and this preference drives a layering of the domains parallel to the substrate [20, 116]. For example, consider a thin film of lamellar poly(styrene-*b*-methyl methacrylate) (PS-PMMA) on a silicon substrate: PS has a slightly lower surface energy than PMMA, while PMMA is strongly preferred over PS at the substrate [117,118]. These asymmetric boundary conditions favor a parallel domain orientation that persists through the film thickness [119,119,120]. In these asymmetric systems, film thickness

is commensurate with the equilibrium domain size when $t = (n + 1/2)L_0$, where L_0 is the domain periodicity and n is an integer. When film thickness is incommensurate with L_0, entropic frustration drives the formation of islands or holes at the free surface [118,120]. The film then consists of regions with two distinct thicknesses that are both commensurate with L_0 [116].

Domains that are oriented parallel to the substrate are not useful for nanopatterning, so a variety of methods have been developed to produce the desired perpendicular orientation [121]. Examples include application of an electric field [122], rough substrates [123, 124], directional solvent evaporation [125, 126], adding surfactants or surface-active nanoparticles [121, 127], blending with homopolymer [128], and preparing "neutral" substrates by tuning the polymer-substrate interfacial energy [26, 129, 130]. The latter approach is very popular because the technique can be applied to many copolymer systems and is easy to integrate with standard manufacturing protocols [23]. However, perpendicular domains are only stable on neutral substrates through a limited range of film thickness [25, 131–135]. The film thickness constraint is understood by considering the interfacial energetics that control domain orientations: Perpendicular orientations incur a gain in surface energy. If the copolymer is comprised of segments with similar surface energies, such as PS and PMMA, then this additional enthalpic contribution can be offset by other factors. For example, when film thickness is incommensurate with L_0, either kinetic or thermodynamic barriers may prevent the formation of surface relief structures, favoring perpendicular orientations to relieve entropic frustration [28, 29, 116, 135, 136].

Recently, it was demonstrated that copolymer architecture can dramatically affect the free energy landscape in thin films [30,31]. Specifically, in thin films of ABA triblock copolymers, perpendicular domain orientations are stable at the air interface

when the B midblock has a slightly lower surface energy than the A endblocks [30]. The effects of architecture on domain orientation were originally discussed by de Jeu et al. [137], where it was proposed that a B-rich wetting layer would form at the air interface if the entropic penalty for "looping" was less than the surface energy gain for perpendicular domains. This description is consistent with experimental observations and self-consistent field theory (SCFT) calculations [30]. Matsen recently clarified the effects of copolymer architecture on surface energetics by noting that chain ends have a broader distribution at the free surface, so the stability of perpendicular domains largely results from increased end-segment configurational entropy [31].

In our present work, we compare domain orientations in thin films of lamellar PS-*b*-PMMA and PMMA-*b*-PS-*b*-PMMA diblock and triblock copolymers, respectively. The melt surface energy of PS homopolymer is slightly lower than that of PMMA [117,118], but we expect that end-segment entropy will mitigate the enthalpic preference for PS at the free surface and drive a perpendicular domain orientation. All diblock and triblock films are prepared on neutral (or near-neutral) substrates, so energetics at the air interface will largely control domain orientations through the film thickness. Film structure is characterized through optical microscopy, atomic force microscopy, and grazing-incidence small-angle X-ray scattering. For diblock copolymers, we find that domain orientations are highly sensitive to substrate surface chemistry, consistent with numerous other reports [25,131,132,134,135]. Perpendicular domains are reliably obtained on neutral substrates when film thickness is highly incommensurate with asymmetric boundary conditions and/or annealing temperature is elevated ($\geq$ 220°C). For triblock copolymers, we find perpendicular domain orientations in all film thicknesses considered. In addition to the expanded thickness window, we find that domain orientations in triblock films are insensitive to processing

conditions (temperature, time, and variations in substrate surface chemistry), offering greater processing flexibility when compared with the diblock architecture. However, tilted domains are detected in the interior of all diblock and triblock copolymer films. The scattering data suggest that tilt defects are kinetically trapped, and their density could be minimized by reducing the copolymer molecular weight.

4.2 Experimental Methods

Materials. All polymers were purchased from Polymer Source and used as received. "Neutral" polymer brushes are prepared from a hydroxyl-terminated poly(styrene-*co*-methyl methacrylate) random copolymer that is 59 mol% styrene with M_n = 8.9 kg/mol and PDI = 1.47. (The styrene content is slightly higher than the reported "optimal" composition for lamellar copolymers, but we find that substrates treated with this copolymer are slightly selective towards methyl methacrylate.) The AB diblock copolymer is poly(styrene-*b*-methyl methacrylate) (PS-PMMA), with M_n = 100 kg/mol, PDI=1.12, and 50 mol% styrene. The ABA triblock is poly(methyl methacrylate-*b*-styrene-methyl methacrylate) (PMMA-PS-PMMA), with M_n = 198 kg/mol, PDI=1.15, and 50 mol% styrene. Equilibrium lamellar periodicity (L_0) for AB and ABA copolymers are 46 nm and 50 nm, respectively, as determined with X-ray scattering. Substrates are (100) oriented silicon wafers with minimal bow (per the manufacturer). Substrates are cleaned with Piranha solution (3:1 H_2SO_4:30% H_2O_2, ***Caution! Highly Corrosive***) to destroy organic contamination and grow a thin oxide layer.

"Neutral" Substrates. Random copolymer is dissolved in toluene at a concentration of 1 wt%, and films that are approximately 30 nm thick are prepared by

spin-casting on ultraclean silicon substrates. Polymer chains are grafted to the substrate by annealing under low vacuum (10 mTorr) with the following temperature profile: 80°C for 2 hours, then 160°C for one day, followed by cooling to room temperature. Un-grafted polymer is extracted by agitating the samples in toluene (using a sonication bath) or soaking in a stationary toluene bath for one hour. Samples are then dried with nitrogen. The quality (density) of the brush is assessed by measuring the contact angle of water, which is usually 72° after this process. Contact angle is increased to $80-83°$ by repeating all steps a second time (includes coating a new film, annealing, and rinsing); these measured contact angles match the reported values in the literature [131]. Throughout this manuscript, the different brush qualities are denoted by the contact angle of water at the surface.

AB and ABA Thin Films. Thin films of AB and ABA block copolymers are prepared on the "neutral" brushes. Polymers are dissolved in toluene at concentrations that range from 1-4 wt%; solutions are filtered with a 0.2 μm Teflon mesh. Films that range in thickness from 40 nm to 200 nm are prepared by spin-casting. Film thicknesses are measured with a JA Wollam M-2000 spectroscopic ellipsometer: Δ and Ψ are modeled with the Cauchy dispersion relation $n(\lambda) = A + B/\lambda^2$, where A, B, and film thickness are adjustable parameters for regression analysis (all positive values). Films are annealed according to two different procedures: Samples prepared via a "non-equilibrium" process are annealed in air for 10 minutes at 220°C or 240°C. Samples prepared by an "equilibrium" process are annealed under low vacuum (10 mTorr) for 1-2 days at either 180°C or 200°C. The segregation strength is approximately $\chi N \simeq 45$ at temperatures in the range of 180°C to 240°C [138].

Microscopy. The nanoscale and microscale structure of film surfaces are characterized with atomic force microscopy (AFM) and bright-field optical microscopy, respectively. AFM micrographs were collected with a MultiMode 3 (Veeco) in Tapping Mode using silicon probes with a spring constant of approximately 40 N/m. Typical parameters for data acquisition are 1.7 Hz scan frequency, 5 μm $\times$ 5 μm scan area, and 512 $\times$ 512 image resolution. Each sample is measured from at least five randomly-selected regions, and the fraction of perpendicular lamellae per micrograph is calculated with an algorithm implemented in IGOR Pro (Wavemetrics). Optical micrographs can detect variations in sample thickness over microscale areas that are associated with either parallel or mixed parallel/perpendicular lamellar orientations.

Grazing-Incidence Small Angle X-Ray Scattering (GISAXS). GISAXS experiments were conducted at beam line 8-ID-E at the Advanced Photon Source of Argonne National Laboratory. Samples were placed in a vacuum chamber and illuminated with 7.35 keV radiation at incident angles in the range of $0.1 - 0.24°$; the off-specular scattering was recorded with one of the following configurations: A MAR 165 ccd-based detector (pixel size = 79 μm) positioned 2019 mm from the sample, or a Pilatus 1MF pixel array detector (pixel size = 172 μm) positioned 2175 mm from the sample. Acquisition times were approximately 10 sec per frame. Each data set is stored as a 2048$\times$2048 16-bit tiff image (MAR) or as a 981$\times$1043 32-bit tiff image (Pilatus, with 20-bit dynamic range). Note that x-ray penetration depth varies from approximately 10 nm up to the full film thickness as incident angle is varied near the critical angle of the film (ca. 0.17°). All data are displayed as intensity maps $I(2\Theta, \alpha)$, where 2Θ and α denote in-plane and out-of-plane diffraction angles, respectively.

4.3 Results and Discussion

Variables. Thin films of AB (PS-*b*-PMMA) diblock and ABA (PMMA-*b*-PS-*b*-PMMA) triblock copolymers are prepared on "neutral" polymer brushes as described in the Experimental Procedures section. Film thickness, annealing temperature, annealing time, and brush quality are systematically varied to evaluate the effects of sample preparation on lamellar domain orientations. Brush quality is evaluated by measurements of the static water contact angle on freshly prepared substrates, where contact angles $> 80°$ are characteristic of a good-quality brush. Procedures for sample preparation is illustrated in Figure 4.1, and types of lamellar structures that are detected in experiments. (1) Thin film of random copolymer (RC) is cast on an ultraclean silicon substrate. Polymer is grafted to the substrate, and un-grafted polymer is removed to reveal the "neutral" polymer brush. (2) Thin film of PS-PMMA or PMMA-PS-PMMA copolymer (thickness t) is cast on top of the brush. (3) Heating above the glass transition promotes ordering of the lamellar domains. Possible outcomes are: (a) Parallel domain orientation, which is illustrated for asymmetric boundary conditions; (b) Perfect perpendicular orientation; (c) Mixed parallel and perpendicular orientations; (d) Perpendicular phase with "tilt" defects, i.e., misoriented domains.

Microscopy. The surfaces of AB and ABA films are characterized with bright-field optical microscopy (OM) and atomic force microscopy (AFM). OM detects surface relief structures that are associated with parallel domain orientations, such as islands and holes, while AFM directly resolves the domain orientations at the air interface. Representative micrographs for ABA and AB films are included in Figure 4.2 and Figure 4.3, respectively, where samples were annealed on good-quality neutral brushes

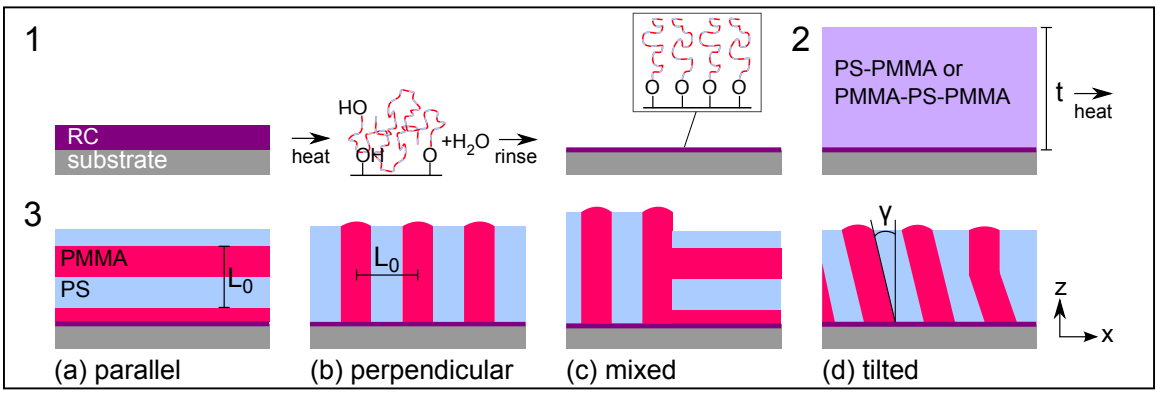

Figure 4.1: Overview of sample preparation and types of lamellar structures that are detected in experiments.

at 200°C for 2 days. Significantly, ABA triblock copolymer domains are perpendicular to the air interface for all thicknesses considered: Optical micrographs reveal flat surfaces, and AFM confirms the presence of perpendicular domains. However, the structures in AB diblock copolymer films are more complex. Domains are perpendicular to the air interface when thickness t is nearly commensurate with the equilibrium copolymer periodicity L_0, i.e., $t/L_0 \leq 1$. When diblock film thicknesses are increased, the optical micrographs reveal surface modulations with an approximate wavelength of 1 μm, and AFM measurements demonstrate that these modulations correspond with mixed parallel and perpendicular domain orientations at the air interface. Parallel domain orientations are dominant in the thickest films, although perpendicular domains are often detected in regions of the film that have a slightly different thickness (for example, the dark spots marked by the arrow in Figure 4.3). Such mixed orientations are common when PS-PMMA films are cast on nearly neutral substrates, indicating that energetics at the substrate and free surface are not perfectly balanced.

The micrographs in Figure 4.2 and Figure 4.3 illustrate the types of surface structures that are detected in these experiments, but these data correspond to a specific

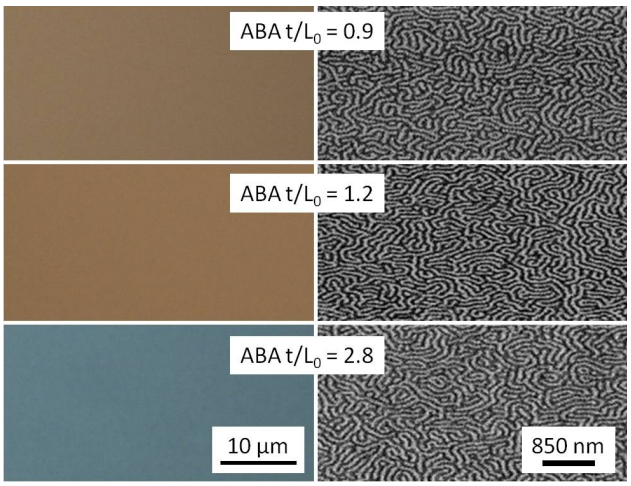

Figure 4.2: Bright-field optical micrographs and atomic force microscopy phase images of ABA film surfaces. All films were prepared on high-quality neutral brushes (contact angle of 83°) and annealed for 2 days at 200°C.

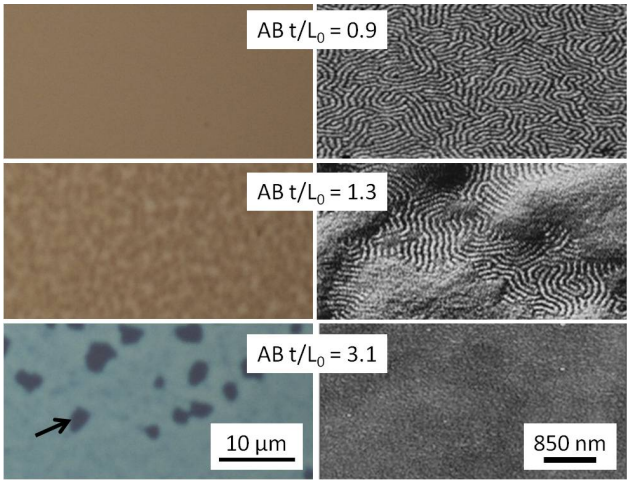

Figure 4.3: Bright-field optical micrographs and atomic force microscopy phase images of AB film surfaces. All films were prepared on high-quality neutral brushes (contact angle of 83°) and annealed for 2 days at 200°C.

processing scheme. Figure 4.4 and Figure 4.5 summarize the effects of each independent variable on domain orientations at the air interface for both long ("equilibrium") and short ("non-equilibrium") annealing processes, respectively. Legend explains the copolymer architecture, annealing temperature, and contact angle of water on the "neutral" polymer brush. The quality of "neutral" brushes is indicated by the contact angle of water, where the maximum value of 83° corresponds with the highest grafting density. The parameter f_{perp} denotes the area fraction of each surface that contains perpendicular domains, and these data are based on analysis of AFM images as described in the Experimental Procedures.

Figure 4.4 summarizes f_{perp} as a function of copolymer architecture, film thickness, quality of the neutral brush (contact angle), and annealing temperature. All samples were annealed for a minimum of 1 day under low vacuum. The prolonged annealing time was selected to bring these structures towards their equilibrium conformations, and no degradation was detected at these moderate annealing temperatures. We find that ABA domains are perpendicular to the air interface ($f_{perp} = 1$) for all processing conditions and film thicknesses considered, indicating that surface energetics are controlling the triblock domain orientations. However, the AB domain orientations vary with film thickness: Lamellae are parallel to the air interface when $t = (n + 1/2)L_0$, a signature of asymmetric wetting at the interfaces [20, 116]. Since the air interface is PS selective [117, 139], these data suggest that PMMA end-blocks are penetrating the neutral brush and interacting with the silicon substrate [140], i.e., the substrate is slightly selective towards PMMA. Diblock lamellae are perpendicular to the air interface when film thickness is $t \simeq nL_0$, or highly incommensurate with asymmetric boundary conditions. Incommensurability will typically drive the formation of islands or holes [20, 118, 141]. In this system, either kinetic or thermodynamic

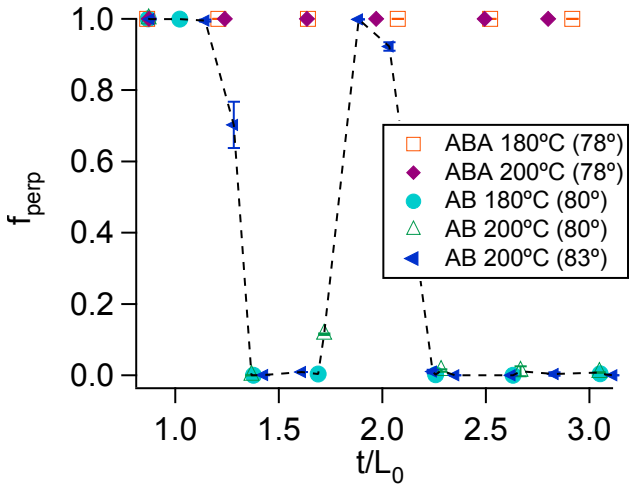

Figure 4.4: Fraction of perpendicular lamellae calculated from AFM images as a function of normalized film thickness. Data for "equilibrium" annealing (more than one day under low vacuum).

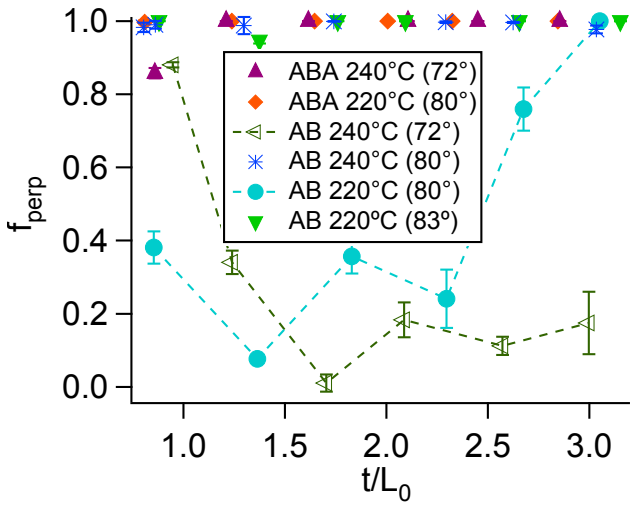

Figure 4.5: Fraction of perpendicular lamellae calculated from AFM images as a function of normalized film thickness. Data for "nonequilibrium" annealing (10 minutes in air).

barriers prevent the formation of surface relief structures, favoring perpendicular orientations to relieve entropic frustration [28, 29, 116, 135, 136].

Figure 4.5 summarizes f_{perp} as a function of copolymer architecture, film thickness, quality of the neutral brush, and annealing temperature. All samples were annealed for 10 minutes in air. The short annealing times are relevant to applications in manufacturing. Much like the "equilibrium" process, ABA domains are oriented perpendicular to the air interface for nearly all processing conditions considered. An exception is an ultrathin film ($t/L_0 \leq 1$) prepared on a poor-quality neutral brush, where mixed orientations are detected at the air interface. In this case, the substrate is slightly selective towards PMMA, so competition between the ordering preferred at each interface is likely responsible for the mixed orientations. AB domain orientations are more complex and depend on temperature, thickness, and brush quality. When brush quality is poor ($< 80°$), mixed parallel and perpendicular domain orientations are detected, where the former is dominant. However, perpendicular domain orientations are detected at the air interface when brush quality is improved ($\geq 80°$) and annealing temperatures are elevated ($\geq 220°$C). These data suggest that the surface energies of PS and PMMA are nearly equal at elevated temperatures, consistent with prior reports [134,140], and demonstrate the well-documented sensitivity to substrate surface chemistry [23].

Optical microscopy and AFM offer simple routes to characterize domain orientations at the air interface: Optical microscopy can quickly screen for thickness modulations that are characteristic of mixed domain orientations, while AFM measurements can discern the relative quantities of parallel and perpendicular domains at the free surface. However, it is important to note that surface microscopies cannot distinguish between perpendicular and "tilted" domain orientations (see illustration

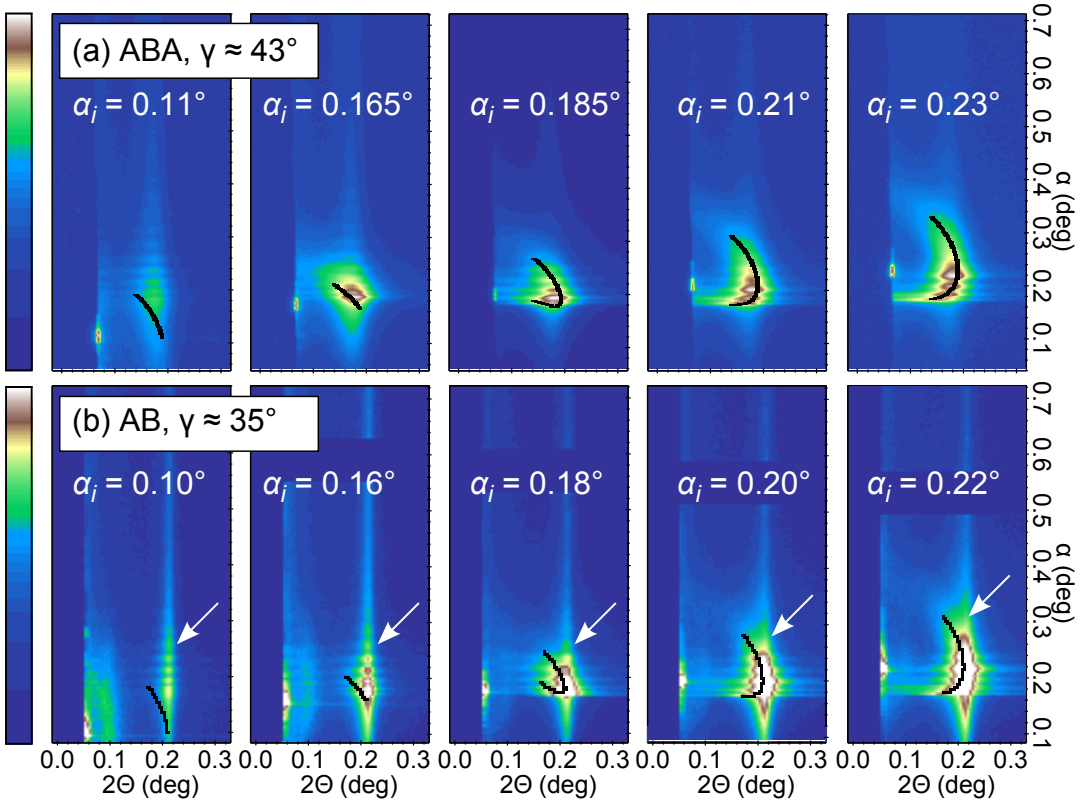

Figure 4.6: GISAXS data for (a) triblock and (b) diblock copolymer thin films ($t/L_0 = 2.9$) annealed at 240°C for 10 minutes.

in Figure 4.1). Furthermore, these microscopies cannot resolve the structures at the polymer-substrate interface. We therefore evaluate AB and ABA domain orientations through the film thickness with Grazing-Incidence Small-Angle X-Ray Scattering (GISAXS) [142–144]. In the subsequent section, we refer to a "perpendicular phase" that contains a distribution of domain orientations, and we quantify the range of tilt angles for misoriented domains through analysis of GISAXS patterns.

GISAXS Analysis. To evaluate the buried domain structure of AB and ABA thin films, GISAXS data were collected from four types of samples: AB films annealed for 2 days at 200°C, AB films annealed for 10 minutes at 240°C, ABA films annealed for

2 days at 200°C, and ABA films annealed for 10 minutes at 240°C. The brush quality was good for all samples (contact angle $> 80°$), so we expect that surface energetics will largely control the domain orientations through the film thickness. Details regarding beam line configuration and data storage are provided in the Experimental Procedures. It is important to note that incident angle (α_i) was varied near the critical angle of the film ($\alpha_c \approx 0.17°$) to control the X-ray penetration depth. It is difficult to accurately calculate a penetration depth from the incident angle, but the top ∼10 nm is sampled when $\alpha_i < \alpha_c$, while the full film thickness is sampled when $\alpha_i > \alpha_c$ [143]. All GISAXS results are consistent with the findings from microscopy: Perpendicular diblock domains were detected with GISAXS when $t \simeq nL_0$ and/or annealing temperatures were elevated, while perpendicular triblock domains were detected for all processing conditions considered. Diblock films that showed "mixed" parallel and perpendicular orientations are not discussed in this section.

When the full film thickness is sampled ($\alpha_i > \alpha_c$), nearly all diblock and triblock copolymer films show partial Debye-Scherrer (powder) rings [145]. Such features are consistent with a distribution of tilted domain orientations in the interior of these films. The range of tilt angles is denoted by $\pm\gamma$ as illustrated in Figure 4.1, where $\gamma = 0$ denotes a perfect perpendicular orientation. The parameter γ is determined for each data set by comparing simulated and experimental Debye-Scherrer rings in $(2\Theta, \alpha_f)$ space. Partial rings are simulated with a straightforward procedure: First, the scattering vector for lamellae tilted through an angle $\pm\gamma$ is defined as $\vec{q_r} = \vec{q} \cdot R$, where $\vec{q} = \{q_{xy}, q_z\} = \{2\pi/L_0, 0\}$ is the scattering vector for perpendicular lamellae and R is a two-dimensional rotation matrix. Second, the contours for partial Debye-Scherrer rings in $(2\Theta, \alpha_f)$ space are calculated from Equations 4.1-4.2 [142–144]:

$$\alpha_f = \arcsin\sqrt{\left(\frac{q_{z,r}}{k}\right)^2 + \sin^2\alpha_i \pm 2\frac{q_{z,r}}{k}\sqrt{n^2 - 1 + \sin^2\alpha_i}}, \tag{4.1}$$

and

$$2\Theta = \arccos\left(\frac{\cos^2\alpha_f + \cos^2\alpha_i - (q_{xy,r}/k)^2}{2\cos\alpha_f\cos\alpha_i}\right). \tag{4.2}$$

Note that parameters n and α_i are the refractive index of PS-PMMA and GISAXS incident angle, respectively, while $k = 2\pi/\lambda$. Tilt range $\pm\gamma$ was refined for each sample by comparing the predicted contour of partial Debye-Scherrer rings with experimental data for $\alpha_i > \alpha_c$; simulated contours are truncated where the intensity falls to 10% of the signal from perfectly perpendicular domains ($\gamma = 0$). This procedure is illustrated in Figure 4.6 for triblock and diblock films with thickness $t/L_0 \simeq 3$, where calculated contours are superimposed over experimental GISAXS data for a range of incident angles. Incident angle (α_i) is varied near the critical angle (0.17°) to produce controlled penetration depths. Contours for partial Debye-Scherrer rings are superimposed over experimental data (solid black lines). The ranges of lamellar tilt angles are $\gamma = (43 \pm 10)^\circ$ and $\gamma = (35 \pm 10)^\circ$ for triblock and diblock morphologies, respectively. Note that AB domains are not tilted near the air interface (contours are included as a guide to the eye).

The tilt ranges calculated with this procedure are summarized in Figure 4.7 as a function of copolymer architecture, film thickness, and thermal history. Both diblock and triblock copolymers (ABA) form lamellae that range in orientation from perpendicular to tilted, where the maximum tilt angle γ roughly increases with film thickness. A maximum tilt angle of $(45 \pm 10)^\circ$ is detected in films that are approximately three times thicker than the equilibrium periodicity ($t \simeq 3L_0$).

When we restrict the GISAXS measurements to the film surface ($\alpha_i > \alpha_c$), we

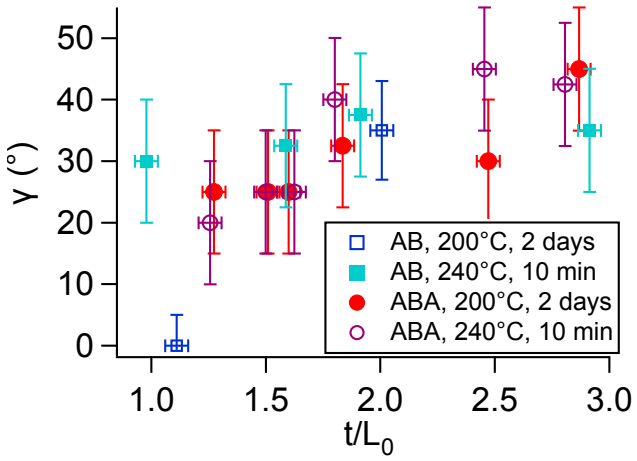

Figure 4.7: Summary of maximum lamellar tilt angles ($\pm\gamma$) for all samples measured with GISAXS.

find evidence that diblock and triblock domain orientations are different at the free surface. In diblock films, domains are perfectly perpendicular at the air interface ($\gamma = 0 \pm 10°$). In triblock films, the first-order diffraction peak is asymmetric in all samples, and the peak shape is consistent with the predicted profile for tilted domains. Such characteristics are observed in Figure 4.6(a) when $\alpha_i = 0.11°$. However, it is very difficult to distinguish between tilted domains and poorly-ordered perpendicular domains when $\alpha_i < \alpha_c$, so it is unclear if the tilt really persists at the near-surface region.

Tilted lamellae have been predicted and observed in AB copolymers assembled on incommensurate chemical templates [146–149]. In such systems, the chemical patterns have a strong affinity for a specific domain. When the pitch of chemical patterns is larger than L_0, the domains must either stretch to match the template or tilt to minimize the stretching penalty. In the present system, there is no periodic potential at the surfaces that could induce such frustration. We speculate that misoriented domains are kinetically-trapped: The molecular weights of our AB and

ABA copolymers are approximately 100 kDa and 200 kDa, respectively, so entanglements and slow diffusion could limit the rate of ordering [150, 151]. Furthermore, it is well-known that the energetic cost for bending lamellar domains is very small, as evidenced by "finger-print" patterns in thin films [26, 149], curved domains and "T-junctions" on epitaxial templates [152–154], and mixed domain orientations in thick copolymer films [155–157]. Considering our high molecular weights and the small energetic penalty for lamellar curvature, it is unlikely that further annealing would change the domain orientations. This is confirmed with in-situ GISAXS measurements, where additional annealing for 1 day at 235°C produces no detectable change in domain orientations.

Our GISAXS data suggest that reducing the molecular weights could improve the quality of AB and ABA thin films: Diblocks have a narrower line shape than triblocks, indicating they possess a higher degree of lateral order. Diblocks are also characterized by a "split" first-order diffraction peak when $\alpha_i > \alpha_c$, where these two peaks are associated with a "perfect" perpendicular phase and tilted domains, respectively. The diffraction peak associated with the "perfectly" oriented domains is noted by the arrow in Figure 4.6(b). In contrast, the higher molecular weight triblocks assemble into an imperfect perpendicular phase, meaning the film is characterized by a distribution of tilted domains with poor lateral ordering.

4.4 Conclusions

Domain orientations in thin films of lamellar poly(styrene-*b*-methyl methacrylate) (AB) and poly(methyl methacrylate-*b*-styrene-*b*-methyl methacrylate) (ABA) copolymers were evaluated as a function of film thickness, annealing temperature,

and annealing time. The objective was to identify conditions that offer a perpendicular domain orientation in thin films, emphasizing films that are thicker than the equilibrium domain periodicity L_0. Substrates were energetically "neutral" (or nearly neutral) with respect to the copolymer constituents, so domain orientations were largely controlled by surface energetics. For AB diblocks, the perpendicular orientation was reliably obtained for a broad range of film thickness when annealing temperatures were elevated ($> 220°$C) and the substrates had few imperfections. Reduced annealing temperatures and/or damaged substrates produce a mixture of parallel and perpendicular domain orientations. For ABA triblocks, the perpendicular domain orientation was easily generated for a broad range of film thicknesses and processing conditions, demonstrating the entropic preference for A endblocks at the free surface. Significantly, the data demonstrate that perpendicular domains are more easily achieved with triblocks than diblocks, particular in thicker films. Such behavior is beneficial for lithographic applications that require high-aspect-ratio nanostructures (such as plasma etching) [158]. However, the perpendicular phase in both diblocks and triblocks contains a high density of kinetically-trapped defects such as "tilted" domains. Longer annealing times did not reduce the defect density, but the data suggest that reducing the molecular weight of these copolymers will improve both the domain orientation and lateral ordering.

Chapter 5 Effects of Substrate Interactions on In-Plane and Out-of-Plane Order in Thin Films of Lamellar Copolymers

5.1 Introduction

Block copolymer thin films are widely investigated to enhance the resolution of the current lithographic techniques. Thin films of block copolymers (BCP) can be spun-cast on pre-patterned substrates and achieve higher density multiplication on the substrates. This technique of directed self-assembly is attractive to the semiconductor industry, but the electronics industry has low tolerance for defects [159–161]. Therefore, complete understanding of domain orientation in thin films of block copolymer on substrates is important. The objective of our studies in to investigate the effects of underlying substrate on in-plane and out-of-plane order.

Domain orientations in thin films of block copolymers is dependent on surface energetics. In order to balance surface energetics and achieve perpendicular domain orientations several techniques have been reported [27,121–123,125]. In our studies with diblock copolymer of lamellar poly(styrene-*b*-methyl methacryalate) (PS-PMMA), we used "neutral" substrates by spin casting polymer brushes on substrates [26,129,130]. This technique is widely used to achieve perpendicular orientations.

Previous studies have reported that in-plane order in BCP is sensitive to

polymer-substrate interactions. Lateral in-plane order changes depending on the interactions with the underlying substrate [162]. Recent studies have reported out-of-plane domain orientation in thin films of BCP. Thin films can have "tilted" domains on slightly preferential substrates [163].

In this work, we studied in-plane and out-of-plane ordering in thin films of PS-PMMA by varying the grafting density of polymer brushes on the substrates. We used hydroxyl-terminated poly(styrene-*co*-methyl methacrylate) random copolymers to prepare "neutral" substrates and processing conditions were varied to achieve different grafting densities of the polymer brushes. Un-grafted polymer was removed by rinsing in toluene. Thin films of PS-PMMA were spin coated on "neutral" brushes and were ordered by annealing at high temperature. Film thickness was varied from 25 nm to 120 nm. These films were investigated by microscopy and scattering techniques for in-plane and out-of-plane ordering. In-plane order improves as the film thickness of PS-PMMA increases and is better ordered on highly grafted polymer brush. Lateral in-plane order is better at the middle of the films than at interfaces. Out-of-plane ordering was best in thin films ($\leq$46 nm) and on highly grafted polymer brush. These results clearly indicate that polymer-substrates interactions have to be carefully tuned to achieve better order in thin films of block copolymers. Thick films of PS-PMMA have low free-energy penalty for bending and "tilted" domains were observed even on substrates with highly grafted polymer brushes.

5.2 Experimental Methods

Materials. The diblock copolymer used for these studies is a lamellar poly(styrene-*b*-methyl methacrylate) (PS-PMMA). The equilibrium lamellar periodicity (L_0) for

Table 5.1: Material Characteristics

Polymer	Styrene %	M_n (kDa)	PDI
PS-PMMA	53% vol	100	1.12
RCP A	62% mol	6.2	1.5
RCP B	64% mol	6.8	1.3

this PS-PMMA copolymer is 46 nm (measured with the grazing-incidence small angle X-ray scattering). Polymer brushes were prepared from hydroxyl-terminated poly(styrene-*co*-methyl methacrylate) random copolymers (RCPs). All polymers were purchased from Polymer Source and independently characterized at the University of Houston. The compositions, molecular weights, and polydispersity indices are reported in Table 5.1. Substrates were (100) oriented silicon wafers. Substrates were cleaned with a UVOCS UV/Ozone system for 20 mins to destroy organic contamination and grow a thin oxide layer.

Brush Preparation. RCPs were dissolved in toluene at a concentration of 1 wt %, and films that were approximately 30 nm thick were prepared by spin-casting on ultraclean silicon substrates. Polymer chains were grafted to the substrate by annealing under low vacuum (10 mTorr) or in nitrogen purged glove box for the temperature and time reported in Table 5.2. Processing conditions were varied to control the thickness of the polymer brushes. Un-grafted polymer was extracted by soaking in toluene with mild agitation. Samples were then dried with a nitrogen stream. The quality of the brush was assessed by measuring the contact angle of water, which was usually 76° after this process. Contact angle was increased to ca.78° by repeating all steps a second time (includes coating a new film, annealing, and rinsing). This outcome is consistent with other literature studies [131, 164].

Table 5.2: Brush thicknesses and grafting densities determined with spectroscopic ellipsometry (SE) and X-ray reflectivity (XRR).

Brush	T (°C)	τ (hr)	t_b^{SE} (nm)	ρ^{SE} (nm^{-2})	t_b^{XRR} (nm)	ρ^{XRR} (nm^{-2})	CA (°)
64% PS	170	48	5.0 ± 0.1	0.47	6.2 ± 0.1	0.59	78 ± 0.6
64% PS	170	24	4.1 ± 0.1	0.39	4.8 ± 0.1	0.45	77 ± 0.6
64% PS	230	1	3.5 ± 0.1	0.33	4.4 ± 0.1	0.41	78 ± 0.5
64% PS	210	1.5	3.0 ± 0.1	0.28	3.4 ± 0.1	0.32	77 ± 0.3
62% PS	170	48	2.5 ± 0.1	0.19	2.6 ± 0.1	0.19	80 ± 0.5

Brush Thickness. Brush and oxide thickness were measured using spectroscopic ellipsometry (SE) and X-ray reflectivity (XRR). SE measurements were performed with a J.A. Wollam M-2000 instrument (spanning 350-1700 nm). Each SE data set consists of the parameters Ψ and Δ that describe the change in polarization state of light [165]. SE data were modeled with a predetermined refractive index for each layer in the sample, so the only adjustable parameter for regression analysis was the thickness of oxide or polymer brush. The complex refractive index for the silicon substrate and silicon dioxide is part of a built-in database. The refractive index for RCP is well-described by the Cauchy dispersion relation $n(\lambda) = 1.52 + 0.01/\lambda^2$, where λ is the wavelength of incident light (units of nm). The oxidized silicon wafers were measured with SE prior to brush attachment, and the calculated oxide thickness was approximately 1.8 nm in all cases. The wafers were measured again after brush attachment, and Table 5.2 summarizes the brush thicknesses calculated from SE data (t_b^{SE}). XRR experiments were performed at the Advanced Photon Source of Argonne National Laboratory (beamline 8-ID-E) [166]. Data were acquired by varying the incident angle in the range of 0.1-2° using increments of 0.003°, and the intensity at specular reflection was recorded with an avalanche photodiode detector. XRR data were modeled following the Parratt recursions [167] convolved with an

Table 5.3: Surface energy measurements for polymer brushes.

Brush	t_{bSE}	Water (°)	Diiodomethane (°)	γ(mN/m)
62% PS	6.2 ± 0.1	78.8 ± 0.8	24.6 ± 0.6	50.7 ± 0.2
64% PS	2.6 ± 0.1	80.4 ± 0.4	23.4 ± 0.3	50.4 ± 0.2

instrumental resolution function [166], where brush thickness (t_b^{XRR}), brush scattering length density (ca. 10×10^{-10} cm^{-2}), and oxide thickness (ca. 1 nm) were refined through regression analysis. The fits are included in the Supporting Information. The brush thicknesses that were calculated from XRR are reported in Table 5.2. XRR can reliably distinguish between oxide and brush layers, while SE cannot differentiate between two optically transparent layers, so we refer to the more accurate XRR values throughout this manuscript.

Surface Energy. The surface energy of the polymer brushes was calculated from contact angle measurements based on Wu's harmonic method [168, 169]. Two liquids were used, deionized water and diiodomethane, and contact angles were recorded from at least three points on the substrate. These data are summarized in Table 5.3 for the thinnest and thickest brush, corresponding with the lowest and highest grafting densities, respectively.

PS-PMMA Thin Films. Thin films of PS-PMMA block copolymers were prepared on the RCP brushes. Polymers were dissolved in toluene at concentrations that ranged from 1-4 wt%, and solutions were filtered with a 0.2 μm Teflon mesh. Films that ranged in thickness from 20 nm to 120 nm were prepared by spin-casting. Film thicknesses were measured with J.A. Wollam M-2000 spectroscopic ellipsometry. The parameters Δ and Ψ were modeled with the Cauchy dispersion relation

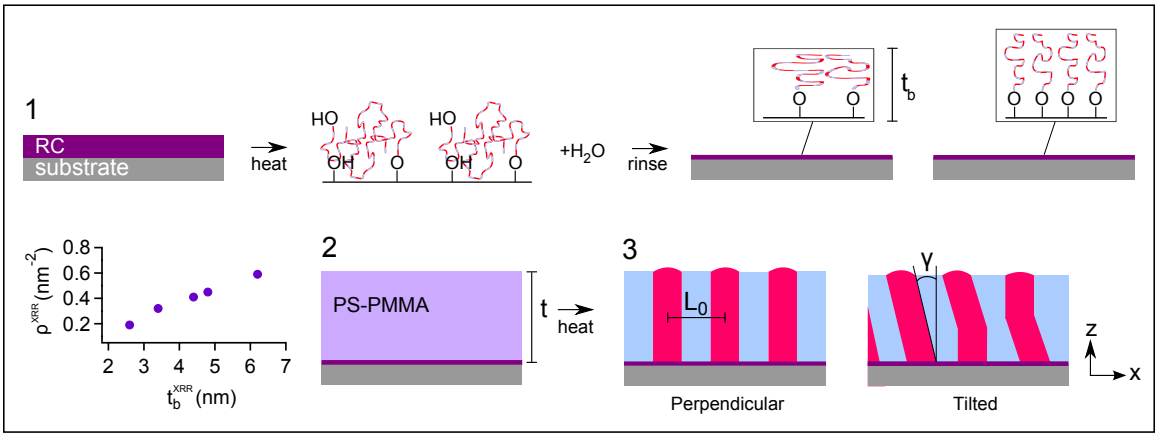

Figure 5.1: Schematic of sample preparation and types of lamellar structures that are detected in experiments.

$n(\lambda) = A + B/\lambda^2$, where A, B, and film thickness were adjustable parameters for regression analysis (all positive values). Typical values for the Cauchy constants are $A = 1.52$ and $B = 0.01$. The BCPs were ordered by annealing in air for 10 minutes at 240°C. The segregation strength is approximately $\chi N \simeq 45$ at 240°C [138, 170]. Other studies have demonstrated that short annealing at high temperature is similar to prolonged vacuum annealing at moderate temperature [163, 171]. Figure 5.1 gives the overview of sample preparation and types of lamellar structures. (1) Thin film of random copolymer (RC) is cast on an ultraclean silicon substrate. Polymer is grafted to the substrate, and un-grafted polymer is removed to reveal the "neutral" polymer brush. Polymer brush thickness (t_b) is varied by varying the processing conditions. Plot denotes the brush thickness (t_b^{XRR}, measured using X-ray reflectivity) and corresponding grafting density. (2) Thin film of PS-PMMA copolymer (thickness t) is spun cast on top of the brush. (3) Ordering of lamellar domains by heating above the glass transition. Domains can be oriented as perfect perpendicular orientation or perpendicular phase with "tilt" defects.

Microscopy. The nanoscale structure at the surface of each film was characterized with atomic force microscopy (AFM) and/or scanning electron microscopy (SEM). AFM micrographs were collected with a MultiMode 3 (Veeco) in Tapping Mode using silicon probes with a spring constant of approximately 40 N/m. Typical parameters for data acquisition were 1.7 Hz scan frequency, 5 μm $\times$ 5 μm scan area, and 512 $\times$ 512 image resolution. The SEM images were recorded with a FEI XL-30FEG SEM in the secondary electrons (SE) mode. The parameters used were an accelerating voltage of 5 kV, beam current of 95 pA, working distance of 5 mm and magnifications ranging from 50-65 kx. Lateral domain order was quantified by calculating the orientational correlation function $g(\vec{r})$ and fitting the azimuthal average to an exponential decay, i.e., $g(r) = exp(-r/\zeta)$ [172–174]. Average values of the orientational correlation length ζ (normalized by $L_0 = 46$ nm) were computed from a minimum of 5 micrographs, and error bars denote the standard deviation. We have verified that the ζ values calculated from AFM and SEM are identical within error (see Supporting Information).

Plasma Etching. Lateral order was investigated throughout the thickness of selected PS-PMMA films by successive etching and imaging steps. The films were cast with an thickness of $t = 2L_0 \simeq 90$ nm on different RCP brushes (6.2, 3.4, and 2.6 nm thick). Each sample was annealed as previously described, and then cut into several smaller pieces. Each piece was then etched to a specific depth using oxygen plasma generated with an Oxford Plasma Lab 80 Plus reactive ion etch (RIE) system. The typical parameters for etching were 20 sccm oxygen, 700 mTorr pressure, 98 W power, and 234 V DC bias. The Supporting Information includes the etch rates for PS, PMMA, and PS-PMMA films.

Grazing-Incidence Small Angle X-Ray Scattering (GISAXS). GISAXS experiments from the PS-PMMA films were conducted at the Advanced Photon Source of Argonne National Laboratory (beamline 8-ID-E) [166]. Samples were placed in a vacuum chamber and illuminated with 7.35 keV radiation at incident angles (α_i) in the range of $0.1 - 0.24°$. The off-specular scattering was recorded with a Pilatus 1MF pixel array detector (pixel size = 172 μm) positioned 2175 mm from the sample. Acquisition times were approximately 10 sec per frame.Each data set is stored as a 981×1043 32-bit tiff image with 20-bit dynamic range. Note that x-ray penetration depth varies from approximately 10 nm up to the full film thickness as incident angle is varied near the critical angle of the film (ca.0.17°). All data are displayed as intensity maps $I(2\Theta, \alpha_f)$, where 2Θ and α_f denote in-plane and out-of-plane diffraction angles, respectively. In addition to GISAXS, we measured XRR and rocking curves for each sample at the same beam line. These data are needed for quantitative analysis of GISAXS patterns as described in the Results and Discussion. XRR measurements were used to quantify the thickness and density of polymer and oxide layers. Data were acquired by varying the incident angle in the range of 0.1-2° using increments of 0.003°, and the intensity at specular reflection was recorded with an avalanche photodiode detector. XRR data were modeled following the Parratt recursions [167] convolved with an instrumental resolution function [166], where polymer thickness (t_b^{XRR}), polymer scattering length density (ca. 10×10^{-10} cm^{-2}), and oxide thickness (ca. 1 nm) were refined through regression analysis. Rocking curves were used to quantify the effects of water curvature on the incident beam angle. These measurements were implemented by setting the incident angle to 0.4° and scanning an avalanche photodiode detector about the specular condition (from 0.35° - 0.45° in

increments of 0.003 °). These data were fit to a Gaussian resolution function,

$$R(q_z) = \frac{1}{\sqrt{2\pi}\delta_{q_z}} exp(-\frac{{q_z}^2}{2{\delta_{q_z}}^2}), \tag{5.1}$$

where q_z is the perpendicular scattering vector (out of plane) and $\delta_{q_z} = (\Delta\lambda/\lambda)q_z + 4\pi\Delta\alpha/\lambda$. The wavelength spread is $\Delta\lambda/\lambda = 10^{-4}$ (fixed) [166], and the angular divergence of the beam ($\Delta\alpha$) is an adjustable parameter for regression analysis. The angular divergence is typically 5×10^{-5} rad.

5.3 Results and Discussion

The aim of these studies is to examine the effects of substrate interactions on in-plane and out-of-plane order in lamellar PS-PMMA block copolymers. All PS-PMMA films were cast on silicon wafers that were functionalized with random copolymer P(S-co-MMA) brushes, and substrate interactions were tuned by varying the graft density of the brush. We refer to substrates with polymer brush as "neutral" substrates. We anticipate that substrates with low graft densities will "pin" the lamellar domains and trap a higher density of defects.

The graft density σ for each sample was calculated from the measured brush thickness t_b,

$$\sigma = \frac{t_b \rho N_A}{M_n}, \tag{5.2}$$

where $\rho = 1.1$ g/cm^3 is the approximate polymer density, N_A is Avogadro's number, and M_n is the number-average molecular weight. Using the brush thickness calculated from XRR, we estimate that ρ ranges from 0.2 to 0.6 chains/nm^2 (Table 5.2).

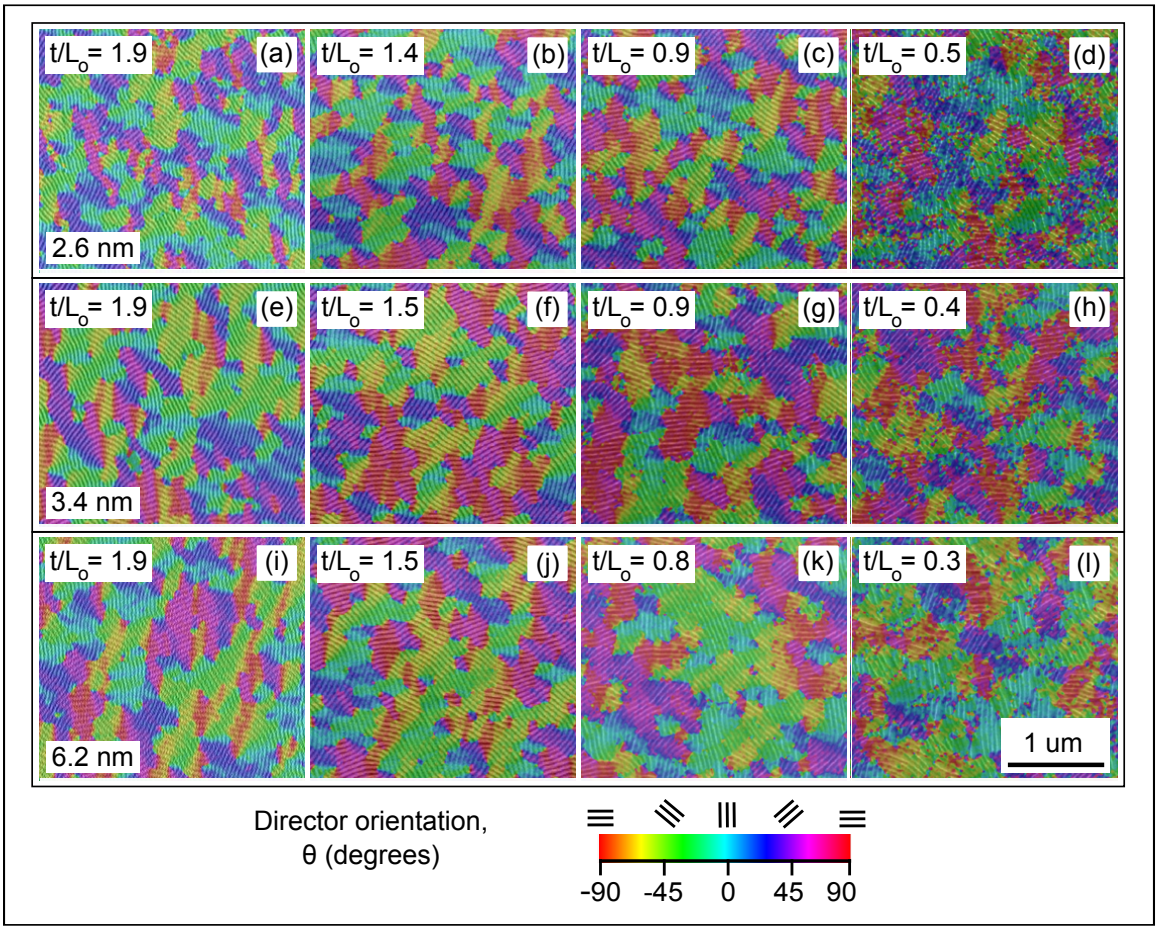

Figure 5.2: Color maps superposed on microscopy images. Domains in PS-PMMA films were ordered by annealing at 240°C for 10 minutes.

In-Plane Order Thin films of PS-PMMA were spun cast on "neutral" substrates and ordered by annealing at 240°C for 10 minutes (as mentioned in the Experimental Procedures). These films were investigated for in-plane order at both polymer-air interface and throughout the film thickness. Polymer-air interface of PS-PMMA films was first inspected under bright-field optical microscopy. All films were observed to be flat which corresponds to nearly balanced surface energetics at both polymer-air and polymer-substrate interfaces. In order to resolve the nanostructured domains at polymer-air interface, PS-PMMA films were imaged using atomic force microscopy (AFM) and/or scanning electron microscopy (SEM). AFM phase or SEM images can clearly resolve PS and PMMA domains. Films with distinct PS and PMMA domains with domain spacing of ∼46 nm corresponds to perpendicular orientations at polymer-air interface. All PS-PMMA films studied showed perpendicular orientations at the polymer-air interface. Any films with slight deviation from perpendicular orientations were marked separately. Lateral domain order throughout the film thickness was investigated for selected PS-PMMA films by successive etching and imaging steps as described in the experimental procedures.

Figure 5.2 shows microscopy images with superposed color maps. Domains with same lateral order are denoted with same color. This can be seen in the color bar with corresponding director orientation (θ). Figure 5.2 (a), (e), (i) are PS-PMMA thin films of thickness $t \approx 2L_0$ on "neutral" substrates with brush thicknesses 2.6 nm, 3.4 nm and 6.2 nm. Lateral order was studied throughout the film thickness by successive etching and imaging. Figure 5.2 (b-d), (f-h), (j-l) show microscopy images of polymer-air interface after successive etching with superposed color maps. Initially started with samples with film thickness of $2L_0$, which were etched and imaged for thicknesses $\sim 1.5L_0$, $\sim 0.9L_0$ and $\sim 0.4L_0$. PS and PMMA domains etch at different

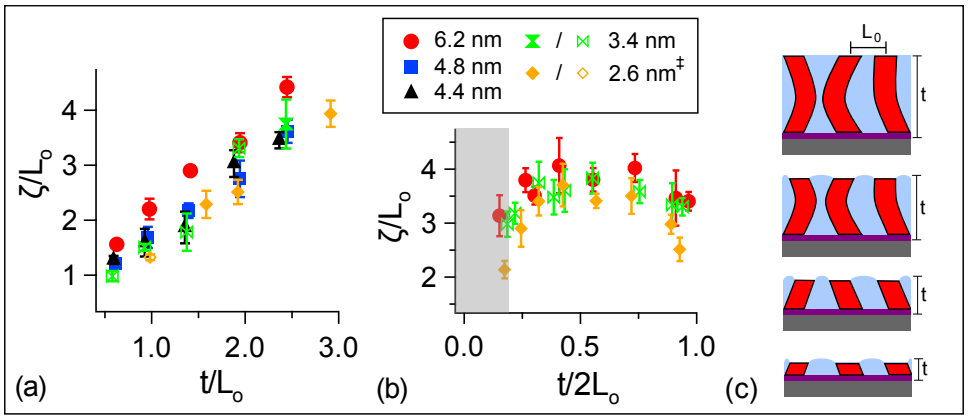

Figure 5.3: (a,b) Normalized orientational correlation length (ζ/L_0) calculated from microscopy images as a function of film thicknesses and brush thicknesses. As-cast films were annealed at 240°C for 10 minutes. (b) ζ/L_0 measured throughout the PS-PMMA film. (c) Cartoon showing the tilted domains.

rates and microscopy image quality is improved until it reaches the both of the film. These microscopy images were superposed with color maps. All microscopy images were processed and lateral domain order was quantified by calculating orientational correlation length (ζ) using the procedure mentioned in the experimental section.

Figure 5.3 (a) plots ζ/L_0 as a function of PS-PMMA film thickness and brush thickness. Legend denotes brush thicknesses, with closed symbols denote PS-PMMA films with perpendicular domains at polymer-air interface where as open symbols denote films with small fraction (≤ 0.02) of parallel domain orientation. All brushes were prepared with 64% PS except for 2.6 nm brush with 62% PS fraction (denoted by ‡). In-plane order in PS-PMMA thin films on all "neutral" substrates improves as the film thickness increases. This suggests that substrate interactions are significantly reduced as the film thickness increases. These results were consistent with previous works done by other groups [164]. Scaling exponent (n) was evaluated for orientational

Table 5.4: Scaling exponent (n) for orientational correlation length as a function of film thickness, i.e., $\zeta/L_0 \sim (t/L_0)^n$

Brush	t_b^{XRR} (nm)	n
64% PS	6.2±0.1	0.73±0.03
64% PS	4.8±0.1	0.76±0.03
64% PS	4.4±0.1	0.74±0.10
64% PS	3.4±0.1	0.95±0.11
62% PS	2.6±0.1	0.98±0.06

correlation length as a function of film thickness using the relation [175],

$$\frac{\zeta}{L_0} = \left(\frac{t}{L_0}\right)^n . \tag{5.3}$$

The values of n evaluated of PS-PMMA films on different "neutral" substrates were tabulated in Table 5.4. Scaling exponent (n) is low for PS-PMMA films spun-cast on highly grafted polymer brushes. This suggests that thicker brushes will reduce the influence of substrate interactions on lateral order.

In-plane order throughout film thickness was done using successive etch and image studies. Figure 5.3 (b) plots ζ/L_0 as the function of film thickness. Legend denotes brush thicknesses, with closed symbols denote PS-PMMA films with perpendicular domains at polymer-air interface where as open symbols denote films with small fraction ($\leq$ 0.02) of parallel domain orientation. All brushes were prepared with 64% PS except for 2.6 nm brush with 62% PS fraction (denoted by ‡). PS-PMMA films of initial thickness $2L_0$ was successively etched and imaged. In-plane order improves as the film is etched half way and decreases on further etching. Influence of interfaces in minimized at the middle of the film. Shaded region denotes the thickness range of poor microscopy image. Image quality reduces because of poor

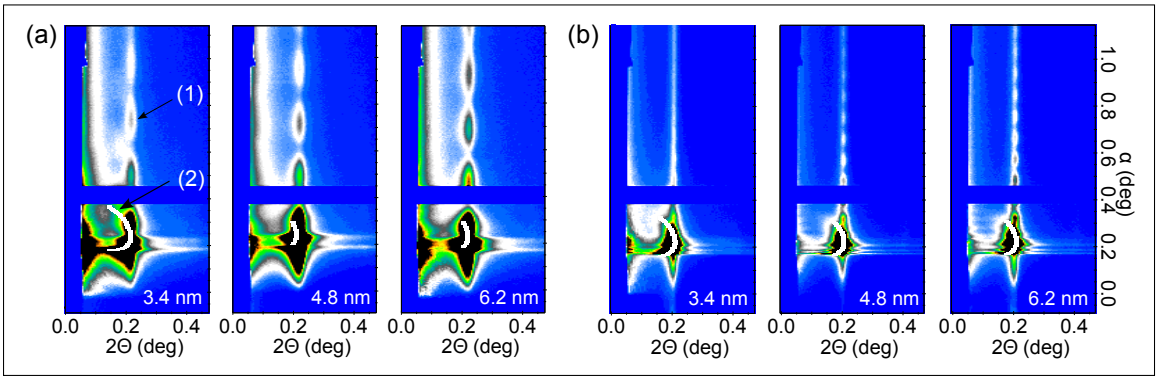

Figure 5.4: GISAXS data for diblock copolymer thin films (a) $t/L_0 = 1$ and (b) $t/L_0 = 2.5$ on three different substrates annealed at 240°C for 10 minutes. Incident angle (α_i) at which data was collected is 0.22°.

contrast, which make it difficult to run the algorithm for estimating lateral in-plane order. The improved ζ/L_0 at the middle of the film was observed for films on three different brushes and is found to be better on thicker brush. This suggests that the influence of both polymer-substrates and polymer-air interface are minimized at the middle of the film. With varying in-plane order throughout the film, we expect the domains to be "tilted" throughout the film thickness. Figure 5.3 (c) shows the cartoon for the PS-PMMA films with "tilted" domains that are etched for different film thickness. In order to understand "tilt" defects in the domain, out-of-plane ordering has to be investigated.

Out-of-plane ordering Microscopy technique does not provide complete information on domain ordering throughout the film thickness. Out-of-plane ordering in thin films of PS-PMMA was investigated using grazing-incidence small angle X-ray scattering (GISAXS) technique. All PS-PMMA samples studied were measured for GISAXS data at the beamline (mentioned in Experimental Procedures). The incident angle (α_i) was varied above the critical angle (i.e., 0.17°) [143] of polymer system to

study domain ordering through the entire film thickness. In order to quantify the out-of-plane ordering, two sets of analysis were done. First, (a) Fitting the first-order diffraction rod and second, (b) Mapping the powder rings. Figure 5.4 shows GISAXS data collected at angle of incidence of 0.22° for PS-PMMA films of thickness $\sim L_0$ and $\sim 2.5L_0$ annealed at 240°C for 10 minutes. GISAXS data is shown for PS-PMMA films on three substrates of brush thickness (t_b^{XRR}) 3.4 nm, 4.8 nm and 6.2 nm. The first-order diffraction rod in PS-PMMA films (denoted by (1) in Figure 5.4) becomes well-defined as the thickness of underlying brush increases. This can be observed in both thin and thick PS-PMMA films. The distribution of tilted domains in the PS-PMMA films was studied by mapping the powder rings contours (denoted by (2)) with the experimental data. Tilted domain orientation are significant in thick PS-PMMA films when compared to thin films on highly grafted polymer brushes. To quantify the range of tilt angles $\pm\gamma$ throughout the film, line cuts were extracted from first-order diffraction rod of all samples. These line cuts were fit using Distorted-wave Born Approximation, following procedures described elsewhere [143, 176]:

$$\begin{aligned} I(q_x, q_y, q_z) \propto |&T^f T^i P(q_{par}, q_{z1}) S(q_{par}, q_{z1}) \\ &+ T^f T^i P(q_{par}, q_{z2}) S(q_{par}, q_{z2}) \\ &+ T^i T^f P(q_{par}, q_{z3}) S(q_{par}, q_{z3}) \\ &+ R^f R^i P(q_{par}, q_{z4}) S(q_{par}, q_{z4})|^2, \end{aligned} \tag{5.4}$$

where T^f, T^i, R^f and R^i are the amplitudes of the transmitted and reflected waves. Outgoing and incoming waves are denoted by superscripts f and i, respectively. q is the scattering vector, $S(q)$ is the structure factor and $P(q)$ is the form factor. The fitting was done to estimate the distribution of tilt angles in the polymer system.

Figure 5.5 (a) shows the fits for first-order diffraction rod for PS-PMMA films on

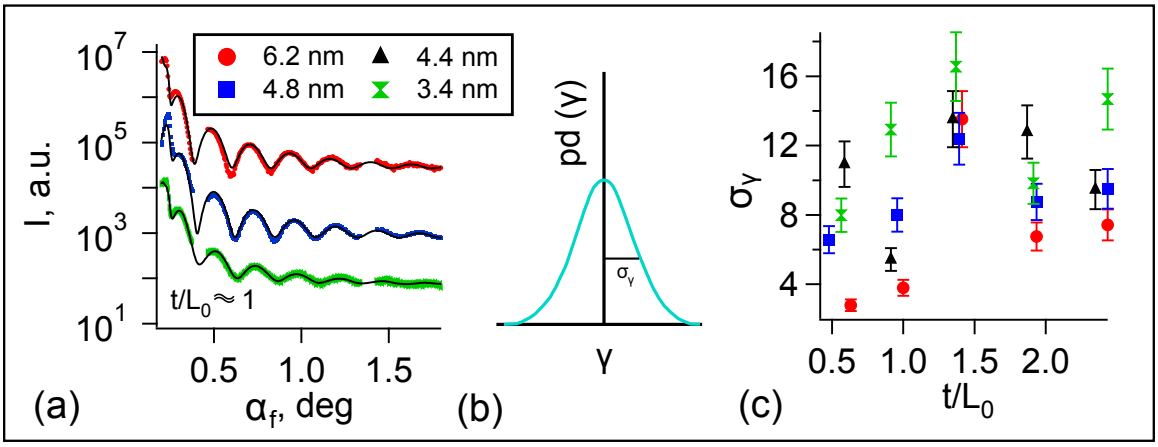

Figure 5.5: (a) Data and fit for first-order diffraction rod for $t/L_0 = 1$ and on three different substrates. (b) Cartoon denoting the distribution of tilt angles (σ_γ). γ is the tilt angle. (c) σ_γ was plotted as a function of film thicknesses and brush thicknesses.

three different brushes annealed at 240°C for 10 minutes. Incident angle (α_i) at which data was collected is 0.22°. The distribution of tilt angles was estimated from the fits. Figure 5.5 (b) denotes the probability density of tilt angle (γ) and its distribution (σ_γ). All samples were processed to extract the first-order diffraction rod and were fit to estimate σ_γ. Figure 5.5 (c) shows the plot of σ_γ as function of PS-PMMA film thicknesses and brush thicknesses. σ_γ increases as the film thickness increases, suggesting that the out-of-plane order is best in thin films ($t \leq L_0$) and on highly grafted polymer brush. σ_γ is low on the thickest brush (6.2 nm), this suggests that out-of-plane ordering is improved when the grafting density of underlying substrate is improved.

Another approach to evaluate the range of tilt angles is by matching the GISAXS powder ring to the simulated contour. The samples were processed and range of tilt angles were plotted in Figure 5.6 (a). As-cast films were annealed at 240°C for 10 minutes. t denotes the thickness of the film, L_0 is the lamellar periodicity. Simulated

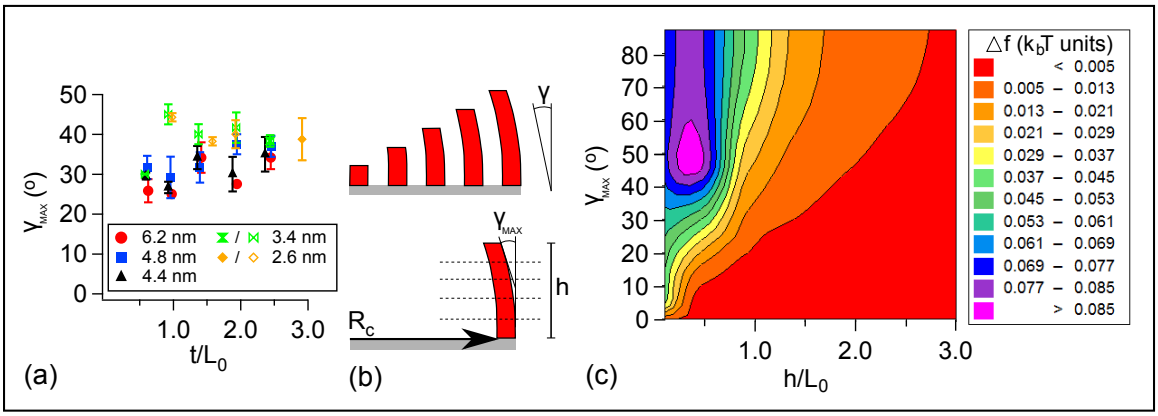

Figure 5.6: (a) Maximum tilt angle range estimated by mapping the powder rings as a function of film thickness and brush thickness. (b) Cartoon depicts the change in tilt angle as the film thickness increases. (c) Free energy penalty for bending.

contour was mapped with experimental Debye-Scherrer rings [145] to evaluate the parameter γ for each data set. In $(2\Theta, \alpha_f)$ space, partial rings are simulated with a straightforward procedure: First, the scattering vector for lamellae tilted through an angle $\pm\gamma$ is defined as $\vec{q_r} = \vec{q} \cdot R$, where $\vec{q} = \{q_{xy}, q_z\} = \{2\pi/L_0, 0\}$ is the scattering vector for perpendicular lamellae and R is a two-dimensional rotation matrix. Second, the contours for partial Debye-Scherrer rings in $(2\Theta, \alpha_f)$ space are calculated from Equations 5.5-5.6 [142–144]:

$$\alpha_f = \arcsin \sqrt{\left(\frac{q_{z,r}}{k}\right)^2 + \sin^2 \alpha_i \pm 2\frac{q_{z,r}}{k}\sqrt{n^2 - 1 + \sin^2 \alpha_i}}, \tag{5.5}$$

and

$$2\Theta = \arccos\left(\frac{\cos^2 \alpha_f + \cos^2 \alpha_i - (q_{xy,r}/k)^2}{2\cos\alpha_f \cos\alpha_i}\right), \tag{5.6}$$

where n and α_i are the refractive index of PS-PMMA and GISAXS incident angle, respectively, while $k = 2\pi/\lambda$. Simulated contour of partial Debye-Scherrer rings was compared with experimental data and tilt range $\pm\gamma$ was estimated. The simulated

contour was truncated to the point where the intensity fall to 20% of the maximum intensity. Figure 5.6(a) summarizes the $\pm\gamma$ estimated for all PS-PMMA films studied. Tilted domains become significant as the film thickness increases. Out-of-plane ordering is better in thin films spun-cast on polymer brushes with high grafting density. These results are consistent with the conclusions from fitting first-order diffraction rod. Cartoon in Figure 5.6(b) depicts the domains with increasing thickness. Here, R_c is the radius of curvature and h denotes the average height of the tilted domains. Thick films are more likely to bend when compared to thin films. Maximum tilt angle increases as the film thickness increases. The free energy penalty of bending was theoretically evaluated for PS-PMMA films using the formula [152]:

$$\nabla f = \frac{1}{2} K_{lam} (\frac{1}{R_c})^2, \tag{5.7}$$

where ∇f is the free energy penalty per chain, R_c is the radius of curvature of the perpendicular lamellae and K_{lam} is the elastic coefficient of the lamellar phase.

K_{lam} in the strong segregation limit is given by,

$$K_{lam} = \frac{\pi^2}{1024} \frac{L^4 k_B T}{N a^2}, \tag{5.8}$$

where L is the lamellar domain spacing, k_B is the Boltzmann constant, T is temperature, N is the polymerization index, and a is the statistical segment length. In our case based on the scaling relationship based on the MW of the PS-PMMA system, we used $L = 46.0$ nm, $a = 0.52$, $N = 1010.29$.

The geometry of the system $\sin\gamma = \frac{t}{R_c}$ is used to understand the free energy penalty variation with thickness and tilt angle for a range of radius of curvatures R_c. (Figure 5.6(c)) Free energy penalty for bending the domain was estimated for our

lamellar PS-PMMA system compared to the theoretical allowed ranges and is low for thick films. As a result, the tilt angles are high for thick PS-PMMA films. The range of tilt angles for PS-PMMA films we studied falls within a narrow spectrum of the free energy landscape. GISAXS analysis suggests that out-of-plane ordering is better in thin PS-PMMA films and on highly grafted polymer substrates. Thicker films have low free energy of penalty, so tilted domains are more significant.

5.4 Conclusions

We studied the effects of substrate on in-plane and out-of-plane ordering in thin films of PS-PMMA. PS-PMMA films were spun-cast on substrates with varying grafting density of polymer brushes. In-plane order improves as the film thickness increases and is better on highly grafting polymer brush. Lateral order throughout the film thickness was investigated by successive etch and image studies. In-plane order is better at the middle of the film when compared to interfaces, suggesting that the out-of-plane domain ordering is tilted or bent. GISAXS analysis was done to investigate the out-of-plane ordering. While out-of-plane order improves for all film thicknesses on densely grafted brushes, there are more tilt defects in thick films compared with thin films. This behavior is explained by the low free energy penalty for bending a tall domain.

Chapter 6 Outlook

6.1 Outlook

Printing polymer films for organic electronics. We developed a simple approach to generate conductive nanostructures and microstructures using electron-beam lithography or proximity ion beam lithography. π-conjugated polymers on exposure to radiation generates intermolecular cross-links, where the size, shape, and density of polymer domains are all tunable parameters. Cross-linked polymers are resistant to solvent and thermal processing, so systematic structure-property studies were established in polymer-based solar cells. The power-conversion efficiency of these model devices improves with increasing interfacial area. The effects of radiation were investigated to completely understand cross-linked polymer system. Charge-carrier mobility and degree of crystallization were reduced by 50% for low-to-moderate exposure doses. Solvent effects have to be understood during the process of development. Preliminary studies suggest that solvent exposure induces further changes in crystallinity. Currently, cross-linking mechanism is investigated using X-ray photoelectron spectroscopy technique. This technique helps in investigating the chemical changes in polymer system due to the exposure to radiation.

It is likely that the patterning techniques can be extended to other classes of polymer semiconductors that have alkyl substituents, including new high-performance materials that are investigated for photovoltaics. We believe these materials can be patterned using lower doses of radiation because they are less soluble in organic

solvents than poly(alkylthiophene), meaning a lower crosslink density will effect the solubility switch. This technique can then be leveraged to investigate structure-property relations as a function of device architecture.

Nanopatterning using thin films of block copolymers. We have investigated the effects of architecture on domain orientation in thin films of block copolymers. Perpendicular orientations can be achieved in triblock copolymers easily when compared to diblock copolymers. Triblocks are easier to process for applications requiring high-aspect-ratio nanostructures. However, both diblock and triblock copolymer films are associated with high density of tilt defects. Further studies were done in understanding the effects of substrate on in-plane and out-of-plane ordering. Thin films of diblock copolymers were prepared on substrates with varying grafting densities. In-plane ordering improves as the film thickness increases and is better ordered on thicker brush. In-plane order is better in the middle of the film when compared to interfaces, suggesting that the domains are tilted. Grazing-incidence small angle X-ray scattering technique was used to investigate the out-of-plane ordering. Thin films on highly grafted brushes have good out-of-plane ordering, whereas thick films due to less free energy penalty have misoriented or tilted domains.

Future studies will extend this understanding of block-copolymer substrate interactions to directed self assembly, a technique that is widely studied for fabrication of integrated circuits and disk drives (bit patterned media) [159, 160]. Directed self-assembly uses a template to control lateral domain placement. Recent experimental and theoretical works have suggested that interactions at the substrate can induce complex three-dimensional structures [177,178], but the current understanding of this behavior is quite limited.

References

[1] P. W. M. Blom, V. D. Mihailetchi, L. J. A. Koster, and D. E. Markov, "Device physics of polymer:fullerene bulk heterojunction solar cells," *Advanced Materials*, vol. 19, pp. 1551–1566, 2007.

[2] K. M. Coakley and M. D. McGehee, "Conjugated polymer photovoltaic cells," *Chem. Mater.*, vol. 16, pp. 4533–4542, 2004.

[3] R. Gaudiana, "Organic photovoltaics: Challenges and opportunities," *Journal of Polymer Science Part B: Polymer Physics*, vol. 50, pp. 1014–1017, 2012.

[4] G. Dennler, M. C. Scharber, and C. J. Brabec, "Polymer-fullerene bulk-heterojunction solar cells," *Adv. Mater.*, vol. 21, pp. 1323–1338, 2009.

[5] B. C. Thompson and J. M. J. Frechet, "Organic photovoltaics - polymer-fullerene composite solar cells," *Angewandte Chemie-International Edition*, vol. 47, no. 1, pp. 58–77, 2008.

[6] J. Nelson, "Diffusion-limited recombination in polymer-fullerene blends and its influence on photocurrent collection," *Physical Review B*, vol. 67, p. 155209, 2003.

[7] M. Mayukh, I. H. Jung, F. He, and L. Yu, "Incremental optimization in donor polymers for bulk heterojunction organic solar cells exhibiting high performance," *Journal of Polymer Science Part B: Polymer Physics*, vol. 50, pp. 1057–1070, 2012.

[8] M. A. Brady, G. M. Su, and M. L. Chabinyc, "Recent progress in the morphology of bulk heterojunction photovoltaics," *Soft Matter*, vol. 7, no. 23, pp. 11065–11077, 2011.

[9] B. A. Gregg, "Excitonic solar cells," *J. Phys. Chem. B*, vol. 107, pp. 4688–4698, 2003.

[10] B. A. Collins, J. R. Tumbleston, and H. Ade, "Miscibility, crystallinity, and phase development in p3ht/pcbm solar cells: Toward an enlightened understanding of device morphology and stability," *J. Phys. Chem.Lett.*, vol. 2, pp. 3135–3145, 2011.

[11] J.-T. Chen and C.-S. Hsu, "Conjugated polymer nanostructures for organic solar cell applications," *Polym. Chem.*, vol. 2, p. 2707, 2011.

[12] M.-Y. Chiu, U.-S. Jeng, C.-H. Su, K. S. Liang, and K.-H. Wei, "Simultaneous use of small- and wide-angle x-ray techniques to analyze nanometerscale phase separation in polymer heterojunction solar cells," *Adv. Mater.*, vol. 20, pp. 2573–2578, 2008.

[13] S. Swaraj, C. Wang, H. Yan, B. Watts, J. Luning, C. R. McNeill, and H. Ade, "Nanomorphology of bulk heterojunction photovoltaic thin films probed with resonant soft x-ray scattering," *Nano Lett.*, vol. 10, pp. 2863–2869, 2010.

[14] D. Chen, A. Nakahara, D. Wei, D. Nordlund, and T. P. Russell, "P3HT/PCBM Bulk Heterojunction Organic Photovoltaics: Correlating Efficiency and Morphology," *Nano Letters*, vol. 11, pp. 561–567, FEB 2011.

[15] I. Botiz and S. B. Darling, "Optoelectronics using block copolymers," *Materials Today*, vol. 13, pp. 42–51, MAY 2010.

[16] H. Xin, O. G. Reid, G. Ren, F. S. Kim, D. S. Ginger, and S. A. Jenekhe, "Polymer Nanowire/Fullerene Bulk Heterojunction Solar Cells: How Nanostructure Determines Photovoltaic Properties," *ACS Nano*, vol. 4, pp. 1861–1872, APR 2010.

[17] M. Aryal, F. Buyukserin, K. Mielczarek, X.-M. Zhao, J. Gao, A. Zakhidov, and W. W. Hu, "Imprinted large-scale high density polymer nanopillars for organic solar cells," *Journal of Vacuum Science & Technology B*, vol. 26, pp. 2562–2566, NOV 2008. 52nd International Conference on Electron, Ion and Photon Beam Technology and Nanofabrication, Portland, OR, MAY 27-30, 2008.

[18] X. He, F. Gao, G. Tu, D. G. Hasko, S. Huettner, N. C. Greenham, U. Steiner, R. H. Friend, and W. T. S. Huck, "Formation of Well-Ordered Heterojunctions in Polymer: PCBM Photovoltaic Devices," *Advanced Functional Materials*, vol. 21, pp. 139–146, JAN 7 2011.

[19] D. Chen, W. Zhao, and T. P. Russell, "P3HT Nanopillars for Organic Photovoltaic Devices Nanoimprinted by AAO Templates," *ACS Nano*, vol. 6, pp. 1479–1485, FEB 2012.

[20] M. Fasolka and A. Mayes, "Block copolymer thin films: Physics and applications," *Annual Review of Materials Research*, vol. 31, pp. 323–355, 2001.

[21] C. T. Black, R. Ruiz, G. Breyta, J. Y. Cheng, M. E. Colburn, K. W. Guarini, H.-C. Kim, and Y. Zhang, "Polymer self assembly in semiconductor microelectronics," *IBM Journal of Research and Development*, vol. 51, pp. 605–633, SEP 2007.

[22] R. Segalman, "Patterning with block copolymer thin films," *Materials Science & Engineering R-Reports*, vol. 48, pp. 191–226, FEB 28 2005.

[23] J. Bang, U. Jeong, D. Y. Ryu, T. P. Russell, and C. J. Hawker, "Block Copolymer Nanolithography: Translation of Molecular Level Control to Nanoscale Patterns," *Advanced Materials*, vol. 21, pp. 4769–4792, DEC 18 2009.

[24] F. Bates and G. Fredrickson, "Block Copolymer Thermodynamics - Theory and Experiment," *Annual Review of Physical Chemistry*, vol. 41, pp. 525–557, 1990.

[25] C. M. Bates, J. R. Strahan, L. J. Santos, B. K. Mueller, B. O. Bamgbade, J. A. Lee, J. M. Katzenstein, C. J. Ellison, and C. G. Willson, "Polymeric Cross-Linked Surface Treatments for Controlling Block Copolymer Orientation in Thin Films," *Langmuir*, vol. 27, pp. 2000–2006, MAR 1 2011.

[26] P. Mansky, Y. Liu, E. Huang, T. Russell, and C. Hawker, "Controlling polymer-surface interactions with random copolymer brushes," *Science*, vol. 275, pp. 1458–1460, MAR 7 1997.

[27] E. Huang, T. Russell, C. Harrison, P. Chaikin, R. Register, C. Hawker, and J. Mays, "Using surface active random copolymers to control the domain orientation in diblock copolymer thin films," *Macromolecules*, vol. 31, pp. 7641–7650, NOV 3 1998.

[28] M. Turner, "Equilibrium properties of a diblock copolymer lamellar phase confined between flat plates," *Physical Review Letters*, vol. 69, pp. 1788–1791, SEP 21 1992.

[29] N. Koneripalli, F. Bates, and G. Fredrickson, "Fractal hole growth in strained block copolymer films," *Physical Review Letters*, vol. 81, pp. 1861–1864, AUG 31 1998.

[30] V. Khanna, E. W. Cochran, A. Hexemer, G. E. Stein, G. H. Fredrickson, E. J. Kramer, X. Li, J. Wang, and S. F. Hahn, "Effect of chain architecture and surface energies on the ordering behavior of lamellar and cylinder forming block copolymers," *Macromolecules*, vol. 39, pp. 9346–9356, DEC 26 2006.

[31] M. W. Matsen, "Architectural Effect on the Surface Tension of an ABA Triblock Copolymer Melt," *Macromolecules*, vol. 43, pp. 1671–1674, FEB 9 2010.

[32] J. K. Bosworth, E. A. Dobisz, O. Hellwig, and R. Ruiz, "Impact of out-of-plane translational order in block copolymer lithography," *Macromolecules*, vol. 44, pp. 9196–9204, 2011.

[33] C. Deibel and V. Dyakonov, "Polymer-fullerene bulk heterojunction solar cells," *Reports on Progress in Physics*, vol. 73, 2010.

[34] C. H. Woo, B. C. Thompson, B. J. Kim, M. F. Toney, and J. M. J. Frechet, "The Influence of Poly(3-hexylthiophene) Regioregularity on Fullerene-Composite Solar Cell Performance," *Journal of the American Chemical Society*, vol. 130, pp. 16324–16329, DEC 3 2008.

[35] M. R. Hammond, R. J. Kline, A. A. Herzing, L. J. Richter, D. S. Germack, H.-W. Ro, C. L. Soles, D. A. Fischer, T. Xu, L. Yu, M. F. Toney, and D. M. DeLongchamp, "Molecular Order in High-Efficiency Polymer/Fullerene Bulk Heterojunction Solar Cells," *ACS Nano*, vol. 5, pp. 8248–8257, OCT 2011.

[36] J. Weickert, R. B. Dunbar, H. C. Hesse, W. Wiedemann, and L. Schmidt-Mende, "Nanostructured Organic and Hybrid Solar Cells," *Advanced Materials*, vol. 23, pp. 1810–1828, APR 26 2011.

[37] R. A. Segalman, B. McCulloch, S. Kirmayer, and J. J. Urban, "Block Copolymers for Organic Optoelectronics," *Macromolecules*, vol. 42, pp. 9205–9216, DEC 8 2009.

[38] I. Botiz, R. D. Schaller, R. Verduzco, and S. B. Darling, "Optoelectronic Properties and Charge Transfer in Donor-Acceptor All-Conjugated Diblock Copolymers," *Journal of Physical Chemistry C*, vol. 115, pp. 9260–9266, MAY 12 2011.

[39] H. Xin, G. Ren, F. S. Kim, and S. A. Jenekhe, "Bulk Heterojunction Solar Cells from Poly(3-butylthiophene)/Fullerene Blends: In Situ Self-Assembly of Nanowires, Morphology, Charge Transport, and Photovoltaic Properties," *Chemistry of Materials*, vol. 20, pp. 6199–6207, OCT 14 2008.

[40] J. S. Kim, Y. Park, D. Y. Lee, J. H. Lee, J. H. Park, J. K. Kim, and K. Cho, "Poly(3-hexylthiophene) Nanorods with Aligned Chain Orientation for Organic Photovoltaics," *Advanced Functional Materials*, vol. 20, pp. 540–545, FEB 22 2010.

[41] M. Aryal, K. Trivedi, and W. W. Hu, "Nano-Confinement Induced Chain Alignment in Ordered P3HT Nanostructures Defined by Nanoimprint Lithography," *ACS Nano*, vol. 3, pp. 3085–3090, OCT 2009.

[42] N. Haberkorn, J. S. Gutmann, and P. Theato, "Template-Assisted Fabrication of Free-Standing Nanorod Arrays of a Hole-Conducting Cross-Linked Triphenylamine Derivative: Toward Ordered Bulk-Heterojunction Solar Cells," *ACS Nano*, vol. 3, pp. 1415–1422, JUN 2009.

[43] X. He, F. Gao, G. Tu, D. Hasko, S. Huettner, U. Steiner, N. C. Greenham, R. H. Friend, and W. T. S. Huck, "Formation of Nanopatterned Polymer Blends in Photovoltaic Devices," *Nano Letters*, vol. 10, pp. 1302–1307, APR 2010.

[44] M. S. Kim, J. S. Kim, J. C. Cho, M. Shtein, L. J. Guo, and J. Kim, "Flexible conjugated polymer photovoltaic cells with controlled heterojunctions fabricated using nanoimprint lithography," *Applied Physics Letters*, vol. 90, p. 123113, 2007.

[45] B. D. Olsen and R. A. Segalman, "Self-assembly of rod-coil block copolymers," *Materials Science & Engineering R-Reports*, vol. 62, pp. 37–66, JUL 30 2008.

[46] K. Coakley, B. Srinivasan, J. Ziebarth, C. Goh, Y. Liu, and M. McGehee, "Enhanced hole mobility in regioregular polythiophene infiltrated in straight nanopores," *Advanced Functional Materials*, vol. 15, pp. 1927–1932, DEC 2005.

[47] W. Wiedemann, L. Sims, A. Abdellah, A. Exner, R. Meier, K. Musselman, J. MacManus-Driscoll, P. Mueller-Buschbaum, G. Scarpa, P. Lugli, and L. Schmidt-Mende, "Polymer solar cells with a well-defined nanostructured interface," *Applied Physics Letters*, vol. 96, p. 263109, 2010.

[48] J. Nabity and M. Wybourne, "A Versatile Pattern Generator for High-Resolution Electron-beam Lithography," *Review of Scientific Instruments*, vol. 60, pp. 27–32, JAN 1989.

[49] G. M. Perera, G. E. Stein, and J. A. Liddle, "Spatial coherence in electron-beam patterning," *Journal of Vacuum Science & Technology B*, vol. 28, pp. 1048–1055, SEP-OCT 2010.

[50] V. Shrotriya, G. Li, Y. Yao, T. Moriarty, K. Emery, and Y. Yang, "Accurate measurement and characterization of organic solar cells," *Advanced Functional Materials*, vol. 16, pp. 2016–2023, OCT 4 2006.

[51] L. E. Ocola and A. Stein, "Effect of cold development on improvement in electron-beam nanopatterning resolution and line roughness," *Journal of Vacuum Science & Technology B*, vol. 24, pp. 3061–3065, NOV-DEC 2006. 50th International Conference on Electron, Ion, and Photon Beam Technology and Nanofavrication, Baltimore, MD, MAY 30-JUN 02, 2006.

[52] L. E. Ocola and V. R. Tirumala, "Nanofabrication of super-high-aspect-ratio structures in hydrogen silsesquioxane from direct-write e-beam lithography and hot development," *Journal of Vacuum Science & Technology B*, vol. 26, pp. 2632–2635, NOV 2008. 52nd International Conference on Electron, Ion and Photon Beam Technology and Nanofabrication, Portland, OR, MAY 27-30, 2008.

[53] W. Hu, K. Sarveswaran, M. Lieberman, and G. Bernstein, "Sub-10 nm electron beam lithography using cold development of poly(methylmethacrylate)," *Journal of Vacuum Science & Technology B*, vol. 22, pp. 1711–1716, JUL-AUG 2004.

[54] S. Cai, J. Keana, J. Nabity, and M. Wybourne, "Conducting Polymers as Deep-UV and Electron-beam Resists - Direct Production of Micrometer Scale Conducting Structures from Poly(3-Octylthiophene)," *Journal of Molecular Electronics*, vol. 7, pp. 63–68, APR-JUN 1991.

[55] M. Abdou, G. Diazguijada, M. Arroyo, and S. Holdcroft, "Photoimaging of Electronically Conducting Polymeric networks," *Chemistry of Materials*, vol. 3, pp. 1003–1006, NOV-DEC 1991.

[56] M. Abdou, W. Zi, A. Leung, and S. Holdcroft, "Laser, Direct-write Microlithography of Soluble Polythiophenes," *Synthetic Metals*, vol. 52, pp. 159–170, OCT 1 1992.

[57] M. Manceau, A. Rivaton, J.-L. Gardette, S. Guillerez, and N. Lemaitre, "The mechanism of photo- and thermooxidation of poly(3-hexylthiophene) (P3HT) reconsidered," *Polymer Degradation and Stability*, vol. 94, pp. 898–907, JUN 2009.

[58] I. R. Gearba, C.-Y. Nam, R. Pindak, and C. T. Black, "Thermal crosslinking of organic semiconducting polythiophene improves transverse hole conductivity," *Appl. Phys. Lett.*, vol. 95, p. 173307, 2009.

[59] M. Sundberg, O. Inganas, S. Stafstrom, G. Gustafsson, and B. Sjogren, "Optical-absorption of poly(3-alkylthiophenes) at low-temperatures," *Solid State Communications*, vol. 71, pp. 435–439, AUG 1989.

[60] P. Brown, D. Thomas, A. Kohler, J. Wilson, C. Kim, J.and Ramsdale, H. Sirringhaus, and R. Friend, "Effect of interchain interactions on the absorption and emission of poly(3-hexylthiophene)," *Physical Review B*, vol. 67, p. 064203, 2003.

[61] M. Abdou and S. Holdcroft, "Mechanisms of photodegradation of poly(3-alkylthiophenes) in solution," *Macromolecules*, vol. 26, pp. 2954–2962, MAY 24 1993.

[62] R. Hikmet and R. Thomassen, "Electron-beam-induced crosslinking of electroluminescent polymers for the production of multi-color patterned devices," *Advanced Materials*, vol. 15, pp. 115+, JAN 16 2003.

[63] J. Zhao, A. Swinnen, G. Van Assche, J. Manca, D. Vanderzande, and B. Van Mele, "Phase Diagram of P3HT/PCBM Blends and Its Implication for the Stability of Morphology," *Journal of Physical Chemistry B*, vol. 113, pp. 1587–1591, FEB 12 2009.

[64] P. E. Hopkinson, P. A. Staniec, A. J. Pearson, A. D. F. Dunbar, T. Wang, A. J. Ryan, R. A. L. Jones, D. G. Lidzey, and A. M. Donald, "A Phase Diagram of the P3HT:PCBM Organic Photovoltaic System: Implications for Device Processing and Performance," *Macromolecules*, vol. 44, pp. 2908–2917, APR 26 2011.

[65] Y. Kim, S. A. Choulis, J. Nelson, D. D. C. Bradley, S. Cook, and J. R. Durrant, "Device annealing effect in organic solar cells with blends of regioregular poly(3-hexylthiophene) and soluble fullerene," *Applied Physics Letters*, vol. 86, p. 063502, 2005.

[66] A. Van der Gon, J. Birgerson, M. Fahlman, and W. Salaneck, "Modification of PEDOT-PSS by low-energy electrons," *Organic Electronics*, vol. 3, pp. 111–118, DEC 2002.

[67] A. L. Ayzner, C. J. Tassone, S. H. Tolbert, and B. J. Schwartz, "Reappraising the Need for Bulk Heterojunctions in Polymer-Fullerene Photovoltaics: The Role of Carrier Transport in All-Solution-Processed P3HT/PCBM Bilayer Solar Cells," *Journal of Physical Chemistry C*, vol. 113, pp. 20050–20060, NOV 19 2009.

[68] K. H. Lee, P. E. Schwenn, A. R. G. Smith, H. Cavaye, P. E. Shaw, M. James, K. B. Krueger, I. R. Gentle, P. Meredith, and P. L. Burn, "Morphology of All-Solution-Processed "Bilayer" Organic Solar Cells," *Advanced Materials*, vol. 23, pp. 766+, FEB 8 2011.

[69] V. S. Gevaerts, L. J. A. Koster, M. M. Wienk, and R. A. J. Janssen, "Discriminating between Bilayer and Bulk Heterojunction Polymer: Fullerene Solar Cells Using the External Quantum Efficiency," *ACS Applied Materials & Interfaces*, vol. 3, pp. 3252–3255, SEP 2011.

[70] D. Chen, F. Liu, C. Wang, A. Nakahara, and T. P. Russell, "Bulk Heterojunction Photovoltaic Active Layers via Bilayer Interdiffusion," *Nano Letters*, vol. 11, pp. 2071–2078, MAY 2011.

[71] N. D. Treat, M. A. Brady, G. Smith, M. F. Toney, E. J. Kramer, C. J. Hawker, and M. L. Chabinyc, "Interdiffusion of PCBM and P3HT Reveals Miscibility in a Photovoltaically Active Blend," *Adavanced Energy Materials*, vol. 1, pp. 82–89, JAN 1 2011.

[72] D. R. Kozub, K. Vakhshouri, L. M. Orme, C. Wang, A. Hexemer, and E. D. Gomez, "Polymer Crystallization of Partially Miscible Polythiophene/Fullerene Mixtures Controls Morphology," *Macromolecules*, vol. 44, pp. 5722–5726, JUL 26 2011.

[73] A. Cravino, P. Schilinsky, and C. J. Brabec, "Characterization of organic solar cells: the importance of device layout," *Advanced Functional Materials*, vol. 17, pp. 3906–3910, DEC 17 2007.

[74] D. Gupta, M. Bag, and K. S. Narayan, "Area dependent efficiency of organic solar cells," *Applied Physics Letters*, vol. 93, p. 163301, 2008.

[75] C. Brabec, S. Shaheen, C. Winder, N. Sariciftci, and P. Denk, "Effect of LiF/metal electrodes on the performance of plastic solar cells," *Applied Physics Letters*, vol. 80, pp. 1288–1290, FEB 18 2002.

[76] E. Ahlswede, J. Hanisch, and M. Powalla, "Comparative study of the influence of lif, naf, and kf on the performance of polymer bulk heterojunction solar cells," *Applied Physics Letters*, vol. 90, p. 163504, 2007.

[77] B. J. Kim, Y. Miyamoto, B. Ma, and J. M. J. Frechet, "Photocrosslinkable Polythiophenes for Efficient, Thermally Stable, Organic Photovoltaics," *Advanced Functional Materials*, vol. 19, pp. 2273–2281, JUL 24 2009.

[78] P. E. Shaw, A. Ruseckas, and I. Samuel, "Exciton diffusion measurements in poly(3-hexylthiophene)," *Advanced Materials*, vol. 20, pp. 3516+, SEP 17 2008.

[79] C. Muller, A. Falcou, N. Reckefuss, M. Rojahn, V. Wiederhirn, P. Rudati, H. Frohne, O. Nuyken, H. Becker, and K. Meerholz, "Multi-colour organic light-emitting displays by solution processing," *Nature*, vol. 421, pp. 829–833, FEB 20 2003.

[80] F. C. Krebs, "Fabrication and processing of polymer solar cells: A review of printing and coating techniques," *Solar energy materials and solar cells*, vol. 93, pp. 394–412, APR 2009.

[81] S. Miyanishi, K. Tajima, and K. Hashimoto, "Morphological Stabilization of Polymer Photovoltaic Cells by Using Cross-Linkable Poly(3-(5-hexenyl)thiophene)," *Macromolecules*, vol. 42, pp. 1610–1618, MAR 10 2009.

[82] H. Kim, A.-R. Han, C.-H. Cho, H. Kang, H.-H. Cho, M. Lee, J. Frechet, J. Oh, and B. Kim, "Solvent-resistant organic transistors and thermally stable organic photovoltaics based on cross-linkable conjugated polymers," *Chemistry of Materials*, vol. 24, pp. 215–221, 2011.

[83] S. Jegadesan, S. Sindhu, R. Advincula, and S. Valiyaveettil, "Direct electrochemical nanopatterning of polycarbazole monomer and precursor polymer films: Ambient formation of thermally stable conducting nanopatterns," *Langmuir*, vol. 22, pp. 780–786, JAN 17 2006.

[84] S. Jegadesan, P. Taranekar, S. Sindhu, R. Advincula, and S. Valiyaveettil, "Electrochemically nanopatterned conducting coronas of a conjugated polymer precursor: SPM parameters and polymer composition," *Langmuir*, vol. 22, pp. 3807–3811, APR 11 2006.

[85] G. Jiang, A. Baba, and R. Advincula, "Nanopatterning and fabrication of memory devices from layer-by-layer poly(3,4-ethylenedioxythiophene)-poly(styrene sulfonate) ultrathin films," *Langmuir*, vol. 23, pp. 817–825, JAN 16 2007.

[86] J. Y. Park, P. Taranekar, and R. Advincula, "Polythiophene precursor electrochemical nanolithography: highly local thermal and morphological characterization," *Soft Matter*, vol. 7, no. 5, pp. 1849–1855, 2011.

[87] G. A. O'Brien, A. J. Quinn, D. A. Tanner, and G. Redmond, "A single polymer nanowire photodetector," *Advanced Materials*, vol. 18, pp. 2379–2382, SEP 18 2006.

[88] A. N. Sokolov, M. E. Roberts, and Z. Bao, "Fabrication of low-cost electronic biosensors," *Materials Today*, vol. 12, pp. 12–20, SEP 2009.

[89] P. Ruchhoeft and J. Wolfe, "Ion beam aperture-array lithography," *Journal of Vacuum Science & Technology B*, vol. 19, pp. 2529–2532, NOV-DEC 2001. 45th International Conference on Electron, Ion, and Photon Beam Technology and Nanofabrication, WASHINGTON, D.C., MAY 29-JUN 01, 2001.

[90] V. Parekh, E. Chunsheng, D. Smith, A. Ruiz, J. Wolfe, P. Ruchhoeft, E. Svedberg, S. Khizroev, and D. Litvinov, "Fabrication of a high anisotropy nanoscale patterned magnetic recording medium for data storage applications," *Nanotechnology*, vol. 17, pp. 2079–2082, MAY 14 2006.

[91] V. Parekh, A. Ruiz, P. Ruchhoeft, H. Nounu, D. Litvinov, and J. C. Wolfe, "Estimation of scattered particle exposure in ion beam aperture array lithography," *Journal of Vacuum Science & Technology B*, vol. 24, pp. 2915–2919, NOV-DEC 2006. 50th International Conference on Electron, Ion, and Photon Beam Technology and Nanofavrication, Baltimore, MD, MAY 30-JUN 02, 2006.

[92] A. Nasrullah, D. Smith, T. Sherlock, P. Ruchhoeft, and D. Litvinov, "Near neighbor averaging: A technique for improving image uniformity in aperture array lithography," *Journal of Vacuum Science & Technology B*, vol. 27, pp. 2674–2678, NOV 2009.

[93] A. Facchetti, "pi-conjugated polymers for organic electronics and photovoltaic cell applications," *Chemistry of Materials*, vol. 23, pp. 733–758, 2011.

[94] H. Zhou, L. Yang, and W. You, "Rational design of high performance conjugated polymers for organic solar cells," *Macromolecules*, vol. 45, pp. 607–632, 2012.

[95] C. Wang, H. Dong, W. Hu, Y. Liu, and D. Zhu, "Semiconducting pi-conjugated systems in field-effect transistors: A material odyssey of organic electronics," *Chemical Reviews*, vol. 112, pp. 2208–2267, 2012.

[96] X. Guo, M. Baumgarten, and K. Müllen, "Designing pi-conjugated polymers for organic electronics," *Progress in Polymer Science*, vol. 38, pp. 1832–1908, 2013.

[97] P. M. Beaujuge and J. M. J. Frechet, "Molecular design and ordering effects in pi-functional materials for transistor and solar cell applications," *Journal of the American Chemical Society*, vol. 133, pp. 20009–20029, 2011.

[98] B. D. C. J.-P. Cornil, J. and J.-L. . Brédas, "Interchain interactions in organic pi-conjugated materials: Impact on electronic structure, optical response, and charge transport," *Advanced Materials*, vol. 13, pp. 1053–1067, 2001.

[99] D. Fichou, "Structural order in conjugated oligothiophenes and its implications on opto-electronic devices," *Journal of Materials Chemistry*, vol. 10, pp. 571–588, 2000.

[100] X. Zhao and X. Zhan, "Electron transporting semiconducting polymers in organic electronics," *Chemical Society Reviews*, vol. 40, pp. 3728–3743, 2011.

[101] M. Jaiswal and R. Menon, "Polymer electronic materials: a review of charge transport," *Polymer International*, vol. 55, pp. 1371–1384, 2006.

[102] S. Persson, P. Dyreklev, and O. Inganas, "Patterning of poly(3-octylthiophene) conducting polymer films by electron beam exposure," *Advanced Materials*, vol. 8, pp. 405–&, MAY 1996.

[103] P. N. Murgatroyd, "Theory of space-charge-limited current enhanced by frenkel effect," *Journal of Physics D: Applied Physics*, vol. 3, p. 151, 1970.

[104] Z. Chiguvare and V. Dyakonov, "Trap-limited hole mobility in semiconducting poly(3-hexylthiophene)," *Physical Review B*, vol. 70, p. 235207, 2004.

[105] D. S. Chung, D. H. Lee, C. Yang, K. Hong, C. E. Park, J. W. Park, and S.-K. Kwon, "Origin of high mobility within an amorphous polymeric semiconductor:

Space-charge-limited current and trap distribution," *Applied Physics Letters*, vol. 93, p. 033303, 2008.

[106] C. R. Singh, G. Gupta, R. Lohwasser, S. Engmann, J. Balko, M. Thelakkat, T. Thurn-Albrecht, and H. Hoppe, "Correlation of charge transport with structural order in highly ordered melt-crystallized poly(3-hexythiophene) thin films," *Journal of Polymer Science Part B: Polymer Physics*, vol. 51, pp. 943–951, 2013.

[107] C. Goh, R. J. Kline, M. D. McGehee, E. N. Kadnikova, and J. M. J. Fréchet, "Molecular-weight-dependent mobilities in regioregular poly(3-hexyl-thiophene) diodes," *Applied Physics Letters*, vol. 86, p. 122110, 2005.

[108] F. Liu, Y. Gu, J. W. Jung, W. H. Jo, and T. P. Russell, "On the morphology of polymer-based photovoltaics," *Journal of Polymer Science Part B: Polymer Physics*, vol. 50, pp. 1018–1044, 2012.

[109] D. M. DeLongchamp, R. J. Kline, D. A. Fisher, L. J. Richter, and M. F. Toney, "Molecular characterization of organic electronic films," *Advanced Materials*, vol. 23, pp. 319–337, 2011.

[110] M. R. Hammond, R. J. Kline, A. A. Herzing, L. J. Richter, D. S. Germack, H.-W. Ro, C. L. Soles, D. A. Fischer, T. Xu, L. Yu, M. F. Toney, and D. M. DeLongchamp, "Molecular order in high-efficiency polymer/fullerene bulk heterojunction solar cells," *ACS Nano*, vol. 5, pp. 8248–8257, 2011.

[111] J. L. Baker, L. H. Jimison, S. Mannsfeld, S. Volkman, S. Yin, V. Subramanian, A. Salleo, A. P. Alivisatos, and M. F. Toney, "Quantification of thin film crystallographic orientation using x-ray diffraction with an area detector," *Langmuir*, vol. 26, pp. 9146–9151, 2010.

[112] R. Segalman, H. Yokoyama, and E. Kramer, "Graphoepitaxy of spherical domain block copolymer films," *Advanced Materials*, vol. 13, pp. 1152+, AUG 3 2001.

[113] J. Cheng, C. Ross, E. Thomas, H. Smith, and G. Vancso, "Fabrication of nanostructures with long-range order using block copolymer lithography," *Applied Physics Letters*, vol. 81, pp. 3657–3659, NOV 4 2002.

[114] S. Kim, H. Solak, M. Stoykovich, N. Ferrier, J. de Pablo, and P. Nealey, "Epitaxial self-assembly of block copolymers on lithographically defined nanopatterned substrates," *Nature*, vol. 424, pp. 411–414, JUL 24 2003.

[115] M. Stoykovich, M. Muller, S. Kim, H. Solak, E. Edwards, J. de Pablo, and P. Nealey, "Directed assembly of block copolymer blends into nonregular device-oriented structures," *Science*, vol. 308, pp. 1442–1446, JUN 3 2005.

[116] M. Matsen, "Thin films of block copolymer," *Journal of Chemical Physics*, vol. 106, pp. 7781–7791, MAY 8 1997.

[117] G. Coulon, T. Russell, V. Deline, and P. Green, "Surface-Induced Orientation of Symmetric, Diblock Copolymers - A Secondary Ion Mass-Spectrometry Study," *Macromolecules*, vol. 22, pp. 2581–2589, JUN 1989.

[118] G. Coulon, B. Collin, D. Ausserre, D. Chatenay, and T. Russell, "Islands and Holes on the Free-Surface of Thin Diblock Copolymer Films .1. Characteristics of Formation and Growth," *Journal De Physique*, vol. 51, pp. 2801–2811, DEC 15 1990.

[119] S. Anastasiadis, T. Russell, S. Satija, and C. Majkrzak, "The Morphology of Symmetric Diblock Copolymers as Revealed by Neutron Reflectivity," *Journal of Chemical Physics*, vol. 92, pp. 5677–5691, MAY 1 1990.

[120] A. Mayes, T. Russell, P. Bassereau, S. Baker, and G. Smith, "Evolution of order in thin block-copolymer films," *Macromolecules*, vol. 27, pp. 749–755, JAN 31 1994.

[121] J. G. Son, X. Bulliard, H. Kang, P. F. Nealey, and K. Char, "Surfactant-Assisted Orientation of Thin Diblock Copolymer Films," *Advanced Materials*, vol. 20, pp. 3643+, OCT 2 2008.

[122] T. Morkved, M. Lu, A. Urbas, E. Ehrichs, H. Jaeger, P. Mansky, and T. Russell, "Local control of microdomain orientation in diblock copolymer thin films with electric fields," *Science*, vol. 273, pp. 931–933, AUG 16 1996.

[123] E. Sivaniah, Y. Hayashi, M. Iino, T. Hashimoto, and K. Fukunaga, "Observation of perpendicular orientation in symmetric diblock copolymer thin films on rough substrates," *Macromolecules*, vol. 36, pp. 5894–5896, AUG 12 2003.

[124] K. G. Yager, B. C. Berry, K. Page, D. Patton, A. Karim, and E. J. Amis, "Disordered nanoparticle interfaces for directed self-assembly," *Soft Matter*, vol. 5, no. 3, pp. 622–628, 2009.

[125] G. Kim and M. Libera, "Morphological development in solvent-cast polystyrene-polybutadiene-polystyrene (SBS) triblock copolymer thin films," *Macromolecules*, vol. 31, pp. 2569–2577, APR 21 1998.

[126] S. Kim, M. Misner, T. Xu, M. Kimura, and T. Russell, "Highly oriented and ordered arrays from block copolymers via solvent evaporation," *Advanced Materials*, vol. 16, pp. 226+, FEB 3 2004.

[127] Y. Lin, A. Boker, J. He, K. Sill, H. Xiang, C. Abetz, X. Li, J. Wang, T. Emrick, S. Long, Q. Wang, A. Balazs, and T. Russell, "Self-directed self-assembly of nanoparticle/copolymer mixtures," *Nature*, vol. 434, pp. 55–59, MAR 3 2005.

[128] U. Jeong, D. Ryu, D. Kho, J. Kim, J. Goldbach, D. Kim, and T. Russell, "Enhancement in the orientation of the microdomain in block copolymer thin films upon the addition of homopolymer," *Advanced Materials*, vol. 16, pp. 533+, MAR 18 2004.

[129] P. Mansky, T. Russell, C. Hawker, M. Pitsikalis, and J. Mays, "Ordered diblock copolymer films on random copolymer brushes," *Macromolecules*, vol. 30, pp. 6810–6813, NOV 3 1997.

[130] D. Ryu, K. Shin, E. Drockenmuller, C. Hawker, and T. Russell, "A generalized approach to the modification of solid surfaces," *Science*, vol. 308, pp. 236–239, APR 8 2005.

[131] S. Ham, C. Shin, E. Kim, D. Y. Ryu, U. Jeong, T. P. Russell, and C. J. Hawker, "Microdomain orientation of PS-b-PMMA by controlled interfacial interactions," *Macromolecules*, vol. 41, pp. 6431–6437, SEP 9 2008.

[132] E. Han, K. O. Stuen, Y.-H. La, P. F. Nealey, and P. Gopalan, "Effect of Composition of Substrate-Modifying Random Copolymers on the Orientation of Symmetric and Asymmetric Diblock Copolymer Domains," *Macromolecules*, vol. 41, pp. 9090–9097, DEC 9 2008.

[133] S. Ji, C.-C. Liu, J. G. Son, K. Gotrik, G. S. W. Craig, P. Gopalan, F. J. Himpsel, K. Char, and P. F. Nealey, "Generalization of the Use of Random Copolymers To Control the Wetting Behavior of Block Copolymer Films," *Macromolecules*, vol. 41, pp. 9098–9103, DEC 9 2008.

[134] E. Han, K. O. Stuen, M. Leolukman, C.-C. Liu, P. F. Nealey, and P. Gopalan, "Perpendicular Orientation of Domains in Cylinder-Forming Block Copolymer Thick Films by Controlled Interfacial Interactions," *Macromolecules*, vol. 42, pp. 4896–4901, JUL 14 2009.

[135] H. S. Suh, H. Kang, C.-C. Liu, P. F. Nealey, and K. Char, "Orientation of Block Copolymer Resists on Interlayer Dielectrics with Tunable Surface Energy," *Macromolecules*, vol. 43, pp. 461–466, JAN 12 2010.

[136] T. Russell, A. Menelle, S. Anastasiadis, S. Satija, and C. Majkrzak, "Unconventional Morphologies of Symmetrical, Diblock Copolymers due to Film Thickness Constraints," *Macromolecules*, vol. 24, pp. 6263–6269, NOV 11 1991.

[137] W. Dejeu, P. Lambooy, I. Hamley, D. Vaknin, J. Pederson, K. Kjaer, R. Seyger, P. Vanhutten, and G. Hadziioannou, "On the Morphology of a Lamellar Triblock Copolymer Film," *Journal De Physique II*, vol. 3, pp. 139–146, JAN 1993.

[138] Y. Zhao, E. Sivaniah, and T. Hashimoto, "SAXS Analysis of the Order-Disorder Transition and the Interaction Parameter of Polystyrene-block-poly(methyl methacrylate)," *Macromolecules*, vol. 41, pp. 9948–9951, DEC 23 2008.

[139] T. Russell, G. Coulon, V. Deline, and D. Miller, "Characteristics of the Surface-Induced Orientation For Symmetric Diblock PS/PMMA Copolymers," *Macromolecules*, vol. 22, pp. 4600–4606, DEC 1989.

[140] P. Mansky, T. Russell, C. Hawker, J. Mays, D. Cook, and S. Satija, "Interfacial segregation in disordered block copolymers: Effect of tunable surface potentials," *Physical Review Letters*, vol. 79, pp. 237–240, JUL 14 1997.

[141] P. Green and R. Limary, "Block copolymer thin films: pattern formation and phase behavior," *Advances in Colloid and Interface Science*, vol. 94, pp. 53–81, NOV 15 2001. European Research Conference on Interfaces and Colloidal Systems, AGHIA PELAGHIA, GREECE, SEP 18-23, 1999.

[142] B. Lee, I. Park, J. Yoon, S. Park, J. Kim, K. Kim, T. Chang, and M. Ree, "Structural analysis of block copolymer thin films with grazing incidence small-angle X-ray scattering," *Macromolecules*, vol. 38, pp. 4311–4323, MAY 17 2005.

[143] G. E. Stein, E. J. Kramer, X. Li, and J. Wang, "Layering transitions in thin films of spherical-domain block copolymers," *Macromolecules*, vol. 40, pp. 2453–2460, APR 3 2007.

[144] G. Renaud, R. Lazzari, and F. Leroy, "Probing surface and interface morphology with Grazing Incidence Small Angle X-Ray Scattering," *Surface Science Reports*, vol. 64, pp. 255–380, AUG 31 2009.

[145] P. Busch, M. Rauscher, J.-F. Moulin, and P. Mueller-Buschbaum, "Debye-Scherrer rings from block copolymer films with powder-like order," *Journal of Applied Crystallography*, vol. 44, pp. 370–379, APR 2011.

[146] Y. Tsori and D. Andelman, "Surface induced ordering in thin film diblock copolymers: Tilted lamellar phases," *Journal of Chemical Physics*, vol. 115, pp. 1970–1978, JUL 22 2001.

[147] Y. Tsori and D. Andelman, "Diblock copolymer ordering induced by patterned surfaces," *Europhysics Letters*, vol. 53, pp. 722–728, MAR 2001.

[148] Q. Wang, "Morphology of symmetric diblock copolymers confined between two stripe-patterned surfaces - Tilted lamellae and more," *Macromolecular Theory and Simulations*, vol. 14, pp. 96–108, FEB 18 2005.

[149] S. O. Kim, B. H. Kim, K. Kim, C. M. Koo, M. P. Stoykovich, P. F. Nealey, and H. H. Solak, "Defect structure in thin films of a lamellar block copolymer self-assembled on neutral homogeneous and chemically nanopatterned surfaces," *Macromolecules*, vol. 39, pp. 5466–5470, AUG 8 2006.

[150] T. Lodge and M. Dalvi, "Mechanisms of Chain Diffusion in Lamellar Block-Copolymers," *Physical Review Letters*, vol. 75, pp. 657–660, JUL 24 1995.

[151] G. Fredrickson and F. Bates, "Dynamics of block copolymers: Theory and experiment," *Annual Review of Materials Research*, vol. 26, pp. 501–550, 1996.

[152] G. Wilmes, D. Durkee, N. Balsara, and J. Liddle, "Bending soft block copolymer nanostructures by lithographically directed assembly," *Macromolecules*, vol. 39, pp. 2435–2437, APR 4 2006.

[153] M. P. Stoykovich, H. Kang, K. C. Daoulas, G. Liu, C.-C. Liu, J. J. de Pablo, M. Mueller, and P. F. Nealey, "Directed self-assembly of block copolymers for nanolithography: Fabrication of isolated features and essential integrated circuit geometries," *ACS Nano*, vol. 1, pp. 168–175, OCT 2007.

[154] J. Chai and J. M. Buriak, "Using cylindrical domains of block copolymers to self-assemble and align metallic nanowires," *ACS Nano*, vol. 2, pp. 489–501, MAR 2008.

[155] T. Xu, C. Hawker, and T. Russell, "Interfacial interaction dependence of microdomain orientation in diblock copolymer thin films," *Macromolecules*, vol. 38, pp. 2802–2805, APR 5 2005.

[156] I. A. Zucchi, E. Poliani, and M. Perego, "Microdomain orientation dependence on thickness in thin films of cylinder-forming PS-b-PMMA," *Nanotechnology*, vol. 21, MAY 7 2010.

[157] E. Huang, P. Mansky, T. Russell, C. Harrison, P. Chaikin, R. Register, C. Hawker, and J. Mays, "Mixed lamellar films: Evolution, commensurability effects, and preferential defect formation," *Macromolecules*, vol. 33, pp. 80–88, JAN 11 2000.

[158] C.-C. Liu, P. F. Nealey, Y.-H. Ting, and A. E. Wendt, "Pattern transfer using poly(styrene-block-methyl methacrylate) copolymer films and reactive ion etching," *Journal of Vacuum Science & Technology B*, vol. 25, pp. 1963–1968, NOV 2007. 51st International Conference on Electron, Ion, and Photon Beam Technology and Nanofabrication, Denver, CO, MAY 29-JUN 01, 2007.

[159] R. Ruiz, H. Kang, F. A. Detcheverry, E. Dobisz, D. S. Kercher, T. R. Albrecht, J. J. de Pablo, and P. F. Nealey, "Density multiplication and improved lithography by directed block copolymer assembly," *Science*, vol. 321, pp. 936–939, 2008.

[160] J. Y. Cheng, D. P. Sanders, H. D. Truong, S. Harrer, A. Friz, S. Holmes, M. Colburn, and W. D. Hinsberg, "Simple and Versatile Methods To Integrate Directed Self-Assembly with Optical Lithography Using a Polarity-Switched Photoresist," *ACS Nano*, vol. 4, pp. 4815–4823, AUG 2010.

[161] R. Ruiz, R. L. Sandstrom, and C. T. Black, "Induced orientational order in symmetric diblock copolymer thin films," *Advanced Materials*, vol. 19, pp. 587+, FEB 19 2007.

[162] C. Harrison, P. Chaikin, D. Huse, R. Register, D. Adamson, A. Daniel, E. Huang, P. Mansky, T. Russell, C. Hawker, D. Egolf, I. Melnikov, and E. Bodenschatz, "Reducing substrate pinning of block copolymer microdomains with a buffer layer of polymer brushes," *Macromolecules*, vol. 33, pp. 857–865, FEB 8 2000.

[163] T. Vu, N. Mahadevapuram, G. M. Perera, and G. E. Stein, "Controlling Domain Orientations in Thin Films of AB and ABA Block Copolymers," *Macromolecules*, vol. 44, pp. 6121–6127, AUG 9 2011.

[164] S. Choi, E. Kim, H. Ahn, S. Naidu, Y. Lee, C. J. Hawker, and T. P. Russell, "Lamellar microdomain orientation and phase transition of polystyrene-b-poly(methyl methacrylate) films by controlled interfacial interactions," *Soft Matter*, vol. 8, pp. 3463–3469, 2012.

[165] T. Mykhaylyk, S. Evans, I. Hamley, and J. Henderson, "Ellipsometric study of adsorption on nanopatterned block copolymer substrates.," *The Journal of Chemical Physics*, vol. 122, p. 104902, 2005.

[166] Z. Jiang, X. Li, J. Strzalka, M. Sprung, T. Sun, A. R. Sandy, S. Narayanan, D. R. Lee, and J. Wang, "The dedicated high-resolution grazing-incidence x-ray scattering beamline 8-id-e at the advanced photon source," *Journal of Synchrotron Radiation*, vol. 19, pp. 627–636, 2012.

[167] L. Parratt, "Surface studies of solids by total reflection of x-rays," *Physical Review*, vol. 95, pp. 359–369, 1954.

[168] S. Wu, "Calculation of interfacial tension in polymer systems," *Journal of Polymer Science Part C: Polymer Symposia*, vol. 34, pp. 19–30, 1971.

[169] S. Wu, "Polar and nonpolar interactions in adhesion," *The Journal of Adhesion*, vol. 5, pp. 39–55, 1973.

[170] J. P. Spatz, P. Eibeck, S. Mössmer, M. Möller, E. Y. Kramarenko, P. G. Khalatur, I. I. Potemkin, A. R. Khokhlov, R. G. Winkler, and P. Reineker, "Order-disorder transition in surface-induced nanopattern of diblock copolymer films," *Macromolecules*, vol. 33, pp. 150–157, 2000.

[171] A. Welander, H. Kang, K. Stuen, H. Solak, M. Mueller, J. de Pablo, and P. Nealey, "Rapid directed assembly of block copolymer films at elevated temperatures," *Macromolecules*, vol. 41, p. 2759, 2008.

[172] C. Harrison, D. H. Adamson, Z. Cheng, J. M. Sebastian, S. Sethuraman, D. A. Huse, R. A. Register, and P. M. Chaikin, "Mechanisms of ordering in striped patterns," *Science*, vol. 290, pp. 1558–1560, 2000.

[173] a. G. H. F. a. E. J. K. Matthew R. Hammond, and Eric Cochran, "Temperature dependence of order, disorder, and defects in laterally confined diblock copolymer cylinder monolayers," *Macromolecules*, vol. 38, pp. 6575–6585, 2005.

[174] C. Harrison, Z. Cheng, S. Sethuraman, P. Huse, D.; Chaikin, D. Vega, J. Sebastian, R. Register, and D. Adamson, "Dynamics of pattern coarsening in a two-dimensional smectic system," *Physical Review E*, vol. 66, 2002.

[175] E. Sivaniah, Y. Hayashi, S. Matsubara, S. Kiyono, T. Hashimoto, a. E. J. K. K. Fukunaga, and T. Mates, "Symmetric diblock copolymer thin films on rough

substrates. kinetics and structure formation in pure block copolymer thin films," *Macromolecules*, vol. 38, pp. 1837–1849, 2005.

[176] J. Bang, B. J. Kim, G. E. Stein, T. P. Russell, X. Li, J. Wang, E. J. Kramer, and C. J. Hawker, "Effect of humidity on the ordering of PEO-based copolymer thin films," *Macromolecules*, vol. 40, pp. 7019–7025, SEP 18 2007.

[177] C.-C. Liu, A. Ramírez-Hernández, E. Han, G. S. Craig, Y. Tada, H. Yoshida, H. Kang, S. Ji, P. Gopalan, J. J. de Pablo, and P. F. Nealey, "Chemical patterns for directed self-assembly of lamellae-forming block copolymers with density multiplication of features," *Macromolecules*, vol. 46, pp. 1415–1424, 2013.

[178] G. Perera, C. Wang, M. Doxastakis, R. Kline, W. Wu, A. Bosse, and G. Stein, "Directed self-assembly of lamellar copolymers: Effects of interfacial interactions on domain shape," *ACS Macro Letters*, vol. 1, pp. 1244–1248, 2012.